UNIVERSITÀ DEGLI STUDI DI BARI

FACOLTA' DI SCIENZE MATEMATICHE FISICHE E NATURALI

Dipartimento Interateneo di Fisica "M.Merlin"

TESI DI DOTTORATO DI RICERCA IN FISICA

Settore scientifico-disciplinare FIS/01

Ciclo di Dottorato XXIV

THE UPGRADE OF THE ALICE INNER TRACKING SYSTEM

Dott. Cristina Terrevoli

ESAME FINALE 2012

Contents

Introduction **5**

1 Heavy Ion Collisions and ALICE **9**

1.1 The phase transition to QGP 10

1.1.1 QGP in Heavy Ion Collisions 15

1.2 Heavy Flavour Physics in heavy ion collisions 22

1.2.1 In-Medium Energy Loss 24

1.2.2 Probing QGP with heavy flavour 25

1.3 Thermalization 30

1.4 Hadronization: fragmentation vs. recombination 32

1.5 Flow 34

1.6 The ALICE Experiment at LHC 37

1.6.1 The ALICE detectors 38

1.6.2 Time Projection Chamber 40

1.6.3 Time Of Flight 42

2 The Inner Tracking System of ALICE **44**

2.1 ITS: the vertex detector of ALICE 45

2.1.1 Impact parameter and transverse momentum resolution: physics performance 47
2.2 The ITS subdetectors 50
2.2.1 Silicon Pixel Detector (SPD) 51
2.2.2 Silicon Drift Detector (SDD) 55
2.2.3 Silicon Strip Detector (SSD) 58
2.3 ITS status in the first data taking years 60
2.3.1 SPD status 60
2.3.2 SDD status 61
2.3.3 SSD status 61
2.4 ITS Performance in pp and Pb–Pb 62
2.4.1 Alignment studies 63
2.4.2 ITS and TPC combined tracking algorithm 65
2.5 Detector efficiency 71

3 ITS Upgrade motivation 83

ALICE physics performance in Pb–Pb and Motivation for an upgrade of the ITS 83

3.1 Physics goal of the ALICE experiment 84
3.1.1 Charged-Particle Multiplicity Density 85
3.1.2 QGP: volume and life time 87
3.2 Suppression of high p_T charged particle production 87
3.3 In medium Energy Loss of charmed mesons 89
3.3.1 Baryon to Meson Ratio measurement 92

3.3.2 Elliptic Flow measurement 95
3.4 Motivations for the upgrade of the Inner Tracking System . . 100
3.4.1 Impact of the ITS upgrade and new measurements . . 101
3.5 Technologies for the upgrade 102
3.6 Upgrade Timeline 106

4 ITS Upgrade simulation studies 108

4.1 Introduction 108
4.2 Simulation conditions 109
4.3 Simulation Tool 111
4.3.1 The simulation framework: ROOT, GEANT3 and AliROOT 113
4.4 ITS Upgrade simulation 114
4.4.1 Geometrical simulation of the detector 114
4.4.2 Transport code simulation with Geant3 and Response Model 117
4.4.3 Cluster Finder 120
4.4.4 Global, Local and Tracking reference system 121
4.4.5 Stand-alone Tracking Algorithm 123
4.5 Tracking Performance: impact parameter resolution, transverse momentum resolution 127
4.6 Fast Tool simulation 130
4.6.1 Impact of the first L0 layer on the impact parameter resolution. 131

4.7 7-layers Upgrade Scenario 134
4.7.1 Tracking efficiency 139

5 Performance Study on the benchmark channel Λ_c 141

5.1 Analysis of Λ_c with the current ITS 141
5.1.1 Analysis Strategy 143
5.1.2 Simulation method 148
5.2 Performance studies for $\Lambda_c \to pK\pi$ 150
5.2.1 Cuts Optimization 152
5.2.2 Results 155
5.3 Performance with further improved detector 158
5.4 Reconstruction efficiency 159
5.5 Conclusion 160

Conclusions 161

Bibliography 165

Introduction

In the last two decades, nuclear physics has extended its domain, thanks to the developments in accelerator technology. Heavy ion collisions are now possible at energies never reached before, which allow to study a new state of matter with partonic degrees of freedom: the Quark Gluon Plasma. Recent experimental results from the Super Proton Synchrotron (SPS) and the Relativistic Heavy Ion Collider (RHIC) have already provided the evidence that such a new state was created. These first observations motivate studies at even higher energies, such as those reached by the Large Hadron Collider (LHC), which would allow a deeper understanding and characterization of the new state.

ALICE (A Large Ion Collider Experiment) is one of the four main experiments at the LHC. The main goal of ALICE is the study of nuclear matter under extreme conditions of temperature and energy density, such as those attained in nucleus–nucleus collisions at a center-of-mass energy, that, for Pb–Pb nuclei, will reach an energy of 5.5 TeV per nucleon pair. Proton-proton and proton-nucleus collisions are also part of the ALICE physics program.

After two years of operation with p-p collisions and the first run with Pb-Pb collisions at the centre-of-mass energy of 2.76 TeV per nucleon pair, ALICE has already demonstrated its excellent capabilities to measure high energy nuclear collisions at the LHC. Nevertheless, there are several frontiers for which the current experimental setup is not yet fully optimized, and where detector upgrades could enormously enhance the physics capabilities. One of the domains which would most profit of an upgraded detector is the study of heavy quark production: this is a fundamental probe for the investigation of the properties of the hot and dense matter formed at the LHC.

The heavy quark pairs ($c\bar{c}$ and $b\bar{b}$), produced in the very initial stage of the collision, come out from the interaction region as hadrons, possibly as a part of a jet, and carry out information about the properties of the traversed medium. Such information can be extracted from the properties of the open charm and beauty hadrons in the final state. Charm and beauty hadrons decay weakly with a mean free path of the order of a few hundred microns. Therefore, their identification relies on the possibility of resolving a decay vertex at such distances from the primary vertex. The ALICE Inner Tracking System (ITS), made of six layers of silicon detectors, has been designed and built for this purpose and it has provided the first results on heavy quark measurements, though with some limitations. A detector based on today's frontier technologies would certainly offer new exciting possibilities within the above described physics scope.

At the moment, different scenarios for the new detector layout and

technologies are being considered. With respect to the current ITS, the baseline idea for the upgraded tracker is to have a detection layer closer to the beam line (which implies a beam pipe with smaller radius) and a larger number of layers instrumented with silicon pixels. The track position resolution at the primary vertex could be improved by a factor 3.

Besides the natural improvement of the measurement capabilities on the channels already well measured with the present ITS, the upgraded ITS will offer the possibility of exploring new physics items. Examples are: baryons containing heavy quarks, the exclusive decay channels of B-mesons, the production mechanisms of hadrons containing more than one heavy quark.

In this thesis, studies for an upgrade of the ALICE ITS are presented. In particular, the work focuses on two aspects: the implementation of a flexible simulation tool, suitable for the study and optimization of different upgrade layouts; a study of the performance of an upgraded ITS in the heavy quark baryon (Λ_c) sector.

The thesis is structured as follows:

- In Chapter 1 the physics of the QGP and the importance of charm and beauty particles as probes of this state of matter are discussed; a comparison of the heavy ion collisions at LHC with those at previous high energy accelerators and a description of the ALICE setup are also discussed.

- In Chapter 2 a detailed description of the ITS is given; its present status and performance are shown.

- In Chapter 3 the physics performance and limitations of the present ALICE detector in studying heavy flavour at mid-rapidity in Pb–Pb collisions are discussed; the motivations for an upgrade of the ITS are explained.

- In Chapter 4 the implementation of a simulation tool, fully integrated in the existing ALICE simulation and analysis framework, is described. The tool is needed to study the performance of the new detector and to optimise its layout. The performance obtained with two new layouts is also discussed.

- In Chapter 5 a study is presented of the physics performance of the upgraded detector in the benchmark physics channel $\Lambda_c \to pK\pi$, which is the most interesting to be studied with an upgraded detector.

Chapter 1

The physics of Heavy Ion Collisions and the ALICE experiment at LHC

High energy physics is generally identified as the physics of elementary particle: its goals are to understand what are the elementary building blocks of nature and how they interact with each other. The currently accepted theory of particle physics is called Standard Model: a quantum field theory of elementary particles and their fundamental interactions which has been developed and validated in the second half of the twentieth century and is currently well established. Applications of the Standard Model to complex and dynamically evolving systems of finite size under extreme conditions of density and temperature is the main aim of heavy-ion physics. The particular sector of the Standard Model that deals with strong interactions is the theory of Quantum Chromodynamics (QCD). QCD predicts that a new phase of nuclear matter could appear in high density and temperature domains: when the energy density exceeds a critical value, quarks and gluons

can be deconfined over volumes much larger than the hadronic size, thereby forming a new state of matter called "Quark Gluon Plasma" (QGP) [1]. Ultra-relativistic heavy-ion collisions are an ideal tool for the experimental study of QGP. They represent the main field of interest of the ALICE experiment at the LHC.

The content of this chapter is the following:

- the main aspects of the physics of ultra-relativistic heavy-ion collisions are presented;
- the importance of particles containing charm and beauty quarks (the so-called heavy flavour) as the probes of the new matter is discussed;
- a description of the ALICE experiment is given.

1.1 The phase transition to QGP

The traditional energy scale for nuclear physics is that of the nuclear energy density:

$$\epsilon_{nuclear} = 0.15 \ \frac{GeV}{fm^3} \tag{1.1}$$

With the onset of relativistic heavy ion accelerators, high energy nuclear physics was born, extending the domain of nuclear physics. In particular, heavy ion physics studies nuclear matter under conditions of extreme density and temperature, with the aim of determining how macroscopic properties and collective phenomena emerge from the microscopic laws of particle physics, in systems with many degrees of freedom.

Matter at low energy densities is composed of protons, neutrons and electrons. If the system is heated, light mass strongly interacting particles such as pions are produced as thermal excitations. If the energy density is high enough, particles such as neutrons and protons overlap, so that their constituents (quarks and gluons) are free to roam the system without being confined into hadrons, there is deconfinement and a phase transition to the Quark Gluon Plasma, as predicted by the lattice QCD [2].

The phase diagram of nuclear matter

The energy density at which the transition to QGP occurs is of the order of:

$$\epsilon_{QGP} \simeq 1 \ \frac{GeV}{fm^3} \tag{1.2}$$

At such energy density the strong coupling constant is so weak that a gas of particles can be treated with some approximation as an ideal gas. How deconfinement results in a collective phenomenon such as a phase transition can be intuitively understood by means of a simple model, called bag model [3], in which particles (be them hadrons or partons) are treated as a non-interacting (thus ideal) gas, confined in a limited volume by an external pressure B (bag pressure). In such model, the energy density of the gas is:

$$\epsilon(T) = N\frac{\pi^2}{30}T^4 + B \tag{1.3}$$

where N is the number of degrees of freedom of the system. For a gas of pions (chosen here to represent the confined phase) N is equal to three (the

possible values for the third component of the isospin), while for a gas of gluons and quarks $N=N_g+\frac{7}{8}N_q$, where:

- $N_g=8\times2$ is the number of degrees of freedom for gluons (colour and helicity states);
- $N_q=3\times2\times2$ is the number of degrees of freedom (colour, q-$\overline{q}$, spin) for each relevant quark specie (flavour);
- the factor $\frac{7}{8}$ arises from the difference between the Fermi-Dirac statistics (for quarks) and the Bose-Einstein statistics (for gluons).

Thus, $N_{QGP}=16+12\frac{7}{8}N_F$, where N_F is the number of relevant quark species (for example 3 if the temperature is below the charm quark mass). It is clear that there is a difference of more than one order of magnitude between the numbers of degrees of freedom of the confined and the deconfined phase, which results in a steep rise of the ratio ϵ/T^4 in a narrow temperature range, which indicates a phase transition.

The phase diagram of nuclear matter can be conveniently represented in the T-μ_B plane, where μ_B is the chemical potential of the baryon number: the chemical potential of a baryon is a measure of how much energy it would cost to introduce another baryon into the system, and it is related to the baryon density. The picture of the phase diagram (see Fig. 1.1) has evolved with time, according to the developments of theoretical tools and the availability of experimental results. For istance, the nature of the phase transition, i.e. its order, has to be established: the solid lines in Fig. 1.1

represent a first order phase transition, while the dashed lines represent a rapid crossover.

The calculations performed to study the phase diagram of nuclear matter are different in different regions of the diagram.
Along the temperature axis, at μ_B=0, the main tool is lattice QCD, i.e. a non-perturbative theory descending from QCD's first principles such as gauge invariance, whose equations are solved numerically by discretising the space-time on a grid of finite step. According to lattice calculations [2], deconfinement sets in at a temperature $T_C \simeq 170$ MeV: near such value, the ratio ϵ/T^4 increases by an order of magnitude, and at higher temperatures it settles at about 80% of the Stefan-Bolzmann value for a gas of non-interacting quarks and gluons (Fig. 1.2). At present, the phase transition along the temperature axis is believed to be a rapid crossover.

For non-zero baryon chemical potential, the expectations rely on models interpolating between low-density hadronic matter, described by effective theories, and high-density QGP, described by QCD. The uncertainties in this regime are larger than those arising from lattice QCD at μ_B=0. The current expectations state that QGP at T=0 can be obtained by compressing nuclear matter to a density of $3 \div 10\rho_0$, where ρ_0=0.15 fm^{-3} is the nuclear density of ordinary matter. This density range corresponds to values of μ_B around 1 GeV. The phase transition along the μ_B axis is at present believed to be a first order transition. According to expectations, when moving along the phase transition line, there has to be a critical point at which the transition

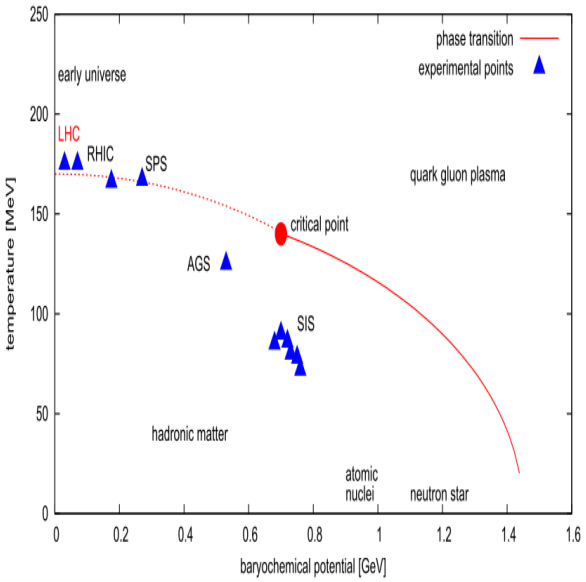

Figure 1.1: Phase diagram of nuclear matter. Triangular markers indicates the estimations extracted by the particle abundances measured in heavy ion collisions experiments and fitted with statistical models.

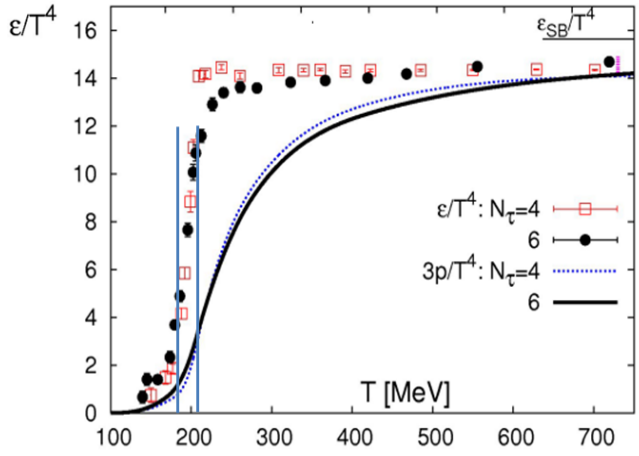

Figure 1.2: Ratio of the energy density to T^4 as a function of T, computed for nuclear matter with 2 degenerate light quarks and a heavier one, for different lattice temporal extent N_τ settings. The two vertical bars mark the interval T=(175±15)MeV, while the horizontal bar marks the Stefan Boltzmann value of ϵ/T^4 for a gas of non interacting quarks and gluons. Figure is taken from Ref. [4].

is of the second order, and beyond which it becomes a crossover (Fig. 1.1). According to the latest theoretical developments, quark matter at high densities and low temperatures should enter a phase other than QGP, analogous to the superconducting phase of solid-state physics.

1.1.1 QGP in Heavy Ion Collisions

The conditions needed to study experimentally the Quark-Gluon Plasma may be realized in central ultra-relativistic heavy ion collisions. These conditions are:

- the number of constituents of the system must be large, so that the system can be described by means of macroscopic variables; for the same reason, the size of the system must be larger than the range of strong nuclear interaction ($\simeq$ 1 fm);
- the system must reach equilibrium, so that thermodynamical variables are well defined: this implies a lifetime of the system larger than the typical time-scale of strong nuclear interaction ($\simeq$ 1fm/c);
- the critical conditions for the transition to QGP must be realized and held until thermalisation occurs.

Evolution of the system

The evolution in time of a high energy heavy ion collision is pictured in Fig. 1.3. It can be summarized as follows:

- the two Lorentz-contracted nuclei collide. The probability density function (PDF) of nucleus can in general be different from that of protons;
- pre-equilibrium (t $<$ 1 fm/c): partons scatter among each other and give rise to an abundant production of particles;
- thermalisation and QGP: (1 fm/c $<$ t $<$ 10 fm/c): matter reaches equilibrium, QGP forms: the degrees of freedom here are those of quarks and gluons;
- mixed phase: the system, while expanding, begins to convert into a hadron gas (very short phase, Δ t $\rightarrow$ 0);
- hadronisation: (t $\simeq$ 10 fm/c) quarks and gluons are again confined into hadrons;
- chemical freeze-out: inelastic interactions between hadrons cease, relative abundances are fixed;
- thermal freeze-out: elastic interactions between hadrons cease, kinematical spectra are fixed.

Energy density

The determination of the energy density reached in the stages mentioned above is not straightforward; the most used definition was given by Bjorken in 1983 [5]:

$$\epsilon_{Bj} = \frac{1}{Ac\tau_f}\frac{\mathrm{d}E_\mathrm{T}}{\mathrm{d}y} \tag{1.4}$$

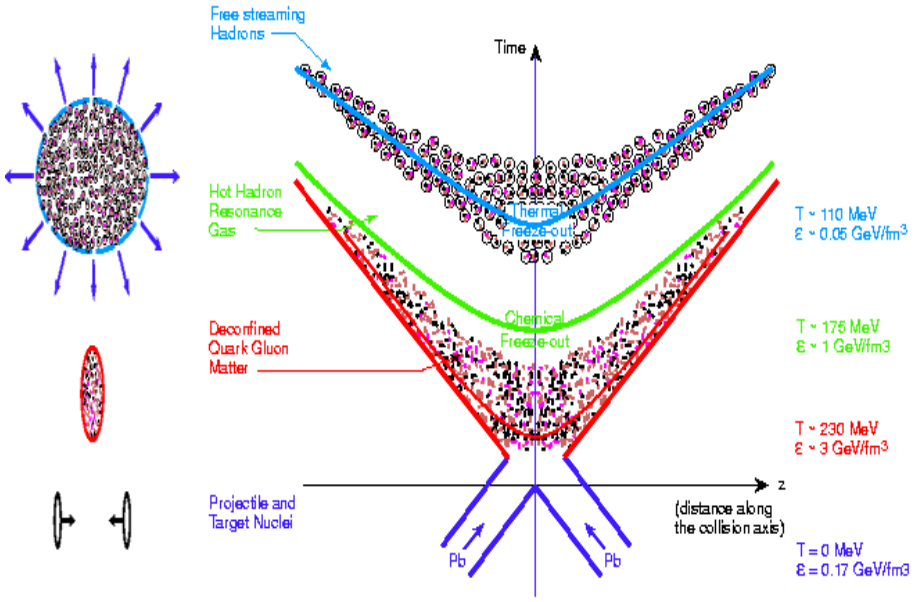

Figure 1.3: Space-time evolution of a Pb-Pb collision.

where A is the transverse area of the interaction region, $\mathrm{d}E_\mathrm{T}/\mathrm{d}y$ is the transverse energy per rapidity unit at mid-rapidity (i.e. an experimentally accessible quantity) and τ_f is the formation time of secondary particles. With such formula one can make an estimate for the energy density for different systems and energies: as an example, in a central Au-Au collision at $\sqrt{s}$ = 200 GeV per nucleon pair, as the one obtained at STAR (RHIC), it is about 15 GeV/fm^3. It has to be pointed out that this value refers to the the initial energy density, i.e. the one available when secondary particles are formed but matter is not thermalised. A more relevant quantity for the purposes of studying QGP is obtained by inserting in Eq. 1.4, instead of τ_f, a realistic guess for the thermalisation time in the above described conditions, i.e. $\tau_{th} \simeq$1 fm/c. This leads to an energy density of about 5 GeV/fm^3, still

much larger than the critical value of 1 GeV/fm^3 (Fig. 1.4): the possibility to reproduce QGP in a laboratory is more than a mere hypothesis.

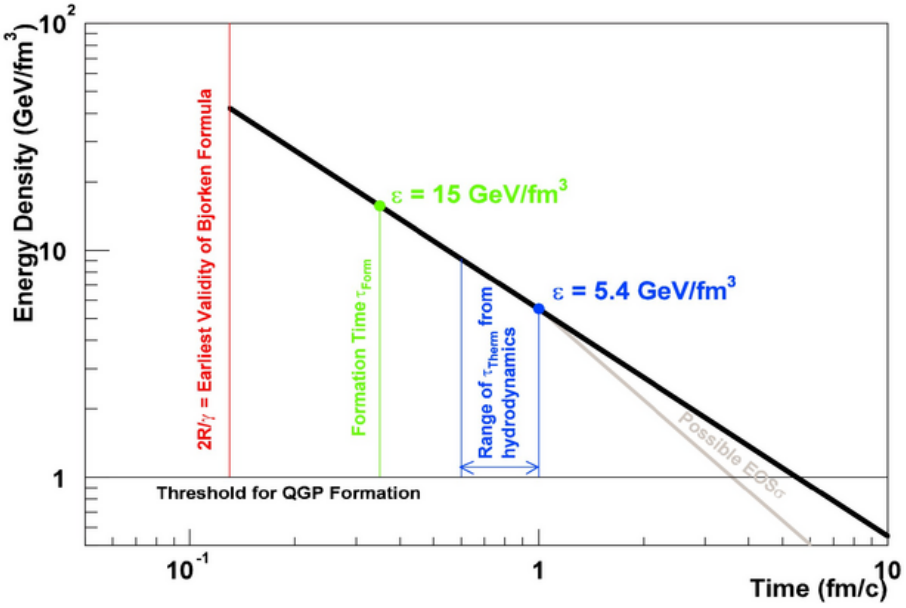

Figure 1.4: Energy density as a function of time in a central Au-Au collision at $\sqrt{s}$ = 200 GeV per nucleon pair, according to Eq. 1.4.

A review of the main relativistic heavy ion accelerators

The above considerations represent a simplified picture of how the transition to QGP can be realized in a laboratory, but nevertheless they can be used to compare the system properties which is formed in the main relativistic heavy ion accelerators that have been running so far. These are:

- Alternative Gradient Synchroton (AGS), running from 1986 to 2000 at the Brookhaven National Laboratories. It accelerated Si and Au ions up to 14.6 GeV per nucleon, on a fixed taget. The centre-of-mass energy per nucleon pair of Au–Au collisions was at most 5 GeV.

- Super Proton Synchrotron (SPS), running from 1986 at CERN (Geneva). It accelerated O, S, In and Pb ions up to 200 GeV per nucleon, on a fixed target. The centre-of-mass energy per nucleon pair of Pb–Pb collisions is up to 17 GeV.

- Relativistic Heavy Ion Collider (RHIC) at the Brookhaven National Laboratories. It has accelerated Cu and Au ions up to 100 GeV per nucleon, in collider mode, so that the center-of-mass energy per nucleon pair in Au–Au collisions is up to 200 GeV.

The Large Hadron Collider at the LHC (CERN) [9, 10] was designed to accelerate and collide protons and heavy ions, as for example Ar or the heavier Pb ions, up to the energy of 2.76 TeV per nucleon (in case of Pb), i.e. a center-of-mass energy per colliding nucleon pair $\sqrt{s_{NN}} = 5.5$ TeV. With a radius of 27 Km, the LHC is the largest collider in the world. It is housed in the tunnel of the previous Large Electron Positron collider, at a depth between 50 and 175 m underground. It will serve as both a proton and ion collider, and proton-ion collider too. The nominal luminosity for pp collisions is of $10^{34}\ s^{-1}cm^{-2}$, while for Pb–Pb collisions it is about $10^{27}s^{-1}cm^{-2}$. The PS and SPS rings are used as injectors for the machine (see fig. 1.5); in particular, the SPS injects protons in the LHC ring with an energy of 450 GeV. The beams are accelerated in two separate rings, with intersections corresponding to the experiments. The first Pb–Pb collision at the LHC, at the energy of $\sqrt{s_{NN}} = 2.76$ TeV, took place in November 2010, and the run lasted over one month. A second campaign, at the same energy and with the

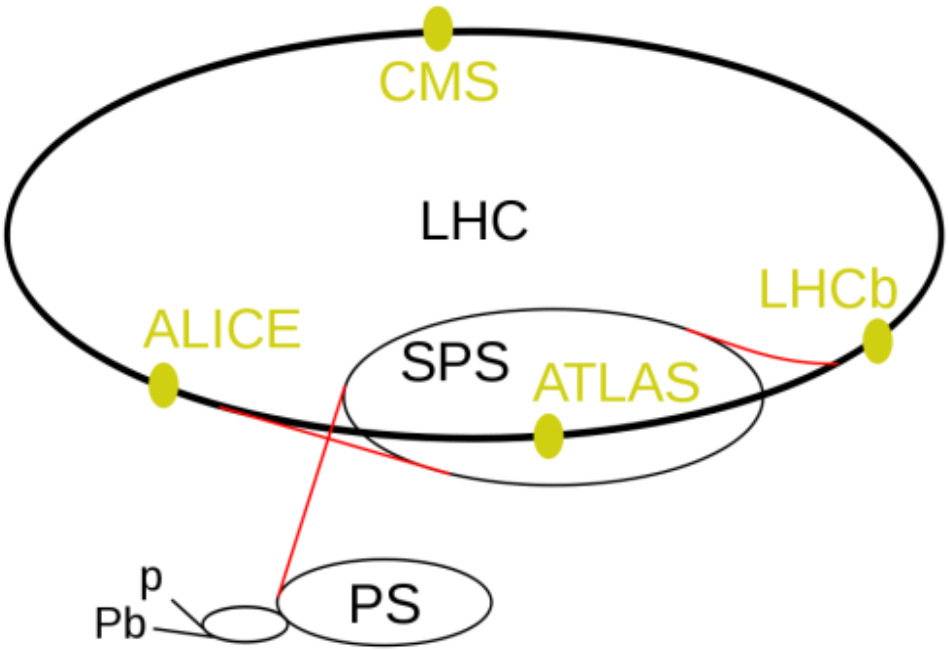

Figure 1.5: The Large Hadron Collider at CERN. The four main LHC experiments (ATLAS, ALICE, CMS, LHCb) and the PS and SPS injector rings are also shown.

same duration, but with a luminosity higher by a factor 20-30, took place in November 2011. The maximum center-of-mass energy of 5.5 TeV for the Pb–Pb collisions should be reached in 2014.

The values of the energy density at t=1 fm/c for SPS, RHIC and LHC top energies, calculated according to Eq. 1.4, are shown in Tab. 1.1.

The nucleon-nucleon centre-of-mass energy for collisions of the heaviest ions at the LHC will exceed that available at RHIC by a factor of about 30 and the energy densities will possibly be high enough to treat the generated QGP as an ideal gas, opening up a new physics domain. Historical experience suggests that such a large jump in energy usually leads to new discoveries. At the LHC, the high energy in the collision centre of mass is

expected to lead to a large energy density and to an initial temperature at least a factor 2 larger than at RHIC. Due to the high initial temperature, also the life time and the volume of the deconfined medium is extended, since it has to expand more while cooling down to the final common freeze-out temperature of $\sim$ 170 MeV. In addition, the large expected number of gluons favours energy and momentum exchanges, thus considerably reducing the time needed for the thermal equilibration of the medium. To summarize, the LHC should produce a hotter, larger and longer living QCD plasma than the previous heavy ion facilities.

Machine	System	$\sqrt{s_{NN}}$ (GeV)	ϵ_{Bj} (GeV/fm^3)	τ_{QGP} (fm/c)	dN_{ch}/dy	Initial T (MeV)
SPS	Pb-Pb	17	2.9	$<$2	400	200
RHIC	Au-Au	200	25	1.5-4.0	650	350
ALICE	Pb-Pb	5500	120	$>$ 10	2000-3000	$>$ 600

Table 1.1: Duration time of QGP and Energy density at t=1fm/c for central A-A collisions, according to the Bjorken formula, for different colliding systems [82].

Experiments at SPS claimed the discovery of the new state of matter [6]. The experiments at RHIC have been studied the properties of the new state: the QGP is a strongly coupled matter, which behaves as a perfect liquid [7, 8]. The LHC heavy-ion program is expected to provide deep insight of this state of matter, investigating what are the characteristics of such state of matter through the analysis of the available experimental probes, among which heavy flavour play a crucial role. They will be discussed in Sec. 1.2.

1.2 Heavy Flavour Physics in heavy ion collisions

Particles containing charm and beauty quarks are among the most effective probes of the medium formed in heavy-ion collisions. They are classified as 'hard' probes because, given their large mass ($M_{beauty} \sim 4.8$ GeV, $M_{charm} \sim 1.2$ GeV), they originate from interactions with high transferred momentum ($Q^2 \geq 4M_{c,b}^2$). Their production mostly occurs at the initial stage of the collision, in scattering processes between partons in the colliding nuclei, typically through $q\bar{q}$ annihilation and gluon fusion. For charm, the timescale of the production process is on the order of $1/(2m_q) = 1/(2.4 \text{ GeV}) = 0.1$ fm/c, for beauty being even shorter, to be compared with the QGP formation time (∼1 fm/c after collision) and the fireball lifetime ($\gtrsim$10 fm/c). They are produced before deconfinement sets in, thus before the formation of the QGP, and they can travel throughout the whole QGP lifetime, interacting with the deconfined medium, so they can carry information about the medium density. Moreover, models describing hadronisation through final state fragmentation tend to favor light quark production (ratio of 1 c quark to 10^{11} u,d quarks): thus, production of charm and beauty particles in the final state is negligible and cannot shadow medium effects.

Heavy quark production is a high momentum transfer process: thus, its elementay cross section can be calculated in perturbative QCD, since the strong coupling constant $\alpha_s(Q^2) \propto \frac{1}{\ln \frac{Q^2}{\Lambda_{QCD}^2}}$ (assuming $\Lambda_{QCD} = 200$ MeV) is sufficiently low at this momentum scale. The experimental results (in pp)

can then be confronted with pQCD predictions which have typical accuracies of order 10% or worse.

The advantage of charm with respect to beauty is that the production cross section is larger (see Fig. 1.6) thus, the reconstruction of charm particles via their hadronic decays is subject to smaller statistical errors.

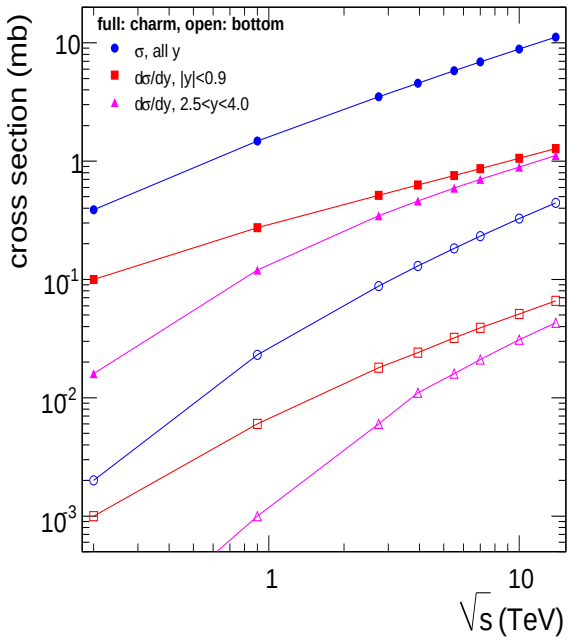

Figure 1.6: Charm and Beauty Production cross section. The expected cross section at LHC in Pb–Pb collisions for charm is about 3 mb, and for beauty is 0.1 mb at the nominal 5.5 TeV center of mass energy per nucleon.

The detection of charmed hadrons is ideally performed in exclusive channels by reconstructing the invariant mass of the particle. In order to extract the signal on top of the large combinatorial background, the tracks of candidate decay products are requested to not point to the primary vertex, where the charmed hadron is produced, but to a displaced vertex where the

decay is assumed to have taken place: this is called a secondary vertex. The capability to detect open charm particles is mainly driven by the ability to separate secondary from primary vertices.

In order to properly reconstruct primary and secondary vertices, a good position resolution in track reconstruction is crucial. More specifically, the measurement of the impact parameter, defined as the minimum distance between the primary vertex and the back extrapolated track trajectory, must be performed with a resolution of a few tens of μm, since the typical impact parameter values for, e.g., the D^0 decay products is of about 100 μm.

1.2.1 In-Medium Energy Loss

The comparison of heavy flavour production in proton-proton and heavy-ion collisions allows to probe the properties of the high-density QCD medium formed in the latter kind of collisions and to study the mechanism of in-medium partonic energy loss.

The experimental observable used to evaluate the influence of nuclear effects is the *Nuclear Modification Factor*, defined as follows:

$$R_{AA}(p_T) = \frac{\mathrm{d}^2 N_{AA}/\mathrm{d}p_T\mathrm{d}y}{N_{coll} \times \mathrm{d}^2 N_{pp}/\mathrm{d}p_T\mathrm{d}y}$$

where $\mathrm{d}N_{AA}/\mathrm{d}p_T$ and $\mathrm{d}N_{pp}/\mathrm{d}p_T$ are the observed differential yields in nucleus-nucleus and proton-proton collisions, respectively, and N_{coll} is the number of estimated binary collisions per nucleus-nucleus collision. This variable should be unity if a nucleus-nucleus collision was just a superposition

of binary nucleon-nucleon collisions without any nuclear effect. The study of the p–A collisions is also fundamental to disentangle cold nuclear matter effects from genuine medium effects, due to the fact that a nucleon inside the nucleus may behave differently than a free nucleon.

1.2.2 Probing QGP with heavy flavour

While traversing the dense matter produced in nucleus-nucleus collisions, the initially-produced hard partons lose energy, strongly interacting with the medium, mainly on account of multiple scattering and medium-induced gluon radiation: their transverse momentum spectra are then expected to be shifted towards lower p_T ('quenching'). Several theoretical models have been developed to study the in-medium energy loss. For instance, the "BDMPS" model ([11, 12]) assumes that, when an energetic parton crosses the medium and experiences multiple scattering, the gluons in its wave function may acquire a transverse momentum q_T with respect to the parton direction and may eventually be radiated. In this scenario, the average energy loss $< \triangle E >$ is given by:

$$< \triangle E > \propto \alpha_s C_R \hat{q} L^2 \tag{1.5}$$

Namely, it is proportional to:

- $\alpha_s C_R$, where C_R is the Casimir factor that describes color coupling. It is equal to 4/3 for quarks and to 3 for gluons. Therefore, this factor

is larger by factor of 9/4 for gluons than for quarks;

- transport coefficient $\widehat{q}$. It is related to the average squared transverse momentum transferred to the parton and it is proportional to the density of scattering centers in the medium;

- the square of the length L traveled in the medium.

The understanding of the mechanism of in-medium energy loss induced on the hard partons that are produced in the initial hard scattering processes is one of the most interesting reasons for addressing charm and beauty production in heavy-ion collisions. In fact, the in-medium energy loss is a distinctive features of the hot and dense medium formed in heavy-ion collisions. In-medium energy loss is expected to depend on the parton nature and on the parton mass. Therefore, it is interesting to compare the nuclear modification factors for gluons, light and heavy quarks. This because eq. 1.5 leads to a different average energy loss for gluons, light quarks and heavy quarks. The difference between gluons and quarks, that is due to their different Casimir factors, causes larger suppression of particles coming from gluon fragmentation with respect to those originating from quarks. A large fraction of high p_T light flavoured hadrons at the LHC (and RHIC) energy originates from hard scattered gluons, while charmed and bottom mesons mainly originate from the fragmentation of heavy quarks directly produced in the early stages of the collision. Consequently, this effect should be seen as larger suppression of high p_T light mesons with respect to the charmed and

beauty ones. Thus, for the D meson, the expectation is that $R_{AA}^{D} > R_{AA}^{\pi}$.

The mass of the quark is believed to determine the energy loss as well, due to the so called "dead-cone effect", which predicts a suppression of the gluon radiation (gluonsstralhung) at forward angles Θ smaller than $\Theta_0 = m/E$: since Θ_0 is larger for heavy quarks than for light quarks, the cone where gluon radiation is forbidden is larger for heavy quarks. Therefore, it has been argued that for beauty quarks, because of their very large mass, the radiative energy loss should be lower than for charm quarks and lighter ones. As a consequence of the above arguments, the prediction for the energy loss is $\triangle E_{gluon} > \triangle E_{charm} > \triangle E_{beauty}$ and a hierarchy between the nuclear modification factors of B and D mesons and light hadrons is expected, such that $R_{AA}^{B} > R_{AA}^{D} > R_{AA}^{\pi}$.

Theoretical models based on perturbative QCD with the inclusion of radiative parton energy loss predict for charm mesons a suppression factor of 3 - 5 and a significantly smaller suppression for B mesons (see figure 1.7 [13]). The mass dependence of energy loss is more pronounced for the beauty mesons, as seen in figure 1.8 [19].

Mass and colour charge dependence can be investigated experimentally considering the ratio between the nuclear modification factors of heavy and light quarks: $R_{D/h} = R_{AA}^{D}(p_T)/R_{AA}^{h}(p_T)$ which is shown in figure 1.9 [19].

The mass effect is modest but more pronounced at moderately low transverse momenta. At sufficiently high p_T (above $\sim$ 10 GeV/c) the c

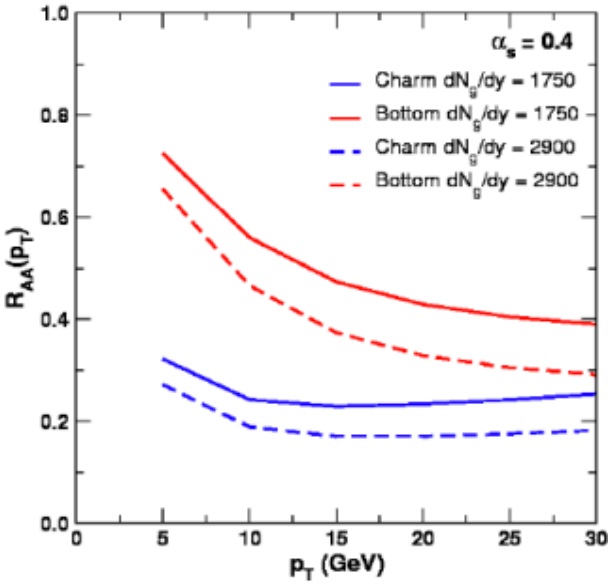

Figure 1.7: Prediction for R_{AA} vs p_T for D mesons (blue) and B mesons (red) in Pb-Pb collisions at the LHC, from radiative + collisions energy loss (DGHW) [13]

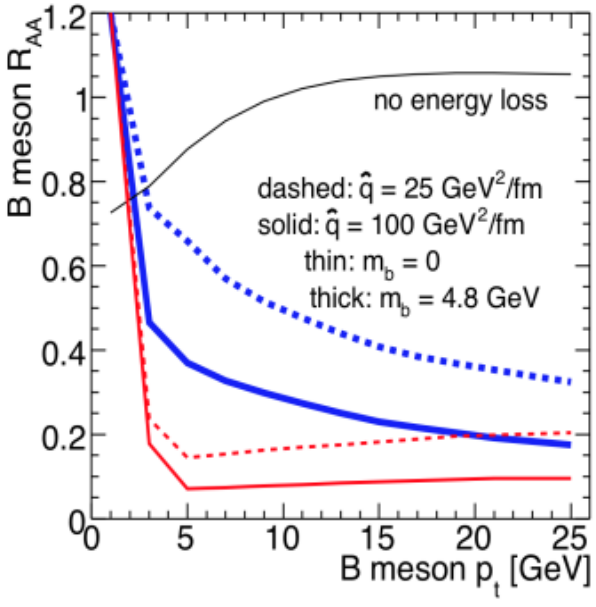

Figure 1.8: Mass dependence of B meson R_{AA} in Pb-Pb collisions at the LHC from radiative energy loss (ASW) [19]

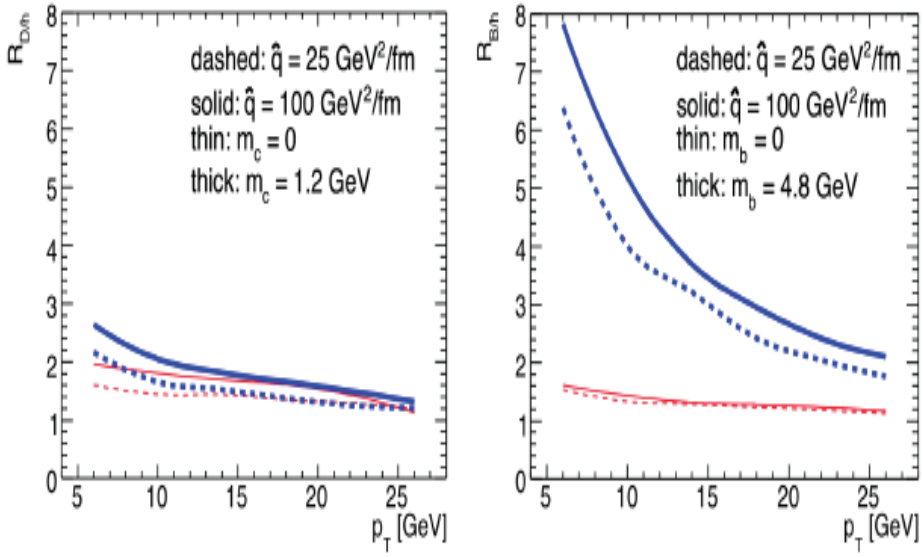

Figure 1.9: Heavy-to-light R_{AA} ratios as predicted by the radiative energy loss mechanism (ASW) for R^D_{AA}/R^h_{AA} (left) and R^B_{AA}/R^h_{AA} (right)[19]

quark starts to behave essentially as a massless parton. However, the ratio is not expected to tend to unity, due to the color charge dependence of energy loss.

Even more interesting is the ratio of the beauty to charm nuclear modification factor: $R_{B/D} = R^B_{\rm AA}(p_T)/R^D_{\rm AA}(p_T)$, which is shown in the left panel of figure 1.10 [19].

Here, the ratio shows a strong deviation from one in particular at moderately low p_T, decreasing only rather slowly for increasing p_T. Predictions for the ratio $R_{D/B}$, which is equal to $1/R_{B/D}$, obtained with either pQCD-based calculations or the AdS/CFT mechanism [14] are shown in the right panel of figure 1.10. This ratio has the advantage of magnifying the

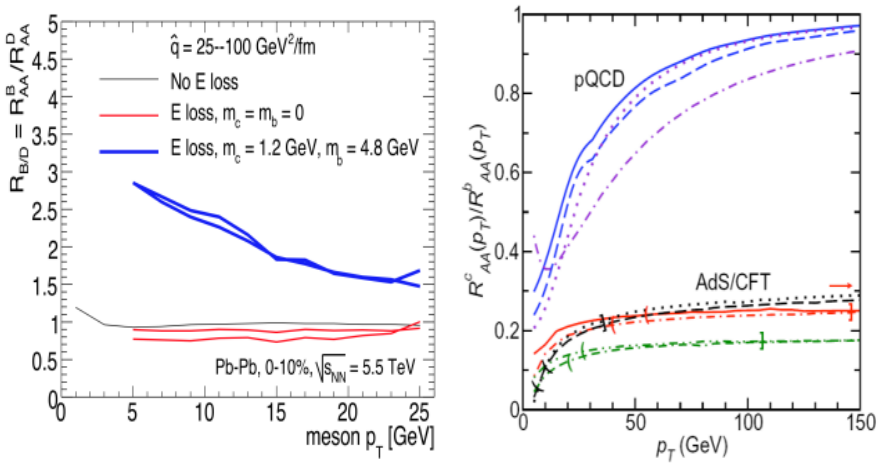

Figure 1.10: Prediction for the comparison of charm and beauty R_{AA} in Pb-Pb collisions at the LHC. Left side: R^B_{AA}/R^D_{AA} vs p_T from radiative energy loss (ASW))[19]. Right side: R^D_{AA}/R^B_{AA} vs p_T from radiative energy loss (pQCD) and AdS/CFT [14]

differences in the mass and p_T dependence of pQCD and AdS/CFT models. While small differences are present among pQCD models and among AdS/CFT models, the two classes of models yield largely different predictions irrespectively of their input parameters.

1.3 Thermalization

Establishing the existence of a thermalized system is an important prerequisite for a new state of matter to be formed. Hadron abundances measured in relativistic heavy ion collisions have been successfully described using statistical thermal models [15, 16, 17]. The inference from these studies is that the system is in chemical equilibrium with a chemical freeze-out temperature of $T_{chem} \sim 170$ MeV, independent of collision system and colli-

sion centrality. This temperature agrees with the value for the quark-hadron phase transition temperature predicted by Lattice QCD. The system expansion and hadronic re-scattering may still continue after chemical equilibration. The temperature at kinetic freeze-out, when hadrons stop interacting, is reflected in the slopes of the hadron momentum distributions and it can be extracted by comparing the measured spectral shapes of identified hadrons to a hydrodynamic model that has been tuned to reproduce the data. The model shows that it takes about 9-10 fm/c until the fireball has become sufficiently dilute to completely convert to hadronic matter, and another 7-8 fm/c to completely decouple at a temperature of $T_{kinetic} \sim 100$ MeV. The success of the statistical thermal models and the hydrodynamic description of single particle spectra and yields implies that the matter produced at RHIC and LHC has reached thermal equilibrium at some early stage of its evolution. The thermalization process itself can only be assessed using a microscopic description of the pre-equilibrium system dynamics. Microscopic transport models [18] need experimental input to constrain the transport coefficients in the medium. Heavy quarks are a good probe of the transport properties of the medium. Due to the large c-quark mass, the charm equilibration time is expected to be about a factor of 5 larger than the light quark equilibration time. Theoretically, the charm diffusion coefficient has been related to the charm energy loss and momentum broadening. Utilizing transport theory, these quantities can then be used as an input for the calculation of charm elliptic flow, thus creating a relation between an experimentally accessible

quantity and the diffusion coefficient. Themalization is thus a prerequisite of thermal models, coalescence and collective behavior, as for example the elliptic flow, which will be treated in the following.

Measurements of open charm production and flow data in heavy ion collisions are challenging due to the small production cross-sections and the experimental limitations on charm particle identification.

1.4 Hadronization: fragmentation vs. recombination

In pp collisions a parton which scatters in a hard collision with another parton, hadronizes in the vacuum through fragmentation. Does it happen the same in Pb–Pb collisions? It has also been suggested [20] that, if the energy loss is large, it could happen that partons become slow enough to undergo hadronization via recombination inside the medium. In particular, at moderate p_T values, the hadron production via the recombination of lower p_T partons from the thermal bath, has been predicted [21] to be competitive with production from the fragmentation of higher p_T scattered partons. It has been suggested [22] that the need for substantial recombination to explain observed hadron yields and flow may be taken as a signature of QGP formation. In order to explain observed features of RHIC collisions, the recombination models [20, 21] assume that coalescence proceeds via constituent quarks, whose number in a given hadron determines its production rate. The following scheme can simply explain the hadronization via recombination:

- $q + \bar{q} \rightarrow$ mesons
- $q + q + q \rightarrow$ baryons
- $\bar{q} + \bar{q} + \bar{q} \rightarrow$ anti-baryons

where q are the constituent quarks. They are presumed to follow a thermal (exponential) momentum spectrum and to have a collective transverse velocity distribution. This picture leads to predictions about the baryon and meson production rates, with the former depending on the spectrum of thermal constituent quarks (and antiquarks) at roughly one-third the baryon (anti-baryon) p_T, the latter being determined by the spectrum at one-half the meson p_T . Indeed, the recombination model was introduced in the RHIC context, to explain an anomalous abundance of baryons with respect to mesons observed at moderate p_T values. Results from RHIC have already shown that there is an enhanced baryon/meson ratio in the intermediate transverse momentum range ($2 <$ pT $<$ 6 GeV/c) in Au + Au collisions at both $\sqrt{s_{NN}} = 130$ and 200 GeV/c: the first strong hints came from the Λ/K ratio and then from other baryon to meson ratio. For the case of heavy hadrons it has not been measured. These findings, for light hadrons, have been later confirmed by ALICE, as it will be shown in chapter 3.

Furthermore, more exotic models [23] predict that, if coalescence process occurs statistically at the hadronization temperature, there is a finite chance that two or even three heavy quarks coalesce into the same particle, thus giving rise to multiply heavy flavoured hadrons, particularly baryons.

This phenomenon is likely to occur only if heavy quarks get very close to thermal equilibrium reshuffling over a large region because high momentum quarks, most likely, will hadronize into different particles unless two or three of them emerge very close in momentum from the hard process. The ultimate reason of this effect is that the average multiplicity of heavy quark pairs increases faster than soft hadrons multiplicity as a function of centre-of-mass energy. This is in turn related to the volume of the system at freeze-out. Consequently, the system gets denser in heavy quarks at chemical freeze-out as energy increases and so does the chance of formation of multiply heavy flavoured hadrons. Therefore, an enhanced production rate, w.r.t pp collisions, of these objects relative to singly heavy flavoured hadrons (like B's or D's) is distinctive of heavy ion collisions and can be used as a probe of thermalization of heavy quarks within the QGP, hence as a unique signal of the QGP itself.

1.5 Flow

The azimuthal distribution of particles in the plane perpendicular to the beam direction is also sensitive to the properties of QGP.

At the beginning of a non central heavy ion collision, the spatial distribution of the colliding matter resembles an ellipsoid due to the incomplete overlap of the two colliding nuclei. Any strong scattering in this early stage converts the spatial anisotropy into a momentum anisotropy which is observable as an elliptic flow of the emitted hadrons.

Elliptic flow is a collective motion pattern superimposed to the chaotic thermal motion. In non-central collisions a preferred direction in the transverse plane exists and it is defined by the direction of the impact parameter, which is defined by the distance between the straight-line trajectories of the centers of the two nuclei before their interaction (see fig. 1.11). As a consequence, the azimuthal distribution of the produced particles may result to be anisotropic with respect to the reaction plane (defined by the impact parameter itself and the beam axis). This initial spatial asymmetry is converted via multiple collisions into an anisotropic momentum distribution of the produced particles.

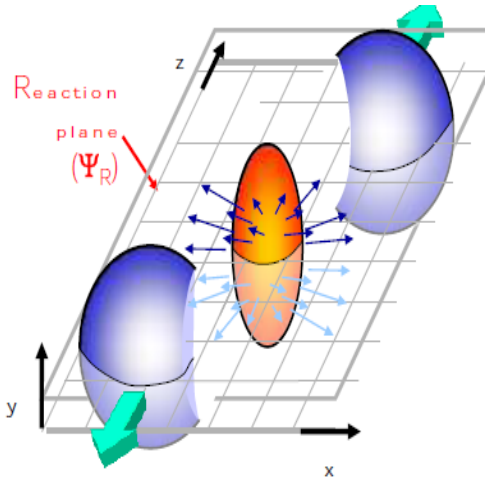

Figure 1.11: Initial spatial azimuthal asymmetry in a non-central nucleus-nucleus collision.

The particle azimuthal distributions relative to the reaction plane are usually written in the form of Fourier series as:

$$\frac{dN}{d\phi} = \frac{1}{2\pi}[1 + \sum 2v_n cos(n(\phi - \psi_R))]$$

where ϕ is the azimuthal angle of the particle, ψ_R is the angle of the initial state spatial plane of symmetry (the reaction plane), and n is the order of the harmonic. The Fourier coefficients are defined as $v_n =< cos[n(\phi - \psi_R)] >$.

The first coefficient of the series, v_1 is called directed flow, while the second coefficient, v_2, is called elliptic flow. Non-zero directed flow implies a preferred direction for particle emission, either parallel ($v_1 > 0$) or anti-parallel ($v_1 < 0$) to the impact parameter. For symmetry reason, directed flow is equal to zero at mid-rapidity. However, it can affect the particles produced in the forward rapidity region, as well as the spectator nucleons.

The amount of elliptic flow can be quantified via the second Fourier coefficient v_2 [24]. The measurement of v_2 of heavy-flavoured mesons gives additional information on the degree of thermalisation of the plasma. Elliptic flow can also be affected by relative contribution of different hadronization mechanisms. According to the study of Molnar [25] in the case of fragmentation, charmed hadron elliptic flow is essentially identical to the charm quark v_2. On the contrary, if hadronization is done via coalescence, hadron elliptic flow is approximately the sum of the constituent flows. If the observed hadronic elliptic flow values in this momentum range result from coalescence of collectively flowing constituent quarks, then one can expect a similarly simple baryon vs. meson relationship [21]: the baryon (meson) flow would be 3 (2) times the quark flow at roughly one-third (one-half) the baryon p_T. Within the coalescence models, the constituent quarks carry their own substantial azimuthal anisotropy, which is then summed to give the hadron

v_2. Such observation leads to a prediction of higher elliptic flow at RHIC energy in the region $2.5 < p_T < 4$ GeV/c, if coalescence plays substantial role in hadronization.

1.6 The ALICE Experiment at LHC

ALICE is one of the four big experiments running at LHC. It is the dedicated experiment to study the collisions of heavy ions.

The ALICE physics program includes data-taking with many different colliding systems: though the focus is undoubtedly on Pb–Pb collisions, nevertheless measurements with each colliding system are of crucial importance, for different reasons:

- data-taking in Pb–Pb collisions will provide access to the higher energy density regime ever studied in a laboratory;
- data-taking in pp collisions will provide a baseline to be compared with A–A data;
- data-taking in p-A collisions will allow to disentangle "cold nuclear matter effects" from genuine medium effects.

After almost 20 years of preparation, ALICE took the first data with proton collisions in November 2009. The total pp data sample collected at 7 TeV (900 GeV) corresponds to some 700 M (7 M) minimum bias (MB) triggers, 50 M muon triggers and about 20 M high multiplicity events. In

addition, a very short test run was taken at 2.36 TeV with only a small subset of detectors being read out. First heavy ion collisions at 2.76 TeV/nucleon took place in November 2010, yielding 30 M nuclear MB interactions on tape. A second round was run in November 2011 at the same energy and increased luminosity of a factor 20-30: about 130 M events have been recorded. The first ALICE results on global event characterization (such as charged particle multiplicities, elliptic flow and high p_T suppression) are summarized in chapter 3.

1.6.1 The ALICE detectors

A schematic view of the detector is shown in figure 1.12.

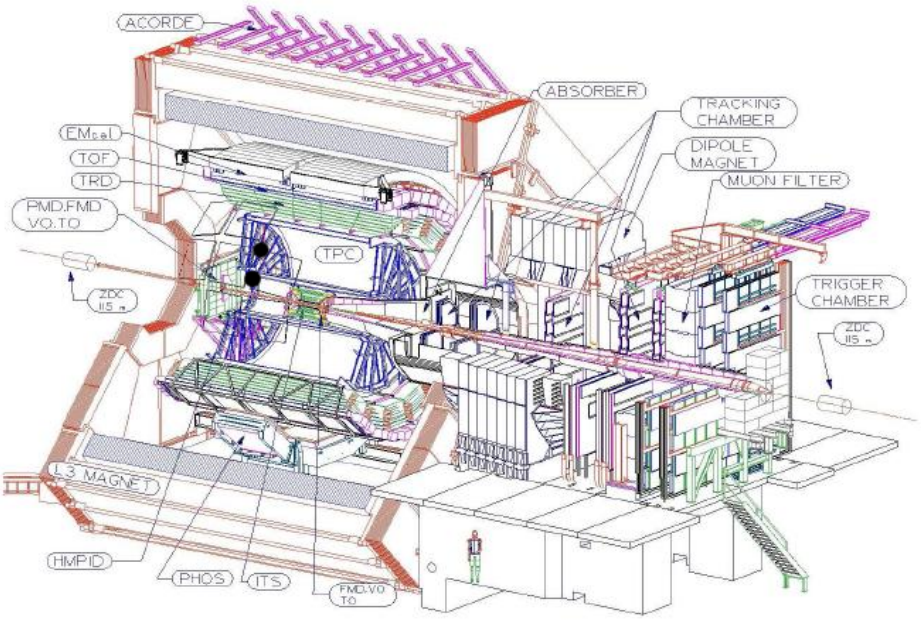

Figure 1.12: Layout of the ALICE experiment with all systems in evidences.

ALICE consists of a central part, which measures hadrons, electrons

and photons, and a forward spectrometer to measure muons. The central part, which covers polar angles from 45^o to 135^o over the full azimuth, is embedded in the large L3 solenoidal magnet (B = 0.5 Tesla). The main tracking detector are the Inner Tracking System (ITS), constituted of high-resolution silicon detectors (two layers each of pixel, drift, and double-sided strips), and the Time Projection Chamber (TPC). Externally to the TPC, there are the Transition Radiation Detector (TRD) and Time Of Flight (TOF) detectors. The TPC, playing a special role in the ALICE tracking and reconstruction, and TOF, designed for the identification of particles with $p_T < 3$ GeV/c and crucial for charm hadron PID, will be described in the following section. The ITS will be described in details in the next chapter. The other detectors in the central barrel are the High Momentum Particle Identification (HMPID), consisting of an array of ring-imaging Cherenkov counters, the Transition Radiation (TRD) counters, for electron identification, and two single-arm electromagnetic calorimeters (high resolution PHOS and large acceptance EMCAL). The forward muon arm (2^o - 9^o; $2.5 < \eta < 4$) consists of a complex arrangement of absorbers, a large dipole magnet (3 Tm field integral), and 14 stations of tracking and triggering chambers. Several smaller detectors for triggering and multiplicity measurements (ZDC, PMD, FMD, T0, V0) are located at small angles. The main design features include a robust and redundant tracking over a limited region of pseudorapidity, designed to cope with the very high particle density of nuclear collisions, a minimum of material in the sensitive tracking volume ($\approx 10\%$ radiation length between

vertex and outer radius of the TPC) to reduce multiple scattering, and several detector systems dedicated to particle identification over a large range in momentum. The layout of the ALICE detector and its eighteen different subsystems are described in detail in [26]. The experiment is fully installed, commissioned and operational, with the exception of two systems (TRD and EMCAL) which were added more recently. Both systems had about 40% of their active area installed during 2010; the EMCAL was completed during the winter shutdown 2010/11 and the TRD will be completed early next year.

1.6.2 Time Projection Chamber

The TPC is the central tracking detector of the ALICE apparatus [27]. A schematic view of the detector is shown in figure 1.13.

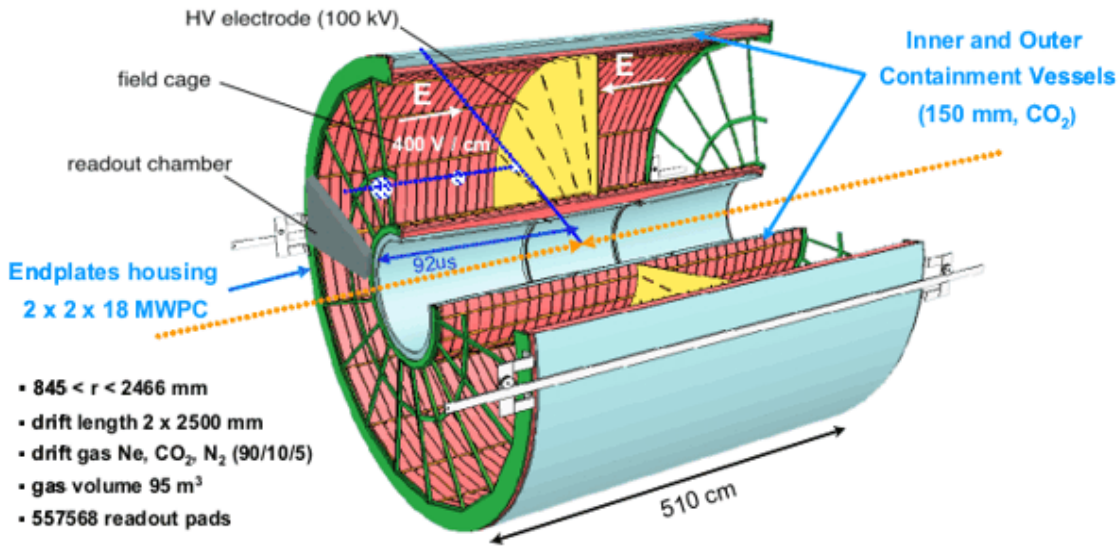

Figure 1.13: Schematic view of the ALICE TPC

Within a total active length of 510 cm, it covers a pseudo-rapidity range of $|\eta| < 0.9$ for particle tracks with full radial track length and up to $\eta = 1.5$ for reduced track length. It covers the full azimuth, except for the dead zones. The inner radius is determined by the maximum acceptable hit density (0.1 cm^{-2}) and is about 85 cm, the outer radius is 250 cm and is determined by the length required to have a high p_T resolution and a $\mathrm{d}E/\mathrm{d}x$ resolution better than 5-7%. It has a conventional design in the overall structure but is innovative in many aspects. It consists of a large cylindrical field cage, filled with 90 m^3 of $Ne/CO_2/N_2$ (90/10/5), needed to optimize the drift velocity, to allow a low electron diffusion and a low radiation length. The drift region covers a distance up to 2.5 m on either side of the central electrode to the end plates. Multi-wire proportional chambers with cathode pad readout are mounted into 18 trapezoidal sectors at each end plate. The field cage is operated at high voltage gradients because of the gas mixture used, with a high voltage of 100 kV at the central electrode that results in a maximum drift time of about 90 μs, which is the limiting factor for the luminosity in ALICE. The corresponding interaction rate, sustainable from the TPC, is about 8 kHz, of which about 10% can be central collisions. The TPC, together with others detectors of the central barrel, provides charged particle momentum measurements with good two-track separation, particle identification and vertex determination. It has been optimized for Pb–Pb expected luminosity and the initially foreseen charged-particle multiplicity density $\mathrm{d}N_{\mathrm{ch}}/\mathrm{d}\eta = 8000$, that means about 20.000 primary and secondary

particles in the TPC acceptance. With its resolution, the TPC should be also able to identify particles in the region of the relativistic rise momenta, up to 50 GeV/c. Despite its data volume and low speed, only such a tracking detector can guarantee the desirable performance at the order of 20.000 particles within the acceptance.

1.6.3 Time Of Flight

Particle identification is one of the distinctive features of the ALICE experiment. Besides the TPC and the ITS, the TOF detector is specifically built to this purpose [28]. Its task is to provide hadron separation in the momentum range from 0.5 GeV/c, to about 3 GeV/c, hence in a range where the $\mathrm{d}E/\mathrm{d}x$ technique is no longer effective. PID in this momentum range allows the study of the kinematical distributions of the different particle types on an event-by-event basis in heavy ion collisions. Moreover, given the large mass of the charm quark, the decay products of D mesons have typical momenta of the order of 1-2 GeV/c; therefore the Time of Flight, with K/π separation up to 2.5 GeV/c, is very effective for the reconstruction of exclusive decays of D mesons and Λ_c baryons in hadronic channels. It is a large area array of Multi-gap Resistive-Plate Chambers (MRPC), a new type of gas detector developed to fulfil the requirements of having a large number of channels to keep the occupancy low, an affordable system and a time resolution better than 100 ps. It is positioned on a cylindrical surface that covers the central barrel ($\eta < 0.9$) over an area of 140 m^2 with 160.000

individual cells at a radius of about 4 m. It has an internal radius of 370 cm and an external radius of 399 cm. When a charged particle traverses the detector, it ionizes the gas producing an avalanche which is driven to the electrodes by the electric field. The detector consists of 90 modules grouped into 18 supermodules. A view of one supermodule is shown in Figure 1.14.

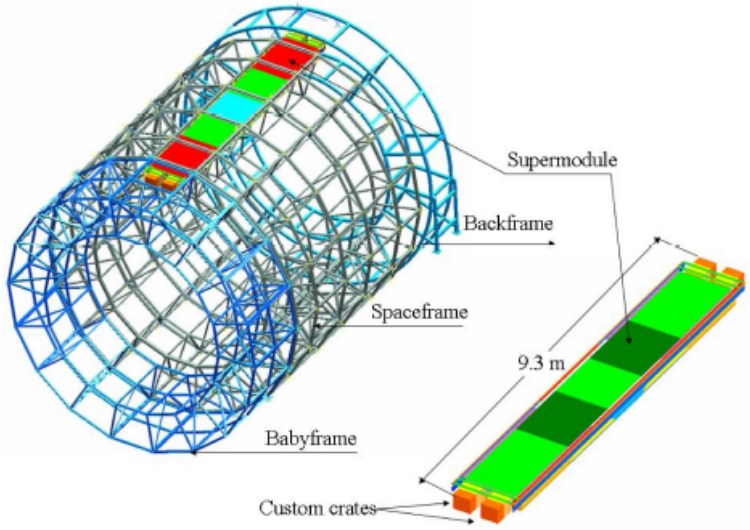

Figure 1.14: Schematic view of the ALICE TOF and drawing of one TOF supermodule, consisting of 5 modules.

Chapter 2

The Inner Tracking System of ALICE

In this chapter the layout of the Inner Tracking System (ITS) is described in details. Then, the present status of the detector is presented, and its performances in pp and Pb–Pb collisions are discussed. Finally, an analysis of the detector efficiency is presented: such study was performed in order to monitor the status of the detector and to tune the Monte Carlo simulation tool according to the observed operational conditions. The detector efficiency of each layer of the ITS has been evaluated in different periods of data taking in 2010. These studies were also important to evaluate the contribution to the tracking precision from each module (elementary cell) of the layers and to test the alignment.

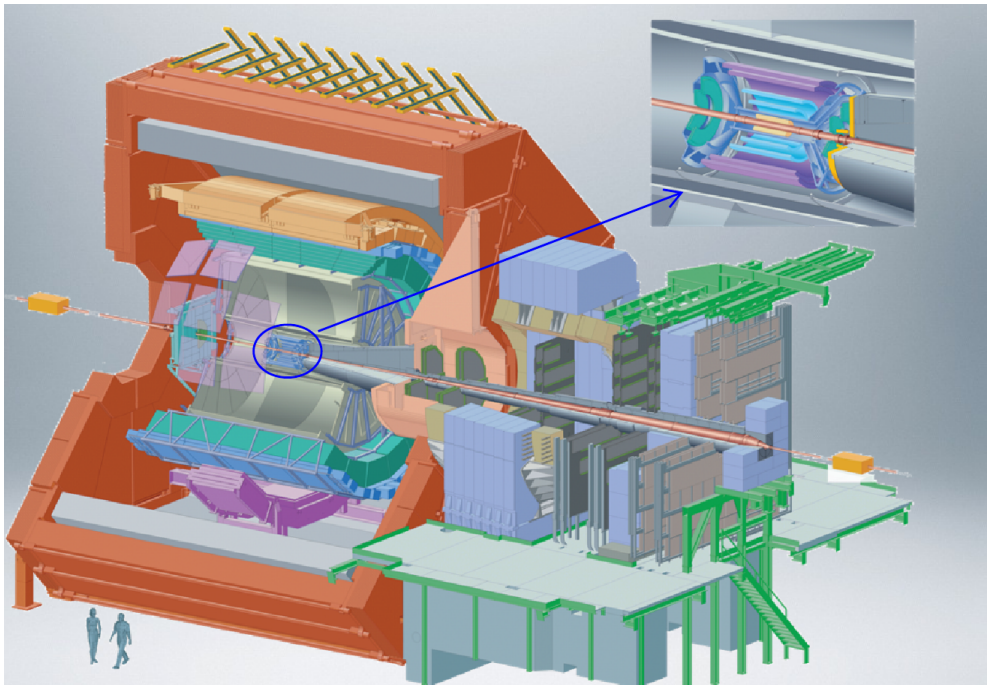

Figure 2.1: Layout of the ALICE experiment. The inset shows a zoom of the ITS.

2.1 ITS: the vertex detector of ALICE

The main tracking detectors of the ALICE set-up in the central barrel are the Inner Tracking System (ITS), a six-layer silicon vertex detector, and the Time-Projection Chamber (TPC).

The ITS, as well as the other detectors, are localized using the ALICE Global Reference system, which has the z axis on the beam line, the x axis in the LHC (horizontal) plane, pointing to the center of the accelerator, and the y axis pointing upward. In the transverse plane, the cylindrical coordinates r and ϕ are often considered: they localize, respectively, the radial coordinate of the point with respect the center of axis, and the azimuthal angle.

The ITS is the detector closest to the interaction point. Its location in ALICE is highlighted in Figure 2.1, where a zoom is drawn in the right upper part of the figure.

The ITS (Fig. 2.2) consists of six silicon detector layers: the two innermost layers are the Silicon Pixel Detectors; the two intermediate layers are the Silicon Drift Detectors; the two outermost layers are the Silicon Strip Detectors. They are located at radii between 3.9 and 43 cm from the beam axis, covering the pseudo-rapidity range $|\eta| < 0.9$. The SPD detector has an extended pseudo-rapidity $|\eta| < 1.98$, to provide a continuous coverage for the measurement of charged multiplicity.

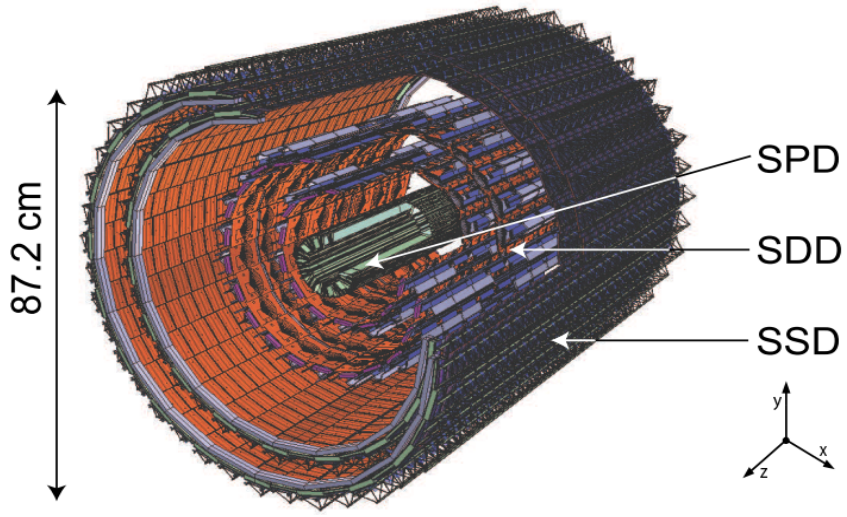

Figure 2.2: Prospective section of the Inner Tracking System (ITS) in ALICE. The Silicon Pixel Detector (SPD), Silicon Drift Detector (SDD) and Silicon Strip Detector (SSD) are shown.

The innermost radius is the minimum allowed by the presence of the beam pipe, whose external radius is 2.9 cm. The outermost radius of the ITS is a compromise between the requirement to match at better the tracks from

the ITS to the TPC (and vice versa) and the space to be left between the TPC and the ITS for the services. One of the main feature of such a detector is its very low material budget, which in terms of radiation length is X/X_0= 7% in total. A small material budget is fundamental in the reconstruction of low momentum tracks, because multiple scattering affects the spatial and the momentum resolution.

The ITS has been designed to track charged particles in the high density track environment normally produced with central Pb–Pb collisions, to perform primary and secondary vertex reconstruction, multiplicity measurement and particle identification of low momentum particles down to $p_T \sim 100$ MeV/c.

2.1.1 Impact parameter and transverse momentum resolution: physics performance

A precise tracking is essential to reconstruct and separate the secondary vertices of heavy-flavoured hadron decays from the primary vertex. The physics performance mainly depend from the impact parameter resolution d_0 and momentum resolution, which are directly connected to the design of the detector.

We consider separately the two projections of the impact parameter in the plane transverse to the beam direction and along the beam direction, respectively:

$$d_0 = q(\rho - \sqrt{(x_v - x_0)^2 + (y_v - y_0)^2}) \tag{2.1}$$

and

$$d_{0,z} = z_{track} - z_v$$

where ρ and (x_0, y_0) are the radius and the center of the track projection in the transverse plane, (x_v , y_v , z_v) is the position of the primary vertex, and z_{track} is the z position of the track after it has been propagated to the point of closest approach in the transverse plane to the primary vertex.

The impact parameter resolution is a convolution of the error in the vertex resolution and the track position resolution:

$$\sigma_{d_0} = \sigma_{vertex} \oplus \sigma_{trackposition}$$

The detector segmentation determines the intrinsic resolution and it is important especially for particles at high transverse momentum. The p_T dependence of the impact parameter resolution reflects what is expected from a contribution due to the spatial precision of the detector added to a contribution due to the multiple scattering:

$$\sigma_{d_0} = \sigma_{det.res.} \oplus \sigma_{scattering}$$

In this decomposition, the first term can be reasonably assumed to be independent of the particle momentum and direction, while the second

depends on the momentum and on the amount of material crossed by the particle. In fact when a charged particle is traversing the materials of a tracking system, it undergoes small deviations of the track, due to Multiple Coulomb Scattering. The effect is described by the theory of Moliere [29]. It shows that, by traversing detector's material of thickness s, the particle undergoes successive small-angle deflections, symmetrically distributed around the incident direction. The Moliere distribution of the scattering angle can be approximated by a Gaussian. The width of this distribution is the root mean square of the scattering angle

$$\theta_0 = \frac{13.6\,\mathrm{MeV}}{p\beta c} z_c \sqrt{\frac{s}{X_L}} [1 + 0.038 \ln(\frac{s}{X_L})]$$

where p, β and z_c are the momentum, velocity and charge number of the incident particle, and X_L is the radiation length of the scattering medium.

If we consider the simplified case of particles moving in the transverse plane, the material thickness can be taken as constant and the multiple scattering term should be proportional to $1/p_T$. Thus the impact parameter resolution can be expressed as

$$\sigma_{d_0} = a + b/p_T$$

where a depends from the intrinsic resolution of the sensor, and b from the total material budget.

The resolution on the impact parameter in the transverse plane is completely determined by the ITS (precisely the first two layers of the ITS), in particular the low material budget of the SPD layers and their intrinsic resolution are the parameters that mainly contribute to the good d_0 resolution, which is less than 60 μm for $p_T > 1$ GeV/c. In section 2.4 will be shown the performance plot of the impact parameter resolution in data.

2.2 The ITS subdetectors

The high particle density expected in heavy ion collisions, and the request to obtain an optimal secondary vertex reconstruction, has led to prefer high granularity silicon detectors. They provide information about the position of the passage of particles through the detector with the ALICE ITS: this information is very accurate in the $r\phi$ plane, because of the higher granularity in this direction, while the resolution is lower in the z direction, due to the smaller intrinsic spatial resolution in this direction. The granularity decreases with the distance from the interaction point, because the particle densities decrease getting farther and farther away from that point.

In table 2.1 the main parameters of the ITS are given: radial position, length along beam axis, number of modules, spatial resolution, and material budget. The material budget reported in the table takes into account the average material including the sensors, electronics, cabling, support structures and cooling associated with radial paths through each layer.

Table 2.1: Characteristics of the six ITS layers, the beam-pipe and the thermal shields

Layer / Type	r [cm]	$\pm z$ [cm]	Number of modules	Intrinsic resolution [μm] $r\phi$	z	Material budget X/X_0 [%]
Beam pipe	2.94	-	-	-		0.22
1 / pixel	3.9	14.1	80	12	100	1.14
2 / pixel	7.6	14.1	160	12	100	1.14
Th. shield	11.5	-	-	-		0.65
3 / drift	15.0	22.2	84	35	25	1.13
4 / drift	23.9	29.7	176	35	25	1.26
Th. shield	31.0	-	-	-		0.65
5 / strip	38.0	43.1	748	20	830	0.83
6 / strip	43.0	48.9	950	20	830	0.83

2.2.1 Silicon Pixel Detector (SPD)

The two innermost layers of the ITS are made of hybrid Silicon Pixel Detectors (SPD). It plays a fundamental role in reconstructing the primary vertex and identifying the secondary vertices from the decays of heavy flavour particles: the precise spatial information, the small distance from the beam line and the small material budget are all relevant to obtain excellent tracking pointing resolution.

The ladder is the basic building block of the ALICE SPD. It consists of a two-dimensional sensor matrix of reverse-biased silicon diodes detectors, 200 μm thick, bump-bonded to 5 front-end chips, thinned down to 150 μm. The sensor matrix consists of silicon pixel detectors arranged in 256×160 cells. Each pixel cell measures 50 μm in the $r\phi$ direction and 425 μm in the

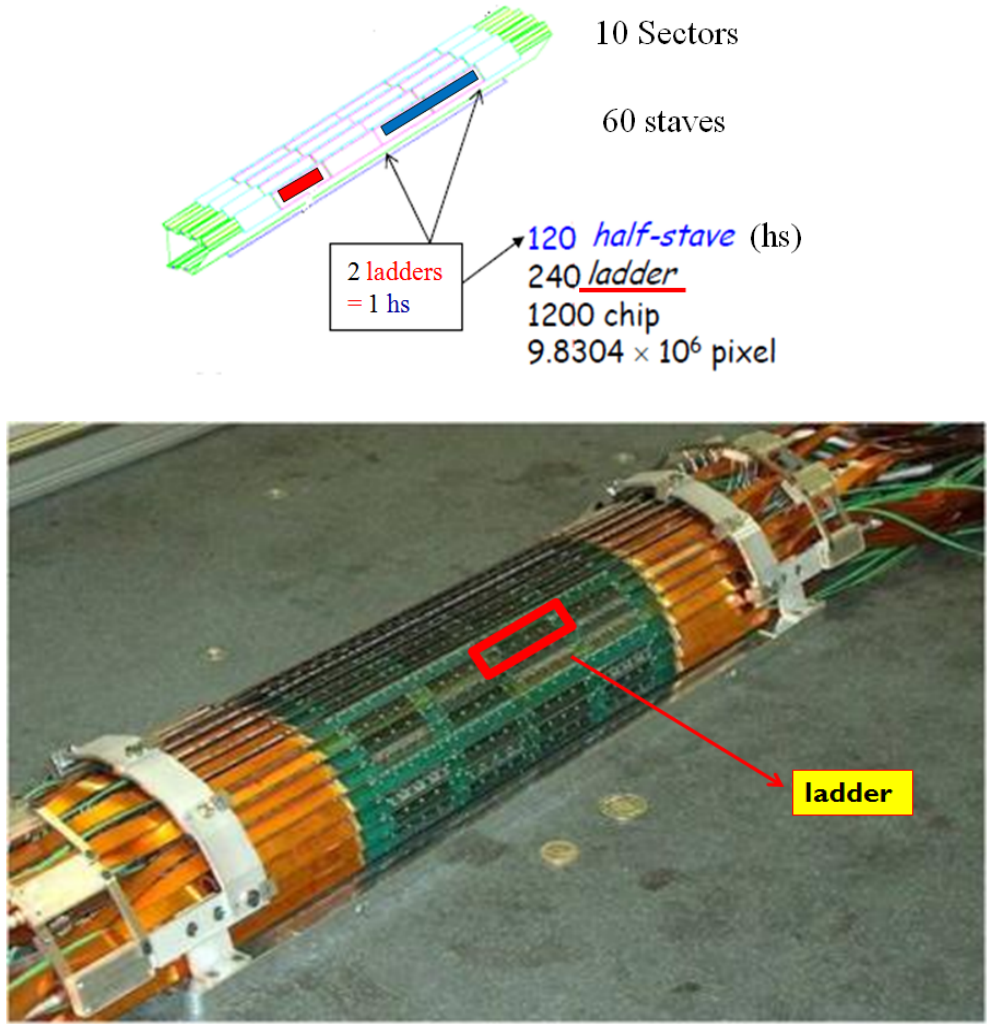

Figure 2.3: Schematic view of one sector in SPD. The ladder is shown in red, the half stave in blue, in the upper part of the figure. Two half staves form a stave. Each sector contains six staves: two in the first layer and four in the second layer. In total there are ten sectors mounted together around the beam pipe to form the SPD barrel. In the bottom part of the figure it is shown one of the two half barrels, prior of the installation.

z direction. The ladder measures 13.9 mm ($r\phi$)× 70.7 mm (z). Five front-end chips, each containing the electronics for the readout of a sub-matrix of 256 ($r\phi$)× 32 (z) detector cells, are bonded to the ladder. Four ladders are aligned in the z direction to form a stave. Six staves, two for the inner

layer and four for the outer layer, are mounted on a carbon fiber support and cooling sector. The staves of the inner (outer) SPD layer are located at an average distance of 3.9 cm (7.6 cm) from the beam axis. Ten sectors are mounted together around the beam pipe to form the barrel. The staves in each layer are mounted in such a way that there is a 2% overlap between the active regions in $r\phi$. Along z, instead, there is a gap between each two consecutive sensors. In total, there are 60 staves, 240 ladders and 9.8 M pixel cells arranged in 1200 read out chips, each containing 8192 pixel cells. In Figure 2.3 a schematic view of one SPD sector is shown in the upper part of the figure: the ladder is drawn in red; two ladders constitute one half stave (in blue). Each sector is constituted of two staves in the innermost layer, and four in the outermost layer.

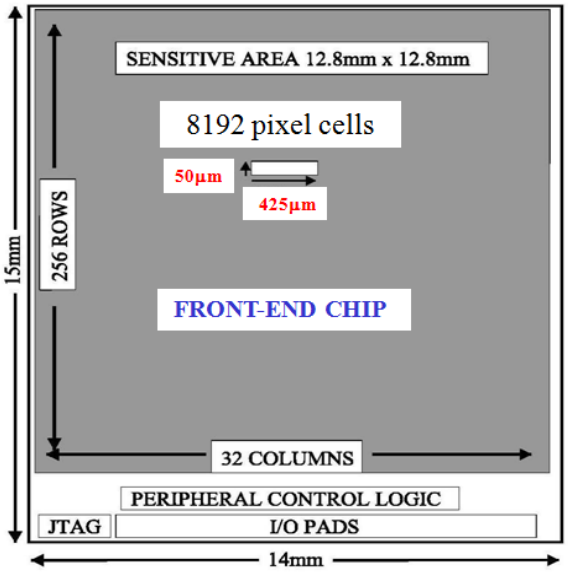

Figure 2.4: One electronic front-end chip of SPD layers.

In Figure 2.4 a sketch of a single chip is shown: the sensitive area of

the chip covers 12.8×12.8 mm^2 and it is composed of 256 rows ×32 columns of pixel cells.

The response type of the pixel is digital: this means that, when a particle hits the sensor, only the information about which pixel has been hit is available. The resolution of the SPD sensor is determined by the pixel cell size, the track incidence angle on the detector, and by the threshold applied in the readout electronics. The nominal resolution for an ideal digital detector would be $L/\sqrt{12}$, where L is the pixel dimension: 14 μm in the $r\phi$ direction and 130 μm in the z direction. However, it should be considered that, when a particle hits the single pixel near its edge, the neighboring pixel will also provide a signal, due to a phenomenon of charge diffusion. The two hits of the pixels above threshold are combined to form a cluster whose central position is closer to the position where the particle has passed through the detector. Instead, for tracks passing at the centre of the pixel, only that pixel is fired and again the position of the cluster is very close to the true track trajectory. This results in a better spatial precision: the values of the resolution along $r\phi$ and z extracted from beam tests [30, 31, 32] for perpendicular tracks are 12 μm and 100 μm, respectively.

The main difficulty in designing this type of sensors was to implement a front-end electronics that properly manage the signals around the chip. Each diode matrix is associated with a cell reading the chip using a technique called bump bonding. The bumps that realize the electrical and mechanical contact of the cells of the chip and pixel sensor are Sn–Pb spheres with a

diameter of 20 μm placed on the back of the sensor at each diode.

The SPD is also a trigger detector: each chip provides a fast trigger signal if at least one hit is detected. The trigger signals from 1200 chips are combined in a programmable logic unit which provides a level-0 trigger signal contribution for the ALICE data acquisition system, with the outcome signal which is shipped to the Central Trigger Processor (CTP) in $\sim$ 800 ns [33].

2.2.2 Silicon Drift Detector (SDD)

The two intermediate layers (layer 3 and layer 4) of the ITS are implemented with Silicon Drift Detector (SDD) technology.

The operating principle is based on the measurement of the time necessary for the electrons produced by ionization of the crossing particle to drift from the generation point to the collecting anodes, under the effect of an adequate electrostatic field.

The basic building block of the ALICE SDD is a module divided into two drift regions where electrons move in opposite directions under a drift field of $\sim$ 500 V/cm, as shown in Figure 2.5. The read out front-end electronics chips are on either side.

The SDD modules are mounted on linear structures called ladders. A picture of the SDD inner layer in which the ladders and the modules are in evidence, is shown in Figure 2.6.

There are 14 ladders with six modules each on the inner SDD layer,

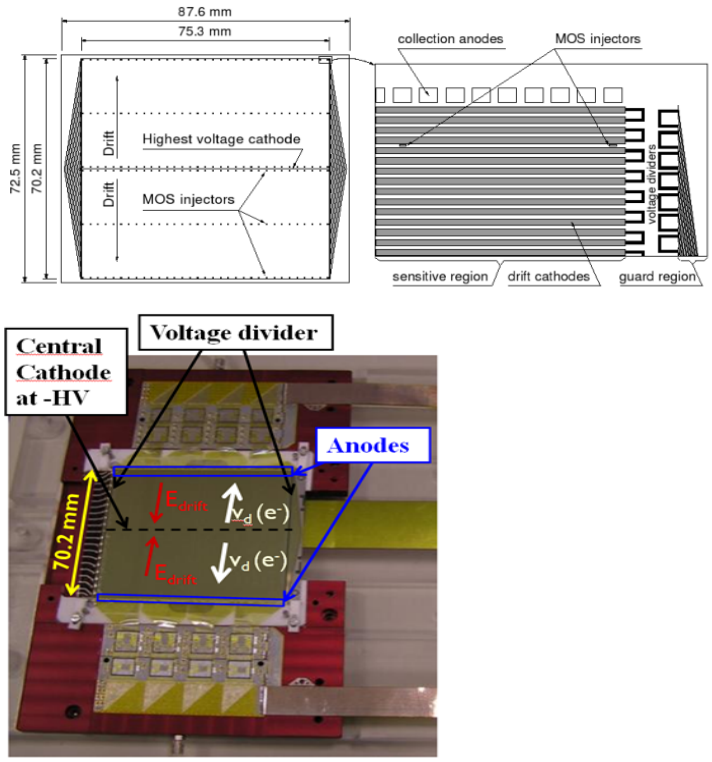

Figure 2.5: Schematic view of the SDD module. The sensitive area is split into two drift regions by the highest voltage cathode at the centre of the module.

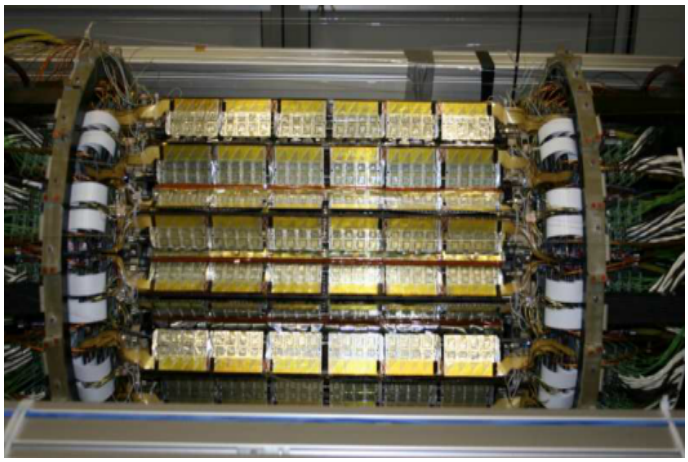

Figure 2.6: Picture of the SDD inner layer of the ALICE Inner Tracking System.

and 22 ladders with eight modules each on the outer SDD layer. Modules and ladders are assembled to have an overlap of the sensitive areas larger than

580 μm in both the $r\phi$ and z directions, so as to provide full angular coverage over the pseudo-rapidity range $|\eta|< 0.9$. The modules are attached to the ladder space frame, which is the layer support, and have their anode rows parallel to the ladder axis (z). The z coordinate is reconstructed from the centroid of the collected charge along the anodes. The electron drift time, from the point where the charge is generated to the anodes, provides the position along the other coordinate $r\phi$ on the detector plane. An optimal reconstruction of the $r\phi$ coordinate requires to know with good precision the drift velocity and the time-zero, which is the measured drift time for particles with zero drift distance. The drift velocity depends on temperature (as $T^{-2.4}$) and is therefore sensitive to temperature gradients in the SDD volume and to temperature variations with time. Hence, it is important to calibrate this parameter frequently during the data taking. The spatial resolution of the SDD detectors, as obtained during beam tests of full-size prototypes, is on average 35 μm along the drift direction (x_{loc}[1]) and 25 μm for the anode coordinate (z_{loc}).

The total collected charge is proportional to the energy loss by the crossing particle and can be used for particle identication.

The readout time of the drift detector is 1023 μs: it is the slowest readout time among the three types of silicon detector (SPD 296 μs; SSD 310 μs), and this is due to the time necessary to collect all the electrons drifting in the electrostatic field.

[1] In the local reference system the origin of the system is at the center of each module, the z axis is along the beam axis and x_{loc} is equivalent to the $r\phi$ coordinate.

2.2.3 Silicon Strip Detector (SSD)

The Silicon Strip Detector fills the last two layers of the ITS (layer 5 and layer 6). The SSD plays a crucial role in matching the tracks from the TPC to the ITS.

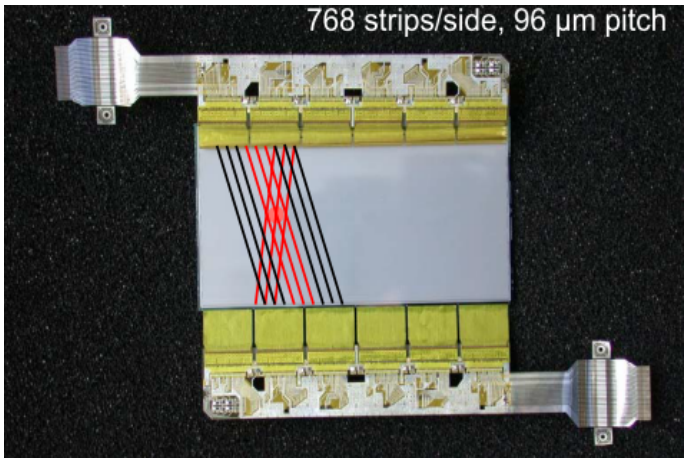

Figure 2.7: SSD module. The six front-end chips per side are visible.

The basic building block of the ALICE SSD is a module (see fig. 2.7) composed of one double-sided strip detector connected to the front-end electronics, with six chips per side, as shown in Fig. 2.7. Each sensor has 768 strips on each side, with a pitch of 95 μm. The stereo angle is 35 mrad, which is a compromise between stereographic view and reduction of ambiguities resulting from high particle densities. The strips are almost parallel to the beam axis, in order to provide the best resolution in the $r\phi$ direction, reaching an intrinsic point resolution of 20 μm in the $r\phi$ direction and 800 μm in the z direction.

A particle passing through the detector creates electron/hole pairs

that are collected by the strips in each side: the intersection point of the strips hit in the two directions provides the measurement of the hit position. The spatial resolution of the SSD system is determined by the pitch of the sensor readout strips and by the charge-sharing between those strips.

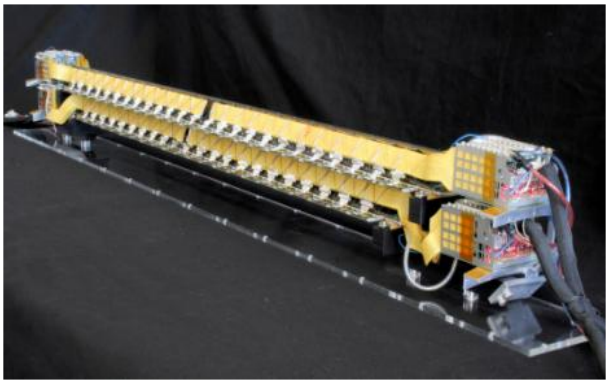

Figure 2.8: SSD ladder.

The analogue readout has a large dynamic range that allows to use the $\mathrm{d}E/\mathrm{d}x$ measurement for particle identication. The innermost SSD layer (layer 5) is composed of 34 ladders (Fig. 2.8), each of them being a linear array of 22 modules along the beam direction. Layer 6 (the outermost ITS layer) consists of 38 ladders, each made of 25 modules. In order to obtain full pseudorapidity coverage, the modules are mounted on the ladders with small overlaps between successive modules, that are staggered by 600 μm in the radial direction. The 72 ladders, carrying a total of 1698 modules, are mounted on support cones in two cylinders. Each module consists of a 1536 strip double-sided silicon sensor connected through aluminum-kapton microcables to the front-end electronics, for a total number of 2.6 million read-out channels.

2.3 ITS status in the first data taking years

The detector performance after two years of experience with LHC proton and Pb beams, as well as with cosmic rays, are discussed in this section, together with the status of each detector.

2.3.1 SPD status

The first pp run at $\sqrt{s}$=900 GeV have been exploited for the fine tuning of the SPD system. In the later runs, several aspects of the SPD are continuously monitored to control the behavior of the detector: noisy pixels (pixels that give signal even if no particle hit them), dead pixels (pixels that do not provide signal), noisy fast-or chips (chips that emit a fast-or signal even if there aren't hits in any pixel). If a noisy pixel appears during the data-taking, an on-line algorithm automatically identifies and excludes it from the data-analysis. The same procedure identifies dead pixels ($\sim 0.6\%$) and pixels with efficiency lower than 40% (~ 1.2 %). A big effort was carried on to identify the noisy and dead pixels. Both categories are excluded from the offline reconstruction [34].

A fraction of SPD modules cannot be stably operated due to localized reduced cooling performance ($\sim 30\%$). Several actions with the aim to recuperate the maximum number of modules have been considered, even assuming options that might require an intervention on the detector services. It has been decide to postpone any intervention after the end of the second

Pb run, hence in the beginning of 2012. The detector response has been found to be reasonably stable in time.

2.3.2 SDD status

At present, 39 modules out of 260 are kept out of data acquisition. The good modules in acquisition are $\sim 85\%$ of the total. The fraction of good channels in active modules is $\sim 99\%$. The main sources of excluded channels are half-ladders switched off due to electrical problems; few other modules are excluded from the acquisition due to either HV or DAQ problems. The modules in acquisition have good stability in time and only 1.5% of channels are excluded because being noisy or dead. During the normal operation, stand-alone calibration runs are performed at each beam fill to monitor the noise, bad channels, gains, drift velocity, and the time offset that has to be subtracted from the measured drift times to obtain the correct particle time, module by module. All monitored parameters are proven to be very stable over the entire data taking period [35].

2.3.3 SSD status

The stability of the system is monitored studying the time evolution of its calibration parameters (intrinsic noise, baseline, gain factor in the response of each single channel) and their correlation with the environmental conditions (e.g., the humidity). About 92% of the SSD modules are active: 141 modules out of 1698 were not operable due to electrical and configu-

ration problems or were masked because of noisy regions. There are about 98.5% of good channels in active modules, for an overall detector efficiency of about 90.3%. The good stability of the SSD allows to provide the expected performance in terms of space point resolution and $\mathrm{d}E/\mathrm{d}x$ measurements for particle identication [36].

2.4 ITS Performance in pp and Pb–Pb

The precise reconstruction of the particle trajectory (the track), the beam interaction point and the decay points of particles is of fundamental importance for the ALICE physics programme. The heavy flavour analyses require high precision in the identification of secondary tracks, coming from charm and beauty hadron decays, displaced from the primary vertex by few hundreds of μm (ex. $c\tau_{D0} = 124\,\mu$m). As already discuss in previous sections, the resolution on the impact parameter in the transverse plane, $d_0(r\phi)$, is the benchmark value to estimate the ITS capability in the reconstruction of primary and secondary vertexes.

To simulate the detector and the its performance, a detailed description of the whole experiment is done within the AliRoot framework [37] where the geometry of each detector and also of the supports and services, and the response of the detectors to the passage of the particles through the materials, are simulated in details. As it will be discussed in chapter 4, Monte Carlo simulation studies using this tool have been carried out before of data taking, to understand the detector's behavior and to estimate its

performances.

2.4.1 Alignment studies

The ITS is made of thousands of separate modules, whose position is different from the nominal one, due to the limitations associated with the assembly and integration of the different components, and due to mutual deformations between components. In order to achieve the required high tracking resolution and to estimate the real pointing resolution, that are determined by the intrinsic resolution of the modules, the relative position (location and orientation) of every module needs to be determined precisely based on an alignment procedure [38].

The first estimation of the misalignments has been performed using data collected in 2008 when cosmic-ray events and some events during the circulating LHC beams were recorded. Then, in 2010, a sample of pp data was collected without magnetic field in order to refine the alignment. Track-based alignment methods (Millepede [39] and an iterative local method) have been used to align the detector. The results of a preliminary survey performed for SDD and SSD are the input for the software alignment methods, based on global or local minimization of the residuals. These measurements have been taken during the assembly phase using a measuring device (laser-based) that determined the positions of the modules on the ladders and the positions of the ladder endpoints on the support cone. The alignment procedure consists in the residual minimization with track-based software alignment, as

the Millepede algorithm, which minimizes a global χ^2 of residuals (defined as the difference between the fitted track position on the detector plane and the position of the cluster) for all alignable volumes. In case of alignement with cosmics, the cosmic ray tracks are firstly reconstructed using the SPD and SSD. The SDD, which require a more elaborated calibration procedure due to the interplay between alignment, drift velocity and time-zero calibration, is added in a second step once a satisfactory alignment of the SPD and SSD is reached. The last step of the alignment procedure is the alignment of the whole ITS with respect to the TPC.

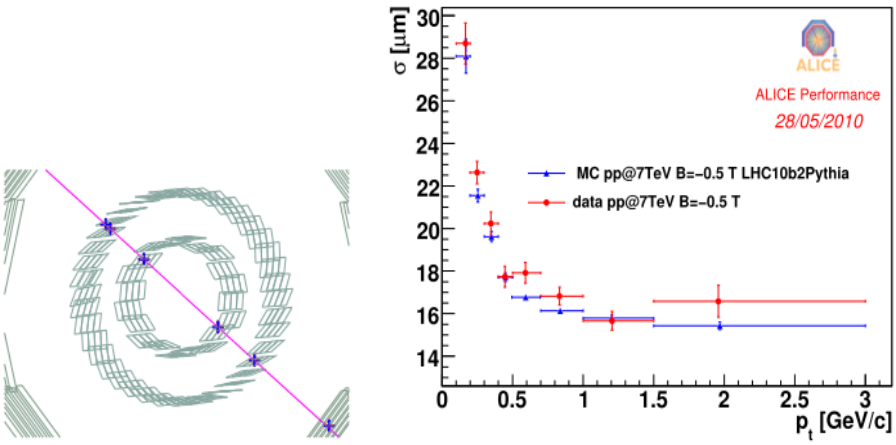

Figure 2.9: Left: cosmic event reconstructed in the SPD, as visualized in the ALICE event display: an extra point in one of the overlap regions of the outer layer is evident. Right: x_{loc} resolution as a function of p_T for the inner SPD layer, obtained with data from pp at $\sqrt{s} = 7$ TeV.

One important check of the quality of the alignment in the SPD modules is the spread in the residual of track to point for "extra" clusters, i.e. the clusters placed in the regions of overlap among modules, as the one illustrated in Figure 2.9 (left). The pairs of points produced by particles crossing the small acceptance of the overlaps between two neighboring modules allow

one to investigate the relative position of the modules themselves with high accuracy. The width of the distribution of the residual of the extra-cluster obtained from pp data as a function of p_T is shown for the x_{loc} coordinate in Figure 2.9 (right). The asymptotic component, which is dominant for p_T>1 GeV/c is due to the intrinsic resolution and to the residual misalignment; the curve rises at low p_T because of multiple scattering. Data points are compatible within errors with the results from a Monte Carlo simulation obtained using random Gaussian misalignments with rms equal to 7 μm: such value can then be considered as an estimate of the average level of residual misalignment for all the SPD modules.

2.4.2 ITS and TPC combined tracking algorithm

The tracking algorithm is based on the Kalman Filter procedure [40]. First, the reconstruction of the vertex is done using only information from the SPD hits (using tracklets, i.e. a pair of clusters in the inner and outer layers). The track reconstruction starts with the clusters on the external part of the TPC and proceeds towards the ITS. The seeds for the track candidates are created using the information from the external pad rows of the TPC and the position of the primary vertex, estimated with the SPD. After the 'candidate tracks' are found in the TPC, track reconstruction in the ITS (inward) is performed. A TPC reconstructed track is matched to a compatible cluster in the outermost ITS layer, then the track is followed in the ITS down to the innermost pixel layer. During the track finding

algorithm, in each step of the cluster association, a search window is opened to search for a cluster inside this window, compatible with the association to the track under construction. The search window is tuned according to the hit density, the track extrapolation length and the residual misalignment. The finding procedure terminates at the first layer of the SPD, then the track is back-propagated (outward) to the outermost layer of the ITS and then to the outermost radius of the TPC. Hence it is extrapolated to the TRD, to the TOF, to the HMPID, to the PHOS and to the EMCal and matched with hits on these detectors. Finally, the track is refitted inwards in TRD, TPC, ITS and it is propagated to the primary vertex. In the end, the vertex position is re-calculated using the reconstructed tracks, thus gaining in resolution with respect to the preliminary estimate obtained with tracklets.

All the clusters associated to the combined TPC and ITS tracks in the event under reconstruction are tagged, and the remaining clusters are used to find other tracks during the ITS stand-alone tracking procedure. Optionally, the ITS stand-alone tracker can be configured to consider all points in the ITS (also those already used by the ITS and TPC combined tracker), starting from the high p_T tracks, which are easier to reconstruct, to the low p_T tracks. The ITS stand-alone tracking will be explained in details in the chapter 4, where the tracking algorithm of the ITS Upgrade tool will be described. The aim of the stand-alone tracker is to extend the acceptance region down to p_T up to $\sim$ 100 MeV, finding tracks that do not reach the TPC due to their low p_T, and also to find tracks that pass through dead

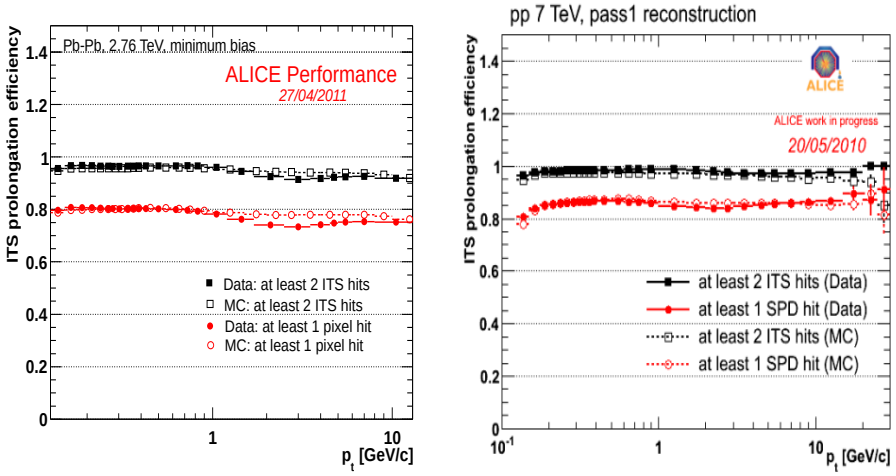

Figure 2.10: Track prolongation efficiency from TPC to ITS in Pb–Pb collisions (left) and pp collisions (right).

zones of the TPC or decaying between the ITS and the TPC.

The matching efficiency between tracks reconstructed in the ITS and those reconstructed in the TPC as a function of p_T is shown in Figure 2.10 for both pp and Pb–Pb collisions.

The comparison with a Monte Carlo simulation is also shown in the same figures: it is in agreement within $< 2\%$ with the efficiency observed in data in the range $0.2 < p_T < 10$ GeV/c. The matching efficiency is about 95% and it is quite constant in the entire momentum range for tracks reconstructed with at least two points in the ITS. It drops to 85% if a cluster in the SPD is request, and this is due to the modules which are switched off due to the cooling problems (∼30%).

The efficiency for the ITS stand-alone tracking can be evaluated by simulation: it is defined as the number of "good" refitted tracks (where a

good track is a track reconstructed with at least 3 associated clusters and without any associated clusters belonging to another track) divided by the number of "trackable" particles. A "trackable" particle is defined as a particle with at least three reconstructed clusters on three different ITS layers and with at least one of the reconstructed points in one of the three innermost layers in the case of the outward procedure, or in one of the three outer layers in the case of the inward procedure (see [41] and chapter 4 for further details). In Figure 2.11 the efficiency is shown as a function of p_T for Monte Carlo Pb–Pb central collisions: the blue circles show the ideal case of the ITS detector with all modules 100 % efficient while the red squares show the efficiency for the configuration of the detector during the 2010 Pb–Pb run ($\sim$ 30% of dead modules). A plateau is reached for values greater than 600 MeV/c. The drop of efficiency at low p_T is due to track curvature in magnetic field and the multiple scattering effect.

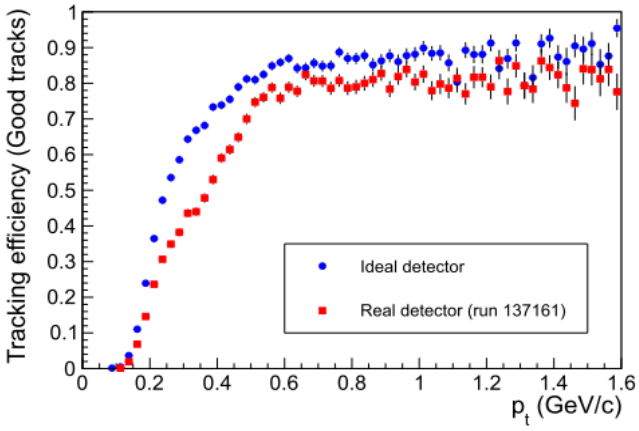

Figure 2.11: ITS stand-alone tracking efficiency in central Pb–Pb collisions as a function of p_T. The blue circles show the ideal case of the ITS detector with all modules 100 % efficient while the red squares refer to a typical configuration of the detector during the 2010 Pb–Pb run.

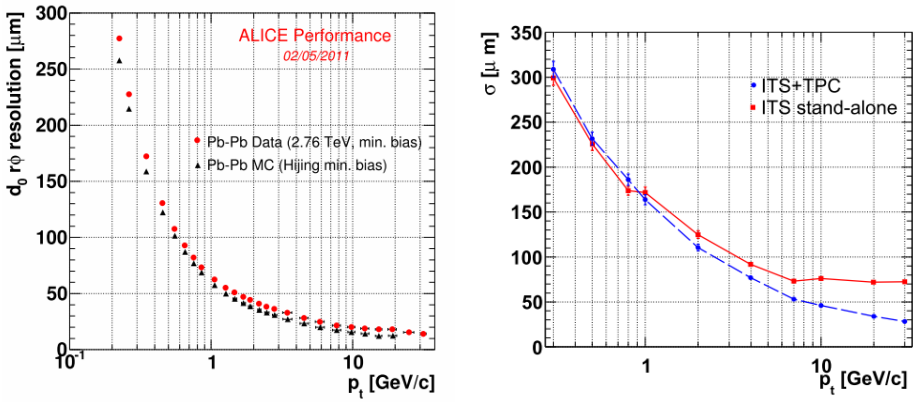

Figure 2.12: Impact parameter resolution of present ITS versus p_{t}, for the $r\phi$ (left, Pb-Pb data and MC) and z (right, pp MC simulation [41]) components.

In the left panel of figure 2.12, the impact parameter resolution in the bending plane ($r\phi$) for ITS stand-alone tracks is shown, for Pb–Pb data and Monte Carlo simulations with realistic residual misalignment. The plot shows a good matching between data and Monte Carlo. The impact parameter resolution for particle with momentum greater than 1 GeV/c is better than 65 μm. At lower p_T the main contribution to the impact parameter resolution is the material budget.

The impact parameter resolution in the longitudinal direction (z) which, differently than in the transverse plane, also benefits from the TPC information, is plotted in Figure 2.12 right, for the ITS stand-alone and ITS and TPC combined tracking.

In Figure 2.13 the impact parameter resolution for pions, protons and kaons as a function of p_T is shown, obtained with the ITS stand-alone tracks in Pb–Pb collisions at $\sqrt{s}$=2.76 TeV. The resolution is within specification for each particle species, and we observe a good agreement with the MC

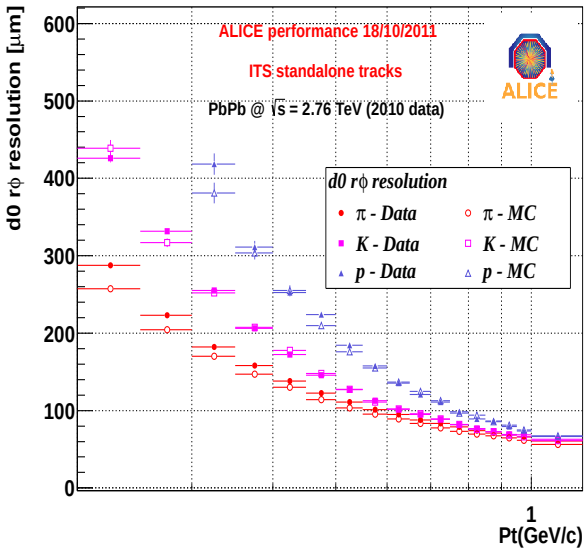

Figure 2.13: Impact parameter resolution of the ITS stand-alone tracks, versus p_{T}, for the $r\phi$ in Pb-Pb data at $\sqrt{s}$ =2.76 TeV for different particle species.

simulation.

In Figure 2.14 the relative p_T resolution is shown: in the left panel the p_T resolution is shown both for stand-alone tracks and those reconstructed with the ITS and TPC combined tracker, in a pp MC sample; in the right panel the resolution in Pb–Pb collisions performed with ITS and TPC combined tracking is shown. For ITS stand-alone tracks the resolution is worse by about one order of magnitude than the TPC and ITS combined ones, because the TPC has a larger lever arm, and also because the ITS has a limited number of points to measure a track.

The identification of low momentum particles by mean of the $\mathrm{d}E/\mathrm{d}x$ measurement in the non-relativistic region can also performed by the ITS. The $\mathrm{d}E/\mathrm{d}x$ measurement is based on the analogue information proportional

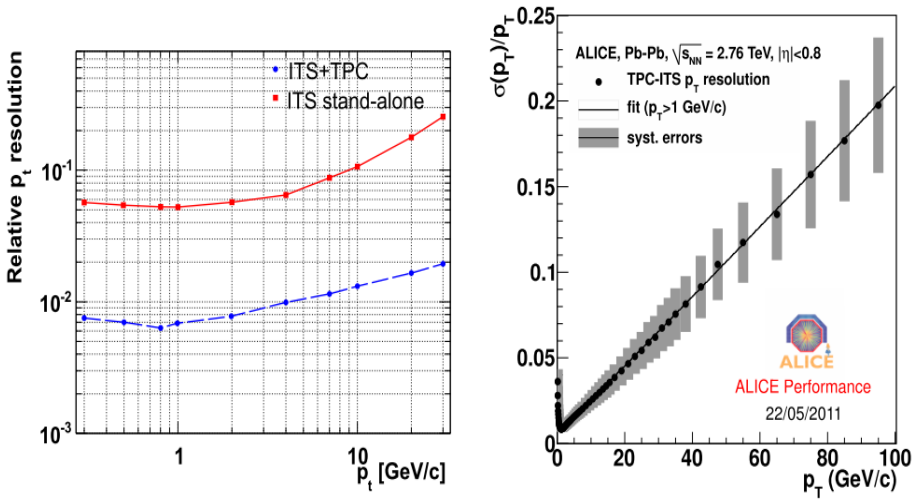

Figure 2.14: Left panel: ITS stand-alone relative p_T resolution in Monte Carlo pp simulation compared to ITS-TPC combined resolution in the p_T range $[0.3, 30]$ GeV/c [41]. Right panel: relative p_T resolution as a function of p_T for ITS-TPC combined tracks in an extended p_T range in Pb–Pb collisions.

to the charge collected by the four layers of SDD and SSD. Figure 2.15 shows the specific energy loss $\mathrm{d}E/\mathrm{d}x$ as a function of the momentum measured with the ITS stand-alone in Pb–Pb collisions. The three lines represents the pions, the kaons and the protons signals expected by the Bethe-Bloch formula. The ITS PID provides pions/kaons separation up to 0.5 GeV/c and pions/protons separation up to 1 GeV/c.

2.5 Detector efficiency

A study to evaluate the efficiency of each chip or module in every plane of the ITS has been performed during the first months of LHC operation in 2010. The aim of this work is to measure the efficiency of the different layers and their contribution to the tracking performance. The achieved results

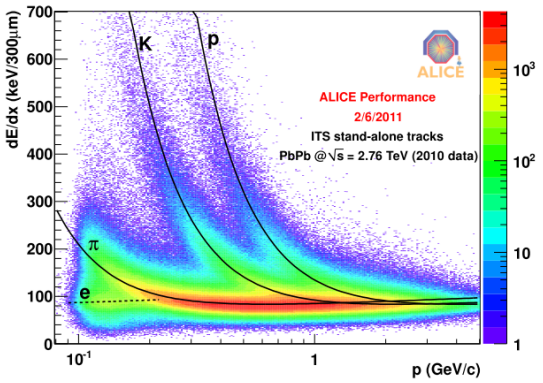

Figure 2.15: Specific energy loss $\mathrm{d}E/\mathrm{d}x$ as a function of the momentum measured with the ITS stand-alone in Pb–Pb collisions. The solid lines are a parametrization of the detector response based on the Bethe-Bloch formula.

were very important to have a good preliminary knowledge of the behavior of the 'real' detector and to have a first estimation of how realistic was the implementation and the description of the ITS in the Monte Carlo simulation, thus helping in the 'tuning' of the simulation. This is very important for the computation of corrections for acceptance and reconstruction inefficiencies and to an estimation of the systematics errors of the Monte Carlo tool.

The efficiency of a given layer can be evaluated by running the tracking algorithm without that layer, and counting the fraction of times a cluster is found to be associated with a track crossing the layer. A space point is searched in the whole reconstructed hit collection, to be compatible with the track prediction obtained without the layer under study, which is removed from the tracking algorithm: the interpolation of the track on this layer is used to evaluate in which chip (for pixel layers) or module (for the other

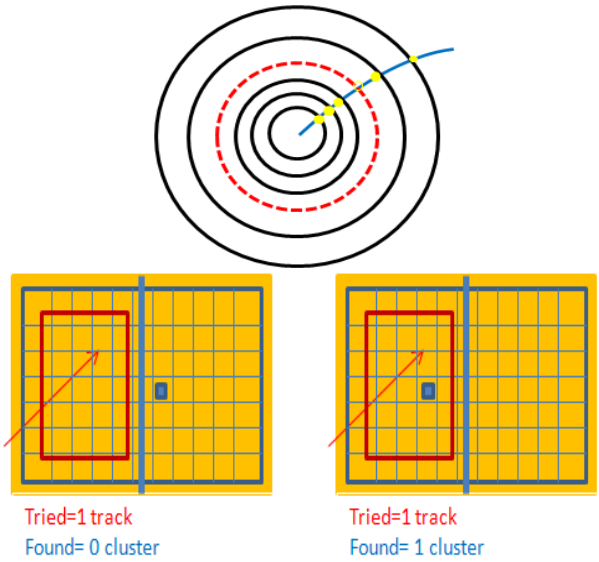

Figure 2.16: Schematic view of the procedure of the Plane Efficiency algorithm: a cluster compatible with the prediction of a track (yellow empty circle) is searched in the layer under study (in red). If the cluster is found, both the "tries" and "success" counters, which define the efficiency of a given module (see text), are incremented. If it is not, then only "tries" is implemented.

layers) the hit is expected.

The efficiency of each module is defined as the number of clusters 'found' divided to the number of tracks 'tried':

$$Efficiency = \frac{found}{tried}$$

and its error is

$$Err_{efficiency} = \frac{1}{tried}\sqrt{found(1 - \frac{found}{tried})}$$

In order to compute it, the following procedure is used: if a track (tried) passes through a module in the layer under study, a cluster is searched for in a fiducial acceptance window, and if the cluster is found, both the "tries" and "success" counters, which define the efficiency of a given module, are incre-

mented. If it is not, then only "tries" is incremented. This is schematically shown in the bottom part of the Figure (2.16).

The area of the fiducial window has been determined in order to avoid flow of counts from one module to the neighbouring ones, which would results in a smearing of the efficiency among adjacent modules, due to the uncertainty on the module assignment, when the track is closer to the border.

In case of SPD, the criterion used to establish the fiducial area also takes into account the fact that the dead pixels are concentrated at the corners of the chips. Getting away from the edge, the risk to meet dead pixels is reduced, as it can be seen in Figure 2.17. The width of the search window for the first pixel layer is such that the distance from the boundary is equal to 3 σ in x and in z direction (σ = track precision) and for the second pixel layer this distance is equal to 2 σ. The value of the sigma is obtained track by track, in the Kalman filter, in the same conditions used to evaluate the efficiency, i.e. by removing the layer under study of the tracking alghoritm.

The selection criteria for the tracks to be used in the plane efficiency evaluation have been tuned, in particular a selection of the good χ^2, in the differences between cluster position and the extrapolated track position; the minimum number of clusters to be associated to the track and eventually the minimum number of cluster in closest layers; the maximum number of

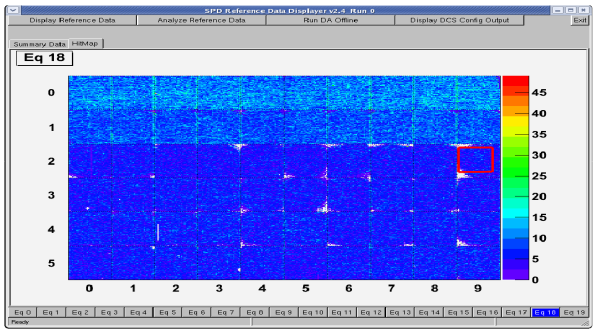

Figure 2.17: Example of a hit distribution chip per chip for sector 18: 10 chips constituting a half stave, for a total of six half stave constituting a sector (=equipment 18) are shown. The first two raw belong to the inner layer, in fact it can be noted a grater number of hits. Here the border effect, where dead pixels accumulate, is evident.

missing clusters in outermost layer or both in innermost and outermost with respect to the one under study and the requirement to have a cluster in the outer or inner layers with respect to the one under study. In table 2.2 the criteria selection are shown.

As a second example, the efficiency for all modules of each layer, for the run 120829 (25th May 2010, pp at 7 TeV), is shown in figures 2.18, 2.20, 2.21. The figures also shows the average efficiency for each layer, which has been computed by summing the number of 'tried' and 'success' in each module. The average efficiency for the first two layers is about 96%. This value can be smaller than the detection efficiency of not dead channels, due to secondaries and gamma conversions that are produced beyond the pixel layers (see sketch in figure 2.19): these charged tracks do not have a cluster associated to the plane under study because any charge was deposited there. The cuts have been optimized to reduce this contribution, but a Monte Carlo

Table 2.2: Selection criteria for good quality tracks for Plane Efficiency computation.

	Selection Criteria		
	Max n. of missing clusters	Max n. of missing outer clusters	Required clusters in outer layers
1 / pixel	2	2	True
2 / pixel	2	2	False
3 / drift	2	1	True
4 / drift	2	1	True
5 / strip	2	0	False
6 / strip	2	-	-

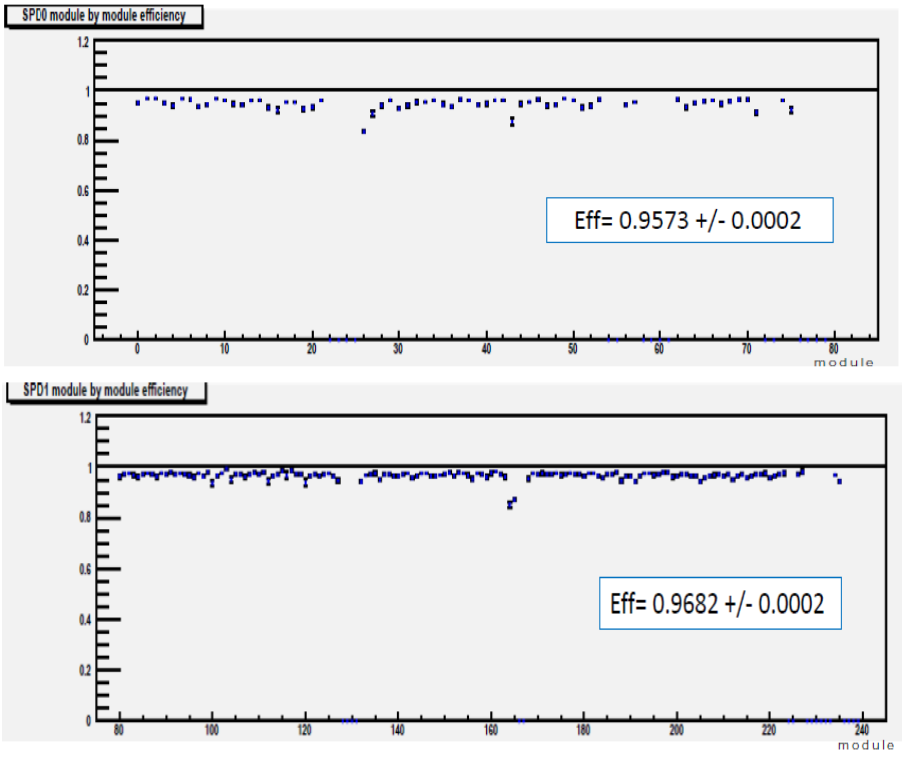

Figure 2.18: Total efficiency for the first and second layer of SPD.

study has shown that an irreducible component cannot be avoided.

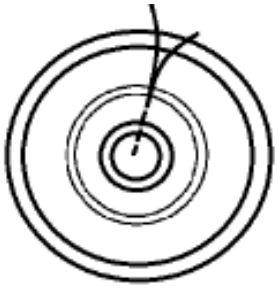

Figure 2.19: Gamma conversions which reduce the computed track efficiency for SPD layers.

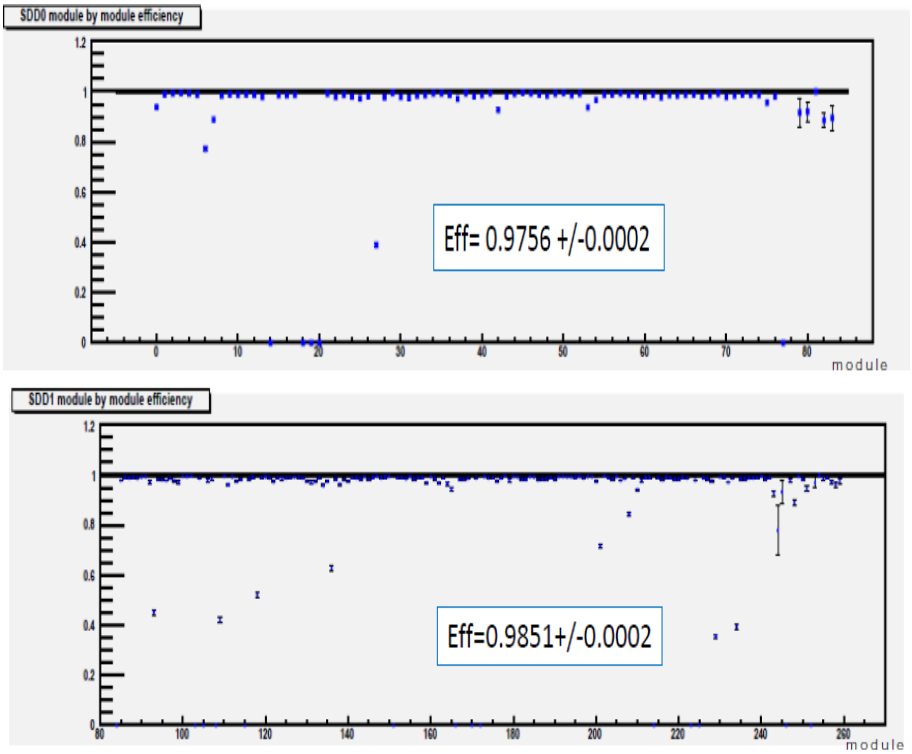

Figure 2.20: Total efficiency for the first and second layer of SDD.

In the figures below (2.22, 2.23, 2.24) the relative differences between the efficiencies obtained from data (pp collisions at 7 TeV) and MC are shown chip by chip, for the two SPD layers and for the second layer of SDD. The

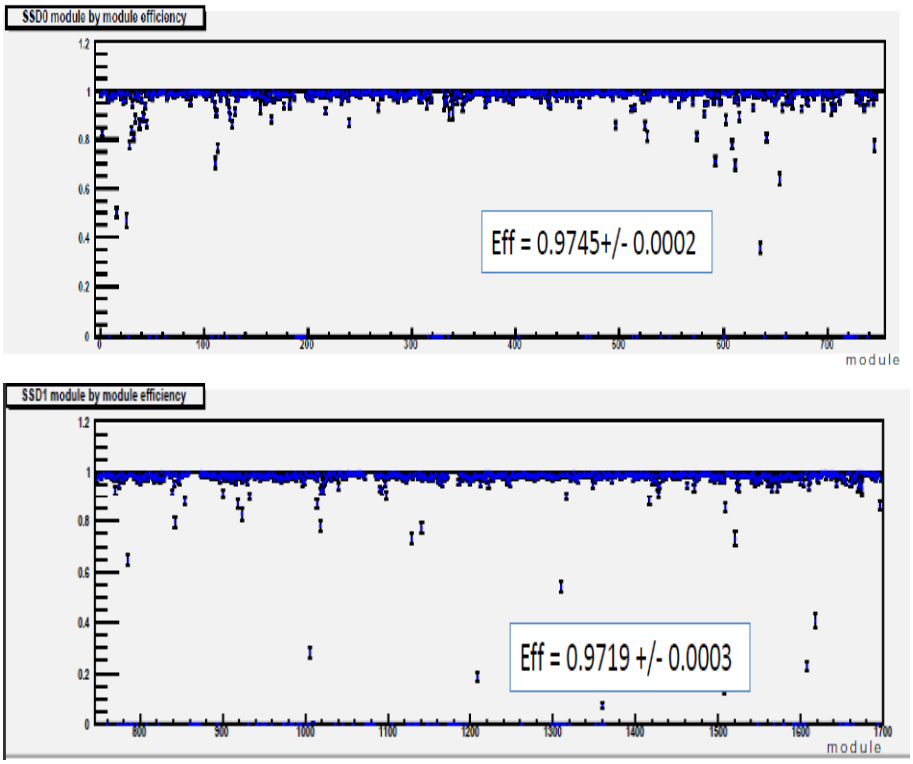

Figure 2.21: Total efficiency for the first and second layer of SSD.

corresponding histogram of the tracking precision in x direction for the first layer of SPD is shown in figure 2.25.

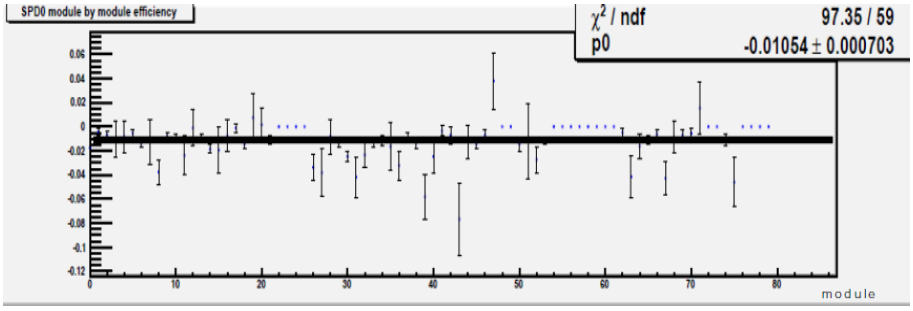

Figure 2.22: Relative efficiency (Data-MC)/MC in run 120829 for the first SPD layer: differences between Data and MC are within 1%.

The analysis of the differences between data and MC, chip by chip, or module by module depending on the subdetector, also was usefull in

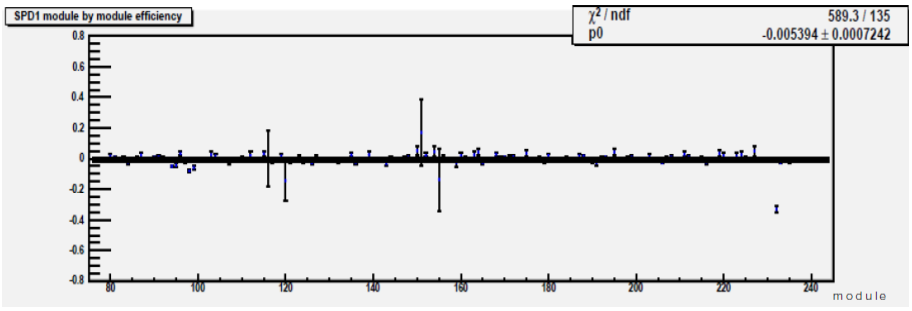

Figure 2.23: Relative efficiency (Data-MC)/MC in run 120829 for the second SPD layer: differences between Data and Mc are within 0.5%.

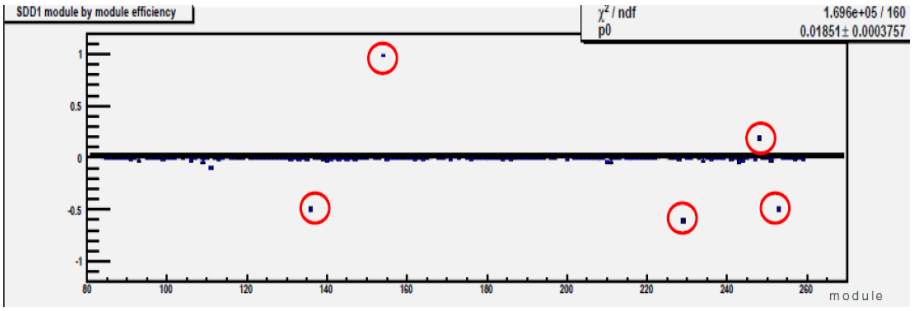

Figure 2.24: Relative efficiency (Data-MC)/MC in run 120829 for the second SDD layer. The red circles represent the module in which the configuration was wrong or not properly simulated in the MC.

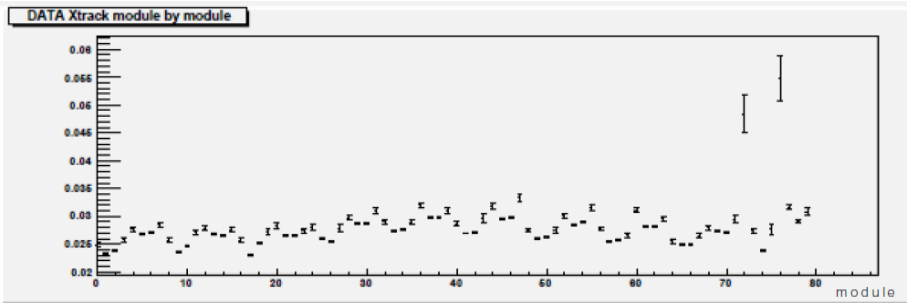

Figure 2.25: Tracking precision in X, module by module, of the first layer of SPD in run 120829.

understanding the real status of each detector, and in some cases it has helped in the detection of configuration issues of some modules and led to their re-calibration, as for instance in the case of modules with red circles in the second layer of SDD (figure 2.24).

In addition to the efficiency determination, these studies provided further information about the residual distribution (track prediction position - cluster position). In fact, with this algorithm the bias of having the cluster associated to the tracks, for a given layer under study, is removed. This is particularly important for the alignment studies, to accurately determine the cluster resolution (for tracking), and to examine the cluster shape distributions (which is shown in Figure 2.26)) and the differences between data and Monte Carlo, module by module, of the mean values of the residual distributions, see figure 2.27 and 2.28 for an example. All that has been very usefull to fine-tune the detector-response simulation models.

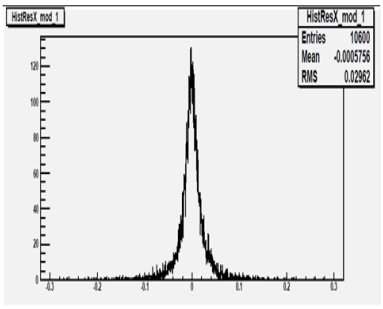

Figure 2.26: Residual distribution in module 1 (chip) of the first SPD layer.

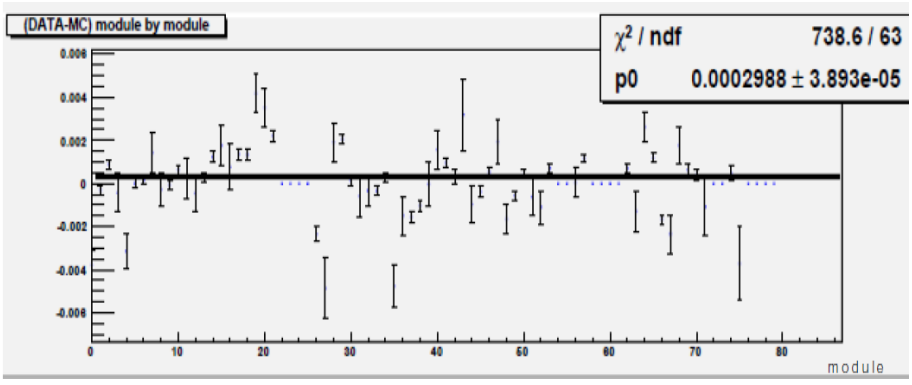

Figure 2.27: Differences of the mean values (module by module) of the residual distribution in X [(Data-MC)], for the first SPD layer. The mean difference is ~ 3 μm.

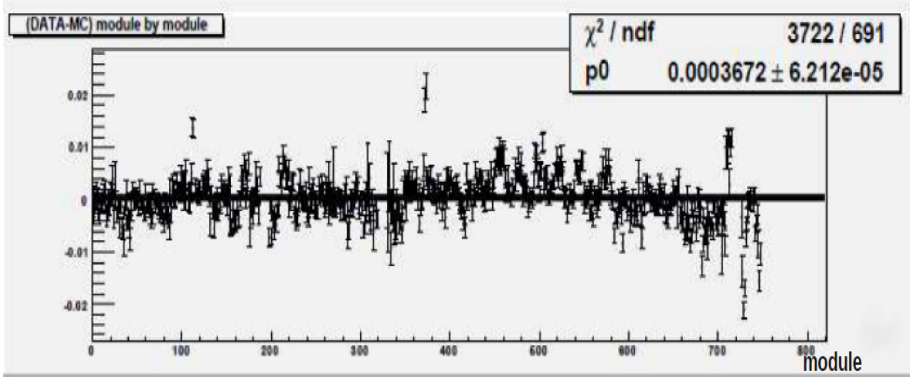

Figure 2.28: Differences of the mean values (module by module) of the residual distribution in X [(Data-MC)], for the first layer of SSD. The mean difference is $\sim$ 3.7 μm.

Furthermore, a detailed analysis of the tracking capabilities of the ITS, which is not discussed in this thesis, showed at the beginning, differences between tracking efficiency in data and MC, and these differences were in part explained with the results given by this 'plane efficiency' studies. Then, the resulting values of this study on the layer efficiency have been used to tune and correct the MC by adding sparse dead pixels in the MC description. Later on, when the luminosity of LHC increased, the individual dead pixel could be found by a simple counting algorithm. The procedure was still used to verify the nice agreement between data and MC. In table 2.3 the plane efficiencies for each layer of the ITS in two different runs are shown as example.

.

Table 2.3: Example of efficiency behavior in two runs of 2010: 115328 and 120829 pp at 7 TeV. The differences in percentage of the efficiencies between Data and MC are given.

	Efficiency (%) (DATA-MC)/MC	
	Run 115328	Run 120129
1 / pixel	-1	-1
2 / pixel	-0.9	0.5
3 / drift	-0.2	0.2
4 / drift	1.2	1.9
5 / strip	0.7	0.02
6 / strip	-3	-3

Chapter 3

ALICE physics performance in Pb–Pb and Motivation for an upgrade of the ITS

In this chapter, the ALICE performance in Pb–Pb collisions is summarized. A comparison with the performance of STAR, another general purpose heavy ion dedicated experiment at RHIC at BNL, is also performed. In the previous chapter, the fundamental role of the ITS in the reconstruction of secondary vertex of particle decaying within few hundred micron from the primary vertex, has been discussed. It has been shown that the precision of the present ITS in the determination of the track dca is adequate to study the production of charm mesons in exclusive decay channels (e.g. $D^0 \to K\pi$ and $D^+ \to K\pi\pi$) at values of transverse momentum above 2 GeV/c. At lower transverse momenta, however, the statistical significance of the measurement is limited. The situation is even worse for charm baryons, given that the most abundantly produced Λ_c has a mean proper decay length $c\tau$ of only 60 μm, that is about a factor 2 smaller than the D^0 meson one.

Therefore, with the present ITS charm baryons are not accessible in central Pb-Pb collisions. For the same reason, the study of beauty baryons or of hadrons with more than one heavy quark are also beyond the capability of the current detector. The motivations for an upgrade of the Inner Tracking System of ALICE are discussed in details in this chapter.

3.1 Physics goal of the ALICE experiment

LHC has some unique advantages and it is complementary to RHIC in several aspects. As discussed in chapter 1, significant differences in terms of energy density, lifetime and volume of matter created in the collisions are expected at the higher LHC centre of mass energy and, in addition, rare 'hard probes' (as, for example, the heavy flavours) are much more abundantly produced. After two years of LHC operation with proton and Pb beams, ALICE has proven its excellent capabilities to measure high energy nuclear collisions at the LHC. Initial performance on global event characterization (charged particle multiplicities, elliptic flow, volume and life-time inferred from pion HBT and high p_T suppression) are shown in the several papers published by the Collaboration [42]. They are rather different with respect the results shown by RHIC, but evolution and intrinsic properties are still well described by the theoretical models. In the following section a discussion of these items is mentioned.

3.1.1 Charged-Particle Multiplicity Density

The first step in characterizing the system produced in Pb–Pb collision at LHC energies is the measurement of the charged-particle pseudorapidity density, which is essential to estimate the initial energy density. ALICE performed this measure in Pb–Pb at 2.76 TeV/nucleon obtaining $\mathrm{d}N_{\mathrm{ch}}/\mathrm{d}\eta \sim 1600$. This value is different from the predicted calculation available during the design phase of ALICE in the early 90's ($\mathrm{d}N_{\mathrm{ch}}/\mathrm{d}\eta > 4000$); but it is in agreement with the extrapolation from RHIC measurements [43]. Normalizing per participant pair, one obtains $\mathrm{d}N_{\mathrm{ch}}/\mathrm{d}\eta)/(0.5{<}N_{part}{>}) \sim 8$.

In Fig 3.1 this value is compared to the measurements for Au–Au, Pb–Pb, pp and $p\overline{p}$ collisions over a wide range of collision energies [44].

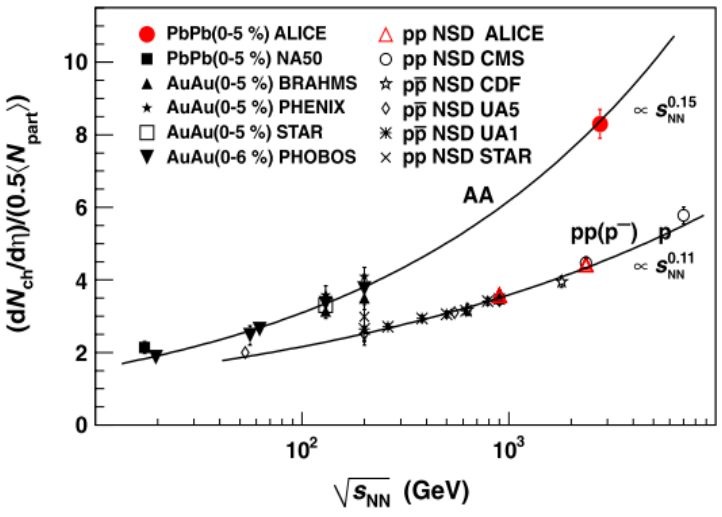

Figure 3.1: Charged-particle pseudorapidity density per participant pair for central nucleus-nucleus and non-single diffractive pp ($p\overline{p}$) collisions as a function of $\sqrt{s_{NN}}$[44].

The transverse energy is estimated by measuring the charged hadronic

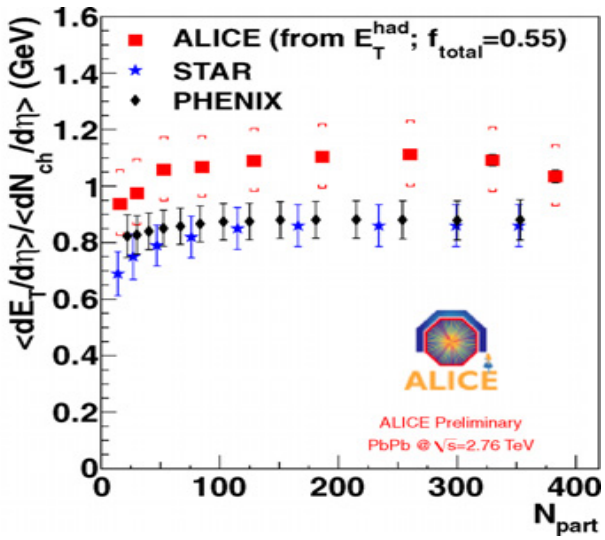

Figure 3.2: Ratio of transverse energy per participant pairs ($\mathrm{d}E_T$ /$\mathrm{d}\eta$) and $\mathrm{d}N_{\mathrm{ch}}/\mathrm{d}\eta$ as function of N_{part} for Pb–Pb collisions at 2.76 TeV and Au–Au collisions at 200 GeV[45].

energy with the tracking system corrected by the fraction of neutral particles not accessible by the tracking detectors. The total energy per charged particle is shown in figure 3.2 as a function of N_{part}. The centrality evolution looks similar for energy and multiplicity: both increase with energy and with centrality. This measurement can be used to extract the energy density using the Bjorken estimate eq.(1.4) For the most central collisions (0-5%), the value of $\mathrm{d}E_T/\mathrm{d}y$ provides an $\varepsilon\tau \sim 15$ GeV/(fm^2c) (where τ is the QGP formation time) at the LHC, about a factor 3 larger than the corresponding one at RHIC [46]. Assuming that the multiplicity is proportional to the entropy of the final state and $\varepsilon \propto T^4$, the factor 3 of increase in energy density from RHIC to LHC corresponds to a 30% of increase in the temperature of the QGP.

3.1.2 QGP: volume and life time

Other important global features of the medium are the freeze-out volume and the total lifetime of the system. They were measured in pp and Pb–Pb collisions by particle interferometry (HBT) [47].

Pion femtoscopy in Pb–Pb collisions can give a measure of the size of the homogeneity region from which the volume of the QGP can be inferred. Detailed femtoscopy studies in heavy-ion collisions, at SPS and RHIC, have shown that the sizes of the emission region ("HBT radii") decrease with increasing pair momentum, which is explained as a manifestation of the collective behavior of the system. The trend was predicted to persist at the LHC. Data from Pb–Pb collisions confirm the existence of a flowing medium and provide strict constraints on the dynamical models. Compared to top RHIC energy, the 'volume of homogeneity' increases by a factor two and the system lifetime increases by more than 30%, in line with the predictions (see Fig. 3.3 [47]).

3.2 Suppression of high p_T charged particle production

As mentioned in the first chapter, one of the key measurements in heavy-ion collisions at the LHC is the nuclear modification factor R_{AA} of charged hadrons. This measurement was one of the first indication from RHIC of the formation of the new state of matter with a clear clue of parton

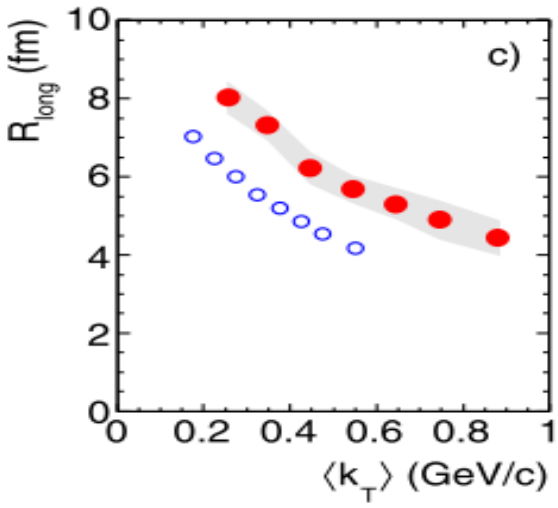

Figure 3.3: Pion HBT radii, along the beam direction, for the 5% most central Pb–Pb collisions at $\sqrt{s_{NN}} = 2.76$ TeV, as function of average p_T of the pion k_T (red filled dots). The shaded band represents the systematic errors. For comparison, the results for Au–Au collisions at $\sqrt{s_{NN}} = 200$ GeV are shown (blue open circles) [47].

energy loss in hot and dense QCD matter. At RHIC energies, the R_{AA} factor was measured to be about 0.2 and roughly independent of p_T in the range 5-15 GeV/c, corresponding to a factor 5 suppression in high p_T particle production with respect to pp collisions [43].

Figure 3.4 shows the nuclear modification factor R_{AA} of charged hadrons for central Pb–Pb collisions, compared to the same measurement performed by the PHENIX and STAR experiments at RHIC. In central collisions at LHC, R_{AA} exhibits a very strong suppression, reaching a minimum of $\sim$ 0.14 at p_T = 6-7 GeV/c. In this p_T region, the nuclear modification factor is smaller than at RHIC. This suggests an enhanced energy loss at LHC and therefore a more dense medium. A significant rise by about a factor two is observed in the range $7 < p_T < 20$ GeV/c. This pattern is very intriguing,

and at present there is not a unique theoretical interpretation.

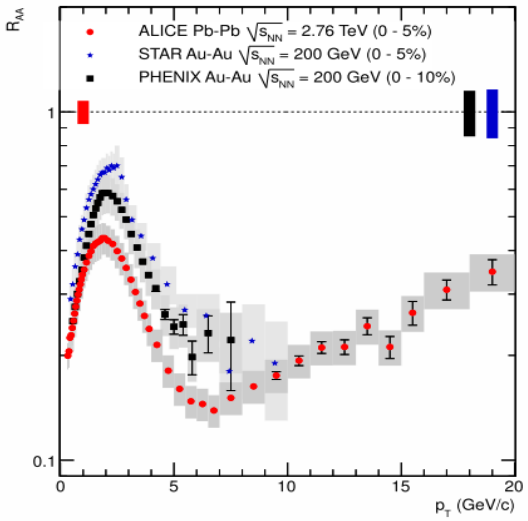

Figure 3.4: Nuclear modification factor R_{AA} for charged hadrons in central Pb-Pb collisions at the LHC, compared to measurements at $\sqrt{s_{NN}} = 200$ GeV by the PHENIX and STAR experiments.

3.3 In medium Energy Loss of charmed mesons

The measurement and comparison of R_{AA} of different medium probes provide a test of the colour-charge and mass dependence of parton energy loss. During the first run of Pb–Pb collisions at 2.76 TeV, ALICE performed the first measurement of the R_{AA} for the D meson, shown in figure 3.5 [48]. At the moment the analysis is restricted to $p_T > 2$ GeV/c. Presumably it will be possible to go down to $p_T \approx 1$ GeV/c, but reaching zero transverse momentum seems to be precluded with the current ALICE setup, due to the huge background.

This preliminary result imply a strong in-medium energy loss for c and b quarks. The R_{AA} of D^0 and D^+, measured for the first time as a function

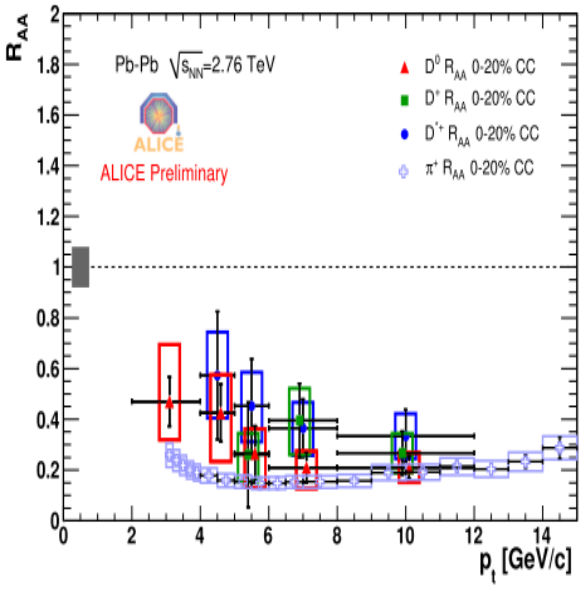

Figure 3.5: Heavy flavour nuclear modification factors R_{AA} for D mesons at mid-rapidity in central Pb-Pb collisions at the LHC measured by ALICE [48] compared to charged pions.

of p_T and centrality, is as low as 0.2-0.3 for $p_T >$ 5 GeV/c and compatible with the R_{AA} of pions. Below 5 GeV/c, there is a hint of a rise and one find that $R^D_{AA} > R^\pi_{AA}$. Higher statistics data, expected from the 2011 Pb–Pb run should allow to study this region more in detail.

The other key measurement concerns the beauty energy loss via R_{AA} with coverage down to low p_T. In ALICE, beauty production is accessed at mid-rapidity via $B \to e + X$. In the present ALICE setup, this will be presumably the only way to measure in addition to the forward rapidity measurement by muons. The left panel of figure 3.6 [48] shows the p_T-differential cross section of electrons from beauty decays in pp collisions at $\sqrt{s} = 7$ TeV. The cross section agrees well with the pQCD based calculations of the inclusive heavy-flavour decay electron from B hadrons for $p_T >$ 2-3 GeV/c [51].

At low p_T, the component of electrons from charm decays has to be subtracted statistically, implying a significant systematic uncertainty.

The single muon differential cross section as a function of p_T in pp collisions at $\sqrt{s} = 7$ TeV is shown in the right panel of figure 3.6 [48]. For $p_T > 5$–6 GeV/c, according to FONLL [51], the spectrum should be dominated by the beauty decays.

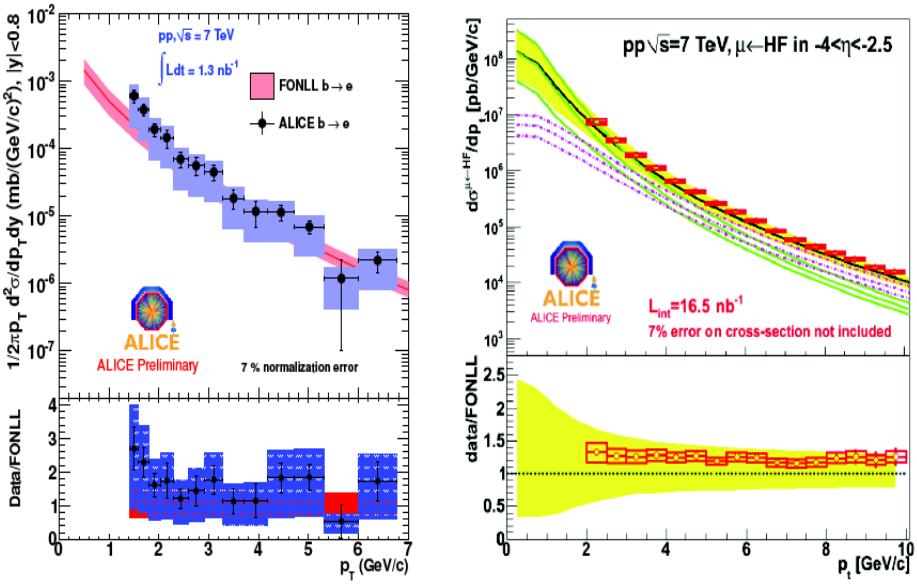

Figure 3.6: Leptons from heavy-flavour decay in pp at 7 TeV, measured by ALICE [48]. Left: electrons from beauty decays at mid-rapidity. Right: muons from heavy-flavour decays at forward rapidity.

The R_{AA} for the electron spectrum measured at mid-rapidity and the R_{CP} (central-to-peripheral nuclear modification factor) for the inclusive muon spectrum measured at forward rapidity are shown in figure 3.7 [48] (these electron and muon measurements are not fully background subtracted, however the p_T spectra are expected to be dominated by heavy flavour semi-

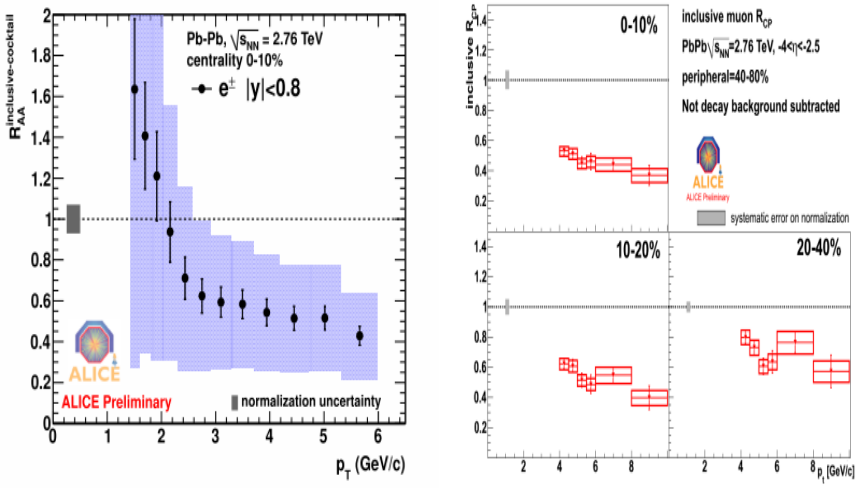

Figure 3.7: Heavy flavour nuclear modification factors in central Pb-Pb collisions at the LHC measured by ALICE [48]. Left: R_{AA} for the cocktail-subtracted electron spectrum, at mid-rapidity. Right: R_{CP} for the inclusive muon spectrum, at forward rapidity.

leptonic decays above 4–5 GeV/c). At high p_T, where beauty should dominate, the suppression is only a factor 2.5, that is smaller than what observed for D mesons (a factor about 4).

Summarizing, with the current detector, beauty production measurement at mid-rapidity may be possible only via single electrons. However, at low p_T the subtraction of the background contribution is problematic.

3.3.1 Baryon to Meson Ratio measurement

In the previous section, it has been shown that the spectra of individual particle species are modified in Pb–Pb with respect to pp collisions. Baryons and mesons show a different modification pattern due to the enhanced baryon production at intermediate p_T. The prediction of baryon enhancement to mesons ratio has been suggested as due to the coalescence, as discussed in

chapter 1.

Measurement performed by the STAR Collaboration (see, for example, [49, 50]) showed that the baryon/meson ratio reaches its maximum at $p_T \sim 2.5$ GeV/c and starts decreasing at higher momenta. The maximum value of the Λ/K^0 ratio in central collisions was found to exceed 1. The Λ/K^0 ratios measured by ALICE in Pb–Pb events at $\sqrt{s_{NN}}$= 2.76 TeV as a function of transverse momentum and for different collision centrality bins is shown in Figure 3.8, as well as in pp collisions at $\sqrt{s}$ = 0.9 and 7 TeV (left). The baryon/meson ratio in pp interactions always stays below 1 and is quite similar to what is observed in peripheral Pb–Pb collisions. As the collision centrality increases, the baryon/meson ratio develops a maximum at $p_T \sim 3$ GeV/c reaching a value of ∼1.5 for the 0-5% most central events. Comparing these preliminary ratios with those measured by the STAR Collaboration in Au–Au collisions at $\sqrt{s_{NN}}$ = 200 GeV, we note that, in the case of most central events, the baryon/meson ratio at the LHC decreases less rapidly with p_T than at RHIC (see Figure 3.8 (right)). The position (in p_T) of the Λ/K^0 maximum measured at Pb–Pb collisions at $\sqrt{s_{NN}}$ = 2.76 TeV is slightly shifted towards higher transverse momenta with respect to that observed in Au–Au events at $\sqrt{s_{NN}}$ = 200 GeV.

Coalescence models consider also the possibility of recombination of a heavy quark with di-quarks present in the QGP. It was suggested that this could lead to a rather significant enhancement of the Λ_c with respect to thermal models [52], where the relative abundance of particles depends only

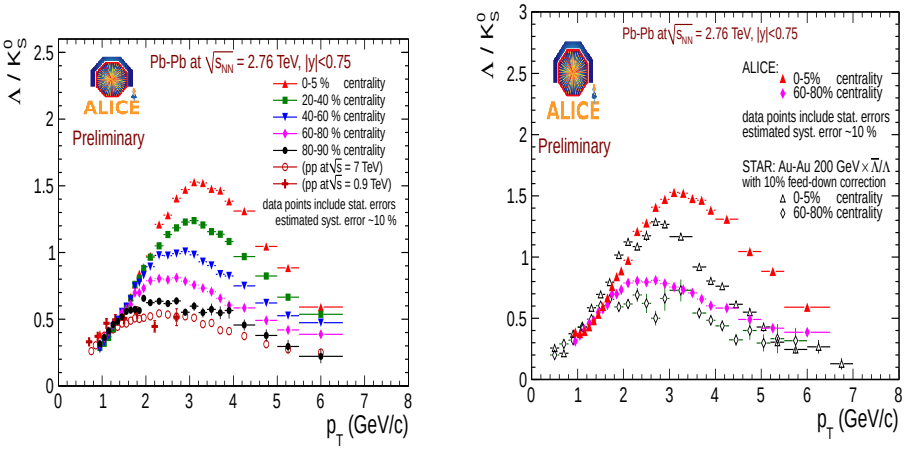

Figure 3.8: Left:Λ/K^0 ratios as a function of p_T for different centralities in Pb–Pb collisions at $\sqrt{s_{NN}}$=2.76 TeV, and also for minimum bias pp collisions at $\sqrt{s}$ = 0.9 and 7 TeV. Right: selected Λ/K^0 ratios shown on the left compared with those measured in Au–Au collisions at $\sqrt{s_{NN}}$ = 200 GeV

on their mass.

An enhanced production rate of multi-charm baryons would be a distinctive feature of thermalization of the medium produced in heavy ion collisions. The enhancement predicted by statistical models in case of hadronization by coalescence can reach a factor 10^3 for the Ω_{ccc} at LHC energies [23]. Thus, double and triple charmed baryons or charmed-beauty baryons could be observed (it should be noticed that states as the Ω_{ccc} have not been observed yet even in elementary collisions).

From the experimental point of view, the main issue for the measurement of charmed baryons is their rather short lifetime: for example, the $c\tau$ of the Λ_c is a factor of 2 smaller than that of the D^0. Therefore, the measurements of charmed baryons requires a very precise tracking and impact parameter resolution, because the decay tracks have typical displacements of

a few tens of micron ($\sim c\tau$) from the primary interaction vertex. Presently, the Λ_c signal was observed by ALICE in the $pK^-\pi^+$ decay channel in pp collisions at $\sqrt{s} = 7\ TeV$ collected in 2010, as it will be shown in chapter 5. However, the signal is observed only at transverse momenta above 3 GeV/c and the statistical significance is relatively low (about 5 σ), as compared to the D meson signals. In Pb–Pb collisions, in particular down to low transverse momenta, the Λ_c measurement seem to be beyond the present setup capabilities. Figure 2.13 in chapter 2, shows the impact parameter resolution as a function of p_T in pp and Pb–Pb collisions: to access the Λ_c, the impact parameter resolution should be better than a factor of 2 at least.

3.3.2 Elliptic Flow measurement

The most critical test of the "heavy ion standard model" comes from the measurement of the elliptic flow at LHC, the RHIC pillar which supports the 'fluid' interpretation of the QGP [43]. Assuming only small or no changes in the fluid properties between RHIC and LHC, the hydrodynamical model predicts firmly that the elliptic flow coefficient v_2, measured as a function of p_T, should not depend on beam energy [53] .

The ALICE measurement at 2.76 TeV [54] shows that the integrated elliptic flow of charged particles increases by about 30% compared to flow measured at the highest RHIC energy of 0.2 TeV (fig. 3.9), because the average p_T is significantly higher at LHC. This result indicates that the hot and dense matter created in these collisions at the LHC still behaves like a

fluid with almost zero friction [53].

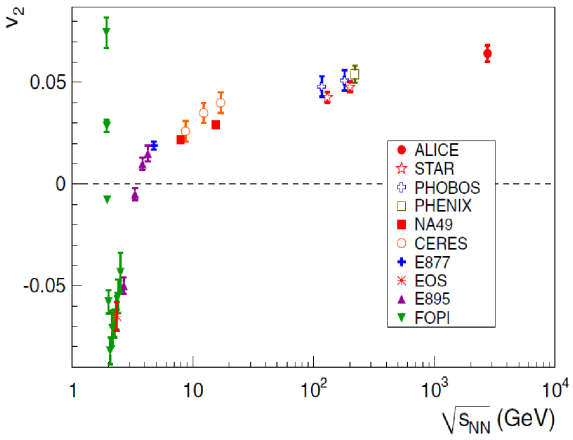

Figure 3.9: Integrated elliptic flow as a function of collision energy [54].

Elliptic flow as a function of transverse momentum p_T is sensitive to the evolution and freeze-out conditions of the created system. Figure 3.10 shows that the charged particle p_T-differential elliptic flow measurement[1], compared to RHIC, does not change within uncertainties at low p_T [54], which is remarkable because the beam energies differ by more than one order of magnitude. The 30% increase in the integrated flow, shown in figure 3.9, can therefore be explained to an increase in average transverse momentum.

In hydrodynamical model calculations, this increase in mean p_T is due to a larger transverse flow at higher energies. This leads to a more pronounced mass dependence of the elliptic flow. In figure 3.11, the identified particle p_T-differential elliptic flow compared to hydrodynamical model predictions is shown. For mid-central collisions the hydrodynamical model

[1]The elliptic flow estimated from two-particle correlations is denoted by $v_2(2)$, while those estimated from multi-particle correlations are denoted by $v_2(4)$ for the four-particle cumulant(see [54] and references therein).

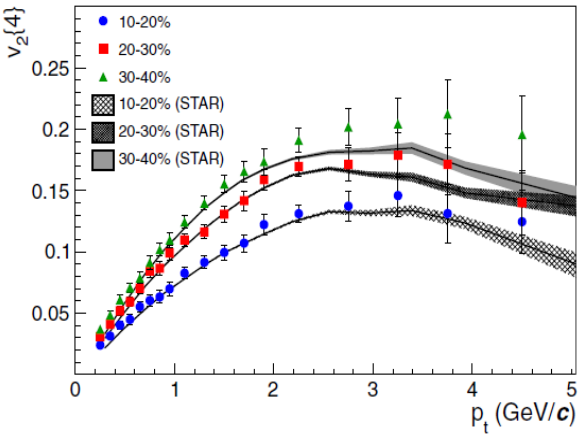

Figure 3.10: Elliptic flow for three centrality classes measured as a function of transverse momentum p_t. The bands indicate RHIC results measured by STAR [54].

predictions [53] (curves in figure 3.11 [58]) describe very well the measured v_2 for pions, kaons and antiprotons at low p_T (left panel). For more central collisions (right panel), the hydrodynamical model predictions well describe the flow of pions and kaons but not that of the antiprotons. This mismatch may indicate a larger radial flow in the data. At RHIC this was also observed and a better description of the antiproton flow was obtained by introducing a hadronic cascade "afterburner" in the calculations [55].

The hydrodynamical model predicts that the mass splitting pattern persists at large values of p_T in contrast to what is observed in data, as it can be seen in figure 3.11 above $p_T \sim 2$ GeV/c. An elegant explanation of the particle-type dependence and magnitude of v_2 at larger p_T is provided by the coalescence picture. At RHIC it was observed that v_2/n_q showed a universal scaling when plotted versus $(m_t - m)/n_q$ for relatively low $p_T < 2$ GeV/c [56]. Here n_q is the number of constituent quarks and $m_t = p_t^2 + m^2$ is the trans-

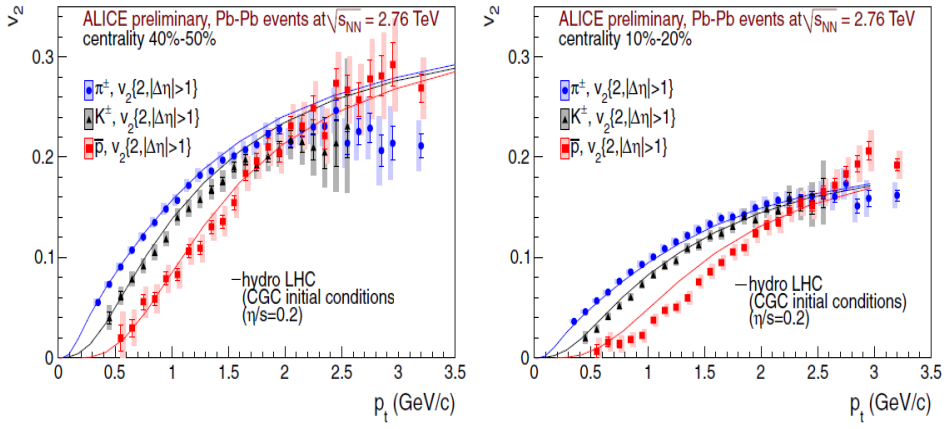

Figure 3.11: The p_T-differential elliptic flow for pions, kaons and antiprotons for 40-50% (left) and 10-20% (right) collision centrality. The curves are hydrodynamical model calculations. Figures taken from [58]

.

verse mass, with m the mass of the particle. At higher p_T, v_2 seems to scale with the constituent quark number, so that v_2/n_q scales with m_t/n_q. The same behavior is observed also at LHC, as shown in figure 3.12 [52], where the scaling at 2.76 TeV for 40-50% collision centrality measured by ALICE can be observed. This observation suggests the presence of a initial partonic state. Assuming the coalescence model [57] for hadronization, the flow of constituent quarks add up, so that $v_2^{Meson}(p_T) = 2\, v_2^q(p_T/2)$ and $v_2^{Baryon}(p_T) = 3\, v_2^q(p_T/3)$.

A very interesting test would be to verify if this universal scaling holds also for heavy flavour mesons and baryons. A first measurement of the D^0 elliptic flow coefficient v_2 in 30–50% central Pb–Pb collisions was obtained by ALICE (see figure 3.13) but with large uncertainties: if confirmed, the result would be very intriguing, because it seems to indicate that D mesons

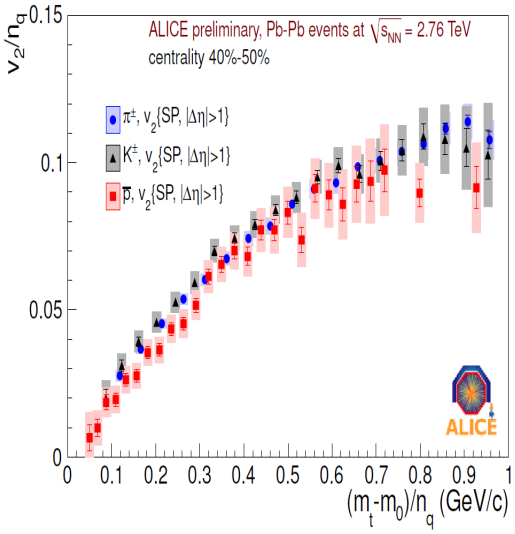

Figure 3.12: v_2=n_q vs m_t-m_0 for identified particles (pions, kaons and antiprotons) in Pb–Pb collisions at $\sqrt{s_{NN}}$ = 2.76 TeV measured by ALICE [52].

take part in the flow.

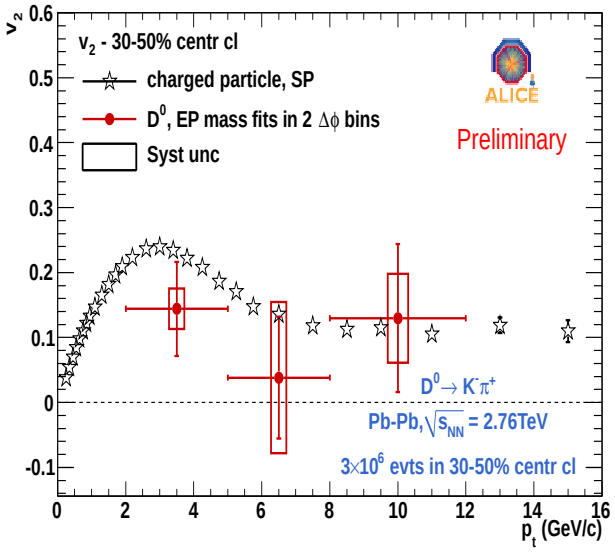

Figure 3.13: First measurement of D^0 v_2 in 30–50% Pb–Pb collisions at the LHC by ALICE.

3.4 Motivations for the upgrade of the Inner Tracking System

There are several frontiers for which the current experimental setup is not fully optimized, and where detector upgrades could enhance enormously the physics capabilities.

The Inner Tracking System was designed in the mid of the 90s using the available technology at that time. Progress in Si detector technology and a better integration closer to the interaction region with minimized material budget allow to improve the performance of the ITS. Detailed simulation studies, discussed in the next chapter, have shown that the resolution on the charged track dca can be improved by a factor of three assuming a substantial upgrade of the ITS. This improvement allows to increase the sensitivity to charm by one order of magnitude or more, depending on the transverse momentum range. A better signal-to-background ratio for fully reconstructed rare heavy-flavour hadrons can be achieved, including charm-strange and beauty-charm mesons, which should be exceedingly sensitive to parton re-combination effects. The study of the quark mass dependence of the in-medium energy loss would be achieved using fully reconstructed D and B mesons. In addition, low p_T and baryon coverage in the charm sector would allow to test collectivity of charm quarks. The possibility of equipping the upgraded ITS with triggering capabilities on displaced vertices, would open new fields for the study of heavy flavours in ALICE, by increasing statistics by more than an order of magnitude. In pp collisions, there is also a

need to improve the understanding of the flavour dependence of multiparticle production. The precise measurement of both the total charm and beauty production cross-sections, down to zero p_T, will be possible for the first time.

Moreover, an important limitation of the present ITS detector is given by the limited readout rate capability. The ITS can run up to a maximum of 1 kHz (with 100% dead time) irrespective of the detector occupancy. This rate restricts ALICE to record only a small fraction of the Pb–Pb collisions delivered by the LHC, whose design value is 8 kHz. The long term perspective for heavy ion physics at LHC is to further increase the luminosity leading up to a collision rate of 50 kHz.

In addition, the need for a new ITS derives from the intrinsic life-time of the present detector. The reduced performance of SPD, SDD and SSD, whose status is described in the previous chapter, can limit the measurements by reducing the statistical accuracy and increasing the systematical uncertainties due to the detection.

3.4.1 Impact of the ITS upgrade and new measurements

A new improved silicon tracker at mid-rapidity would dramatically improve or make accessible the following measurements in Pb–Pb collisions:

- charm down to zero p_T;
- beauty via displaced $J/\psi \rightarrow ee$;
- beauty via displaced $D^0 \rightarrow K\pi$;

- single displaced electron;
- beauty decay vertex reconstruction using any of the previous three channels plus an additional track;
- elliptic flow of charmed and beauty mesons and baryons down to low transverse momentum, including the baryon sector;
- charmed baryons, like Λ_c: since the production at LHC energies is still a rare process, a triggering scheme seems very attractive. It could be based on the topological selection of three charged tracks associated to a displaced vertex;
- beauty baryons, like Λ_b. Once the Λ_c can be experimentally tagged, then also the beauty baryon Λ_b could be measured via the decay chain $\Lambda_b \to \Lambda_c + X$;
- multiply-heavy-flavoured baryons like Ξ_{bc} and Ω_{ccc}: a possible approach could be based on the study of two or three displaced electrons produced in cascade semi-leptonic decays of the constituent heavy quarks.

3.5 Technologies for the upgrade

It will be shown in the next chapter that a dramatic improvement of the ITS capabilities can be achieved by adding a new layer closer to the beam line. The possibility to have such a new layout is due to the feasibility of the installation of a smaller radius beam pipe and to take full

advantage of the enormous progress made in the field of imaging sensors over the last ten years. The latter allows to conceive a new silicon tracker with greatly improved features in terms of determination of the distance of closest approach (dca) to the primary vertex, stand alone tracking efficiency, momentum measurement and readout rate capabilities.

- *Beam Pipe Design*:

  presently the central section of the beam pipe in ALICE is made of beryllium (Be); it has an outer diameter of 59.6 + 0.10 mm, a thickness of 0.8 mm and a length of 4820± 2 mm. The new beam pipe, still in Be, is assumed to have a reduced outer diameter of 39.6 mm. A wall thickness of 500 μm, instead of 800 μm is also being considered.

The concept of the upgraded ITS includes an innermost layer at a smaller radius with respect to the present one and a combination of pixel and strips layers. The silicon strip technology is well consolidated and the improvement under study are mainly on the layout and the front-end electronics functionalities. For the silicon pixel layers, two options are being investigated: hybrid pixels and monolithic pixels.

- *Hybrid Silicon Detectors*: in the hybrid pixel detector concept the sensor and the front-end electronics are implemented on two separate silicon substrates, as schematically shown in the left panel of Figure 3.14. Hybrid detectors represent the state-of-the-art of all pixel detectors for the current LHC experiments. In the hybrid approach the front-end

chip and the sensor are produced on two different wafers and then connected using the bump bonding technology. Present bump bonding techniques are limited to pitches of 30-50 μm. However, the recently introduced Cu-pillar technology may reduce substantially this limit in the near future. Currently, bump bonding represents one of the main cost factors for the production of hybrid pixel detectors and prevents their application to larger surfaces. The main advantage of hybrid pixels is that the sensor and the front-end functionality can be separately optimized.

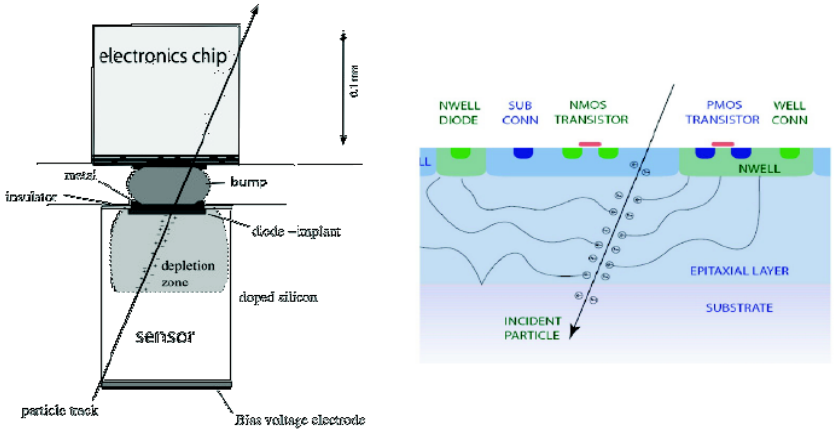

Figure 3.14: Schematic view of a hybrid (left) and a monolithic (right) pixel detector, taken from [60, 61]

- *Monolithic Silicon Detector*: in monolithic approach the sensor is incorporated inside the ASIC chip. Monolithic pixel detectors use as the detection volume the p-type epitaxial layer grown on the highly p-doped silicon substrate during standard CMOS microelectronic processes. The epitaxial layer typically has a thickness of 10-18 μm, thus

the most probable signal generated by a MIP is of the order of 10^3 electrons assuming an average production of 80 e-h pairs μm. In the standard monolithic sensor the epitaxial volume is un-depleted and the charge generated by a ionizing particle is collected mainly by thermal diffusion. CMOS pixel sensors typically feature pixel dimensions of 20×20 μm^2. Additionally, they allow integrating the complex signal processing circuitry on the same substrate as the sensitive volume. Therefore they offer a significant reduction in cost since only CMOS wafers are used. At the moment, the main limitations of monolithic pixel detectors are the radiation hardness, the readout speed and the signal to noise ratio for particle identification.

All the different technical implementations described above will allow to achieve the spatial resolution required for the ALICE ITS upgrade. A key requirement that needs detailed discussions is the material budget limitation for the innermost layers, which should be contained to 0.3-0.5%X_0. Monolithic detectors will have a reduced silicon contribution with respect to hybrids, although an intensive R&D is carried out the thinning of the hybrid pixel detector. In particular, for hybrid pixels a sensor thicknesses of 100 μm has already been achieved and tests are currently ongoing to reduce the front-end chip thickness to 50 μm. A sizable contribution to the overall material budget will in both cases originate from the support, cooling and interconnection. The material budget is one of the most critical parameters for the innermost layers, because it plays a key role for the ultimate limit of

the achievable pointing resolution.

- *New Strip Detector*: new strip detector will benefit from past experience, leading to better reliability and uniformity of several components and thus to a significantly improved overall performance in real operating conditions. In addition, appropriate modifications made on each component design will allow to meet the requirements for the new physics aims, the expected experimental conditions and the position of the detector in the new tracker. At smaller radii with respect to the present position, the strip detector will probably face an occupancy problem that requires to redefine its layout. The upgraded strip detector will be based on 300 μm thick, double-sided micro-strip sensors with a small stereo angle between the strips on opposite sides, in order to keep an acceptable rate of ambiguities in track reconstruction. Given the prospect of a smaller distance between the strip layers and the interaction vertex and taking into account the increased particle multiplicity foreseen at the nominal LHC energy, a redesign of the current sensor is being developed to allow a reduction of the cell size in order to keep low the occupancy.

3.6 Upgrade Timeline

The ALICE ITS upgrade will require a long shutdown (LS) and, therefore, will naturally have to be in phase with the installation of upgrades

for the other LHC experiments, planned as of today for the 2013/14 and 2017/2018 shutdowns. The ITS upgrade targets the long LHC shutdown period in 2017/2018 (LS2). The scope of the upgrade for the LS2 will be well tailored to what can be reasonably prepared and tested within the next five years and installed in 12-15 months, with safety margin. Decisions on upgrade plans in terms of physics strategy and detector feasibility should be taken by March 2012. The R&D efforts will continue till 2014, construction will take place in 2015/16, installation and commissioning in 2017/18.

Chapter 4

Simulation studies for an upgrade of the Inner Tracking System

4.1 Introduction

In this chapter the functional requirements that an upgraded ITS detector should satisfy in order to obtain the physics performance which has been discussed in the previous chapter, are presented.

The tracking performance has been studied by means of a Monte Carlo description based on transport code. The main requirement of such tool is the possibility to easily vary parameters such as the number of layers, their radii, the thickness of the sensitive detector, the material budget in each layer and the spatial resolutions of each sensor, so that the optimization procedure can be carried out in a flexible way.

This MC tool has been used to obtain a better description for a few

given detector configurations, because it is intrinsically slow in term of CPU time, but its fundamental contribution is obligatory to provide the closer description of the details of the simulation. Once the best layout will be chosen, the MC tool (ITSUpgrade in the following) will be tuned to accommodate its properties.

The tool has been validated against the current ITS performance (with the current ITS design) using both pp and Pb–Pb MC samples. After the validation of the tool, the following two new configurations have been considered and their performance have been compared: i) an ITS where only the present SPD detector is upgraded ("SPDNew") and ii) a totally new ITS detector ("AllNew").

4.2 Simulation conditions

Beam pipe: The ALICE request for the upgrade is to get a new beam pipe with a wall thickness of 0.5 mm and an outer diameter of 39.6 mm, see previous cahpter for details.

Particle load: the charged particle density in central Pb–Pb collisions at top LHC energy determines the density of particles on the different detector layers and, consequently, the occupancy per layer and in the individual channels. A relevant contribution to the hit density on a given layer can come from secondary particles which are mostly produced in the interaction of other particles with the material of the beam pipe and of the inner layers.

By extrapolating the measured charged particles in central Pb–Pb collisions at $\sqrt{s_{NN}} = 2.76$ TeV using the $s_{NN}^{0.15}$ scaling [44], one obtains $\mathrm{d}N_{\mathrm{ch}}/\mathrm{d}\eta \simeq 1970$ for central Pb–Pb collisions at $\sqrt{s_{NN}} = 5.5$ TeV. Based on a Monte Carlo simulation for central Pb–Pb collisions, which uses the HIJING generator tuned on such charged particle multiplicity, the hit density due to all charged particles, both primaries and secondaries, has been estimated.

Detector acceptance: this study focuses on the central rapidity region and therefore the detector has been assumed to have a barrel geometry. The ITS acceptance has been determined based on its matching with the current external barrel detectors. The acceptance for tracks emitted from the nominal Interaction Point (IP) in the Pb–Pb interaction at $\sqrt{s_{NN}} = 5.5$ TeV has to take into account the luminous region that would spread around the nominal IP with a longitudinal Gaussian distribution with $\sigma_z^{\mathrm{lumi}} = 5.61$ cm [62]. The requirement of accepting all tracks within a given η range from this luminous region determines the longitudinal length of each ITS layer. In the following sections, we assume for the acceptance of the upgraded ITS the condition corresponding to 90% of the luminous region and a pseudo-rapidity coverage of $|\eta| < 1.22$.

Number and radius of layers: the optimization of the detector parameters has been studied by considering primarily the stand-alone performance and monitoring that the efficiency of the track matching from the TPC to the ITS stays at an excellent level in the ITS-TPC combined tracking mode. The performance will be studied considering a 7-layer layout, with two different

configurations.

Material budget: a reduction of material budget can be achieved by reducing the thickness of the sensor and of the electronics, and the material budget of the services (mechanical support, cooling system, read-out system). Based on the most recent developments of the pixel technologies, which has been mentioned in the previous chapter, here the effect of the material budget of the first layer on the pointing resolution, varying X/X_0 between 0.3 and 0.9 and assuming for the remaining layers the same material budget as in the current ITS, will be shown.

Detector segmentation: the segmentation of the detector determines the intrinsic spatial resolution of the reconstructed track points. A small segmentation of the detector is also important to keep the occupancy at a low value. An excellent resolution of the first layer is fundamental for the resolution on the impact parameter at high p_T where the effect of the multiple scattering becomes negligible. For the outer layers, a good resolution is also important to improve the p_T resolution and the tracking efficiency in the ITS stand-alone mode. In our studies we have assumed an intrinsic spatial resolution of 4 μm both in $r\phi$ and z.

4.3 Simulation Tool

The software to simulate the new detector has been developed in the standard Aliroot framework [37]. This software will replace that of the actual

ITS by simply setting an option in the Config.C. The former is a configuration file needed to set up the whole simulation. It is a C++ macro that is processed before the simulation starts, it creates and configures the Monte Carlo environment: the particle generator object, the magnetic field map and the detector modules.

With this simple switch from the current ITS to the Upgrade in the AliRoot Framework, one can use the analysis tools available to make performance studies (e.g. $D^0 \to Kp$, $\Lambda_c \to pK\pi$), from the simulation of the geometry, the response of the detector to the passage of the particle, the reconstruction of the tracks and the analysis of the reconstructed tracks, as it is done in the current analysis procedure. In Figure 4.1 the sketch of the different steps of the analysis in AliRoot is represented, beginning with the switch from the current to the upgraded ITS: the difference is in the description of the ITS module; the analysis then follow the same procedures as the current one, with the construction of the Event Summary Data (ESD: data are stored in containers filled with reconstruction tracks, information on the vertex positions, etc.. event by event) and the Analysis Object Data (AOD: containers of the tracks with all the information necessary to the different analysis topics).

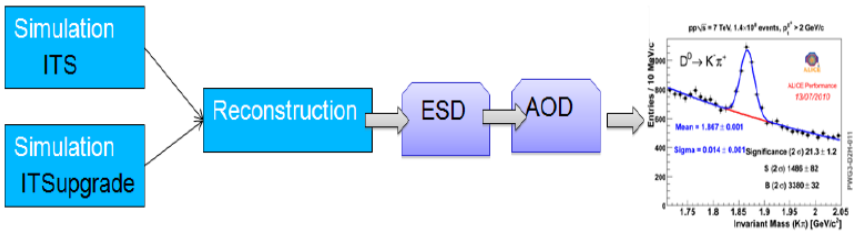

Figure 4.1: Schematic diagram illustrating the simulations and the reconstruction procedure for MC study of the ITS Upgrade and the current ITS

4.3.1 The simulation framework: ROOT, GEANT3 and AliROOT

Here a brief description of the main ingredients of the simulation in AliROOT is given, from geometry to the detector response format. AliRoot is based on the ROOT framework, that provides an environment for the development of software packages for event generation, detector simulation, event reconstruction, data acquisition and a complete data analysis framework. The geometry package developed within AliRoot describes the ALICE detectors in great detail, including services, the vacuum pumps and beam pipe. It uses the GEANT3 [63] package which takes over the simulation of primary collisions, and takes care of the transport of the particles emerging from the interaction of the beams in the material of the detectors, simulating their interactions and the energy deposition. The information about the location and momentum of simulated particles at selected places are saved in a object called *Track References*.

The simulated hits represent the ideal detector response, then the conversion to digital signal and the formatting of the front-end electronics is ap-

plied (*summable digits*). The summable digits of all input streams have to be added, combined with noise, converted to digital values taking into account possible thresholds, and stored in the digits container (*summable digits* $\rightarrow$ *digits*). The results should resemble closely the real data that will be reproduced by the detector.

4.4 ITS Upgrade simulation

4.4.1 Geometrical simulation of the detector

As previously discussed, the main requirement to be satisfied by the ITSUpgrade simulation tool is its flexibility, in order to easily change the geometric features of the design to investigate how to ameliorate the layout in term of impact parameter resolution, transverse momentum resolution and the tracking efficiency. The tool is flexible not only in the geometrical parameters such as the radius of the layer, the thickness, the segmentation of the single cell, but also in the description of the sensor of the detector, as for example its response to the passage of a particle. This aspect will be simulated in details in the near future, when the technology to be used for the sensor, the dimensions and all the services will be chosen and developed.

Here we start to describe the simulation of the main elements of the detector. The ITS has cylindrical symmetry around the beam pipe: hence the basic element that constitutes one single layer of the detector is a cylinder. It is made of silicon, that is the sensitive part of the detector (the sensor),

surrounded by a copper cylinder: this material is needed to simulate the whole material budget in terms of electronic, cables, supports and so on. Specifically, since the sensor will be made of silicon, the real thickness of the sensor has to be simulated, to have a realistic idea of the signal formation in the active region of the layer; therefore the 'non sensitive' part of the detector contains all the material needed to reach the total wanted material budget, and in this simulation such material is modeled with a uniform volume of copper.

Each cylinder is actually constituted of N cylindrical sectors, N is a variable number depending on the layer. The sectors are combined together to form the whole cylinder. This choice has been done in order to speed up the selection of the clusters during the Cluster Finder phase (described later in this chapter), that finds and groups clusters divided in smaller containers than the one constituted by the whole cylinder. Such a division of the cylindrical layer into slices or modules would also mimic a more realistic segmentation. A planar geometry of the sensitive modules would differ just slightly from the cylinder slices.

The thickness, the position, the length, the number of the cylindrical sectors, the segmentation of each sector and the number of layers are all parameters to be set in the the Config.C file.

The Upgrade project foresees also for a new beam pipe with a smaller radius and thickness, so the beam pipe has also been simulated: it is a beryl-

lium cylinder with radium, thickness and length that can be set externally in the Config.C, according to the need. The final chosen value for the radius of the first layer will have to comply with the limits on the smallest possible radius for the beam pipe, which will be determined by the LHC technical co-ordination.

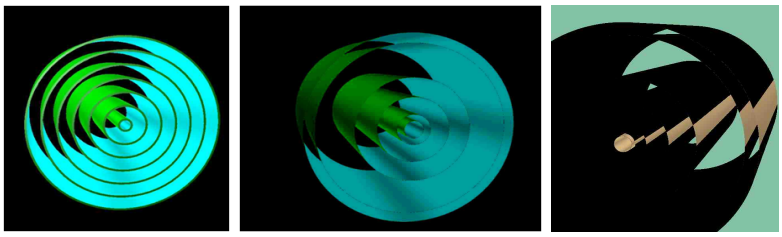

Figure 4.2: ITS Upgrade Simulation tool. Left: geometrical simulation of a 7-layer ITSUpgrade layout. Center: ITS current layout as simulated with the ITSUpgrade tool. Right: ITS current layout: cylindrical sectors in each layer are coloured in yellow. The beam pipe is also shown, in yellow too.

In Figure 4.2, (left), an example of seven layers layout is shown: each layer is made of silicon (green) and copper (cyan). In the same figure (center) the six layer layout is shown, with radii and thicknesses set as the current ITS. In the rightmost part of Figure 4.2 the current layout is shown again, this time with the cylindrical sectors (the modules) and the beam pipe (the cylinder with the smallest radius), highlighted.

As a first validation of the code, we have tried to reproduce the current ITS-layout, choosing the variable mentioned before as in the table 4.1, and investigating the hits and the residual distribution, as it will be shown in the following sections.

Table 4.1: Default layout of the geometry settings parameterizing the actual ITS layout and material budget. X/X_0 is the thickness in terms of radiation lenghts; rφ resolution and z resolution.

	R [cm]	thickness [μm]	x/X_0 [%]	$r\varphi$ res. [μm]	z res. [μm]
Si [Layer 0]	4	150	0.16	9	120
Cu [Layer 0]	4.015	150	1.045101	-	-
Si [Layer 1]	7.6	150	0.160105	12.01	120.09
Cu [Layer 1]	7.615	150	1.045101	-	-
Si [Layer 2]	14.9	150	0.160105	35	28.00
Cu [Layer 2]	14.915	150	1.045101	-	-
Si [Layer 3]	23.8	150	0.160105	35.05	28.00
Cu [Layer 3]	23.815	150	1.045101	-	-
Si [Layer 4]	39.100	150	0.160105	20.01	829.94
Cu [Layer 4]	39.115	150	1.045101	-	-
Si [Layer 5]	43.600	150	0.160105	20.01	829.94
Cu [Layer5]	43.615	150	1.045101	-	-

4.4.2 Transport code simulation with Geant3 and Response Model

After the geometry has been drawn, the passage of produced particles through the material of the detector volume has to be simulated by means of the GEANT3 package [63]. Two types of information are stored at the end of the transport process: the detector *Hits* and the *Track Reference*. As it was already mentioned, the detector hits contain information on the energy deposition inside the sensitive medium (e.g., the energy loss), the track reference consists in the position of the MC particle when exiting a sensitive module. The former is used to create the detector response, whereas the latter is important for debugging purposes at the reconstruction phase. We are simulating a digital particle hit: when a particle hits a given sensor,

the sensor will record a signal, which allows one to locate the impact point of the particle on the layer where the sensor is located. The detector response is a detail that will be implemented when the silicon technology will be defined.

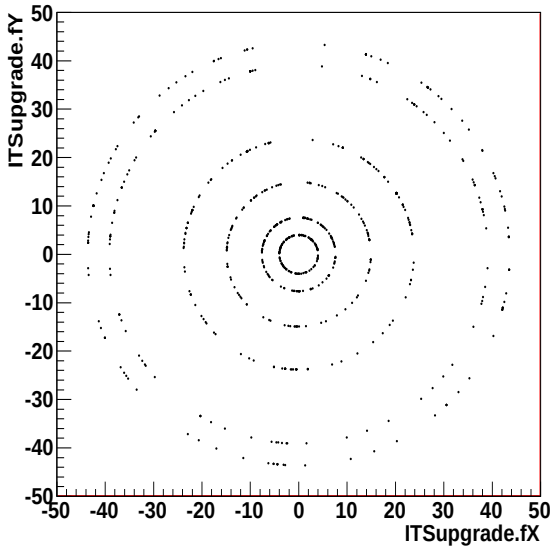

Figure 4.3: Hit Map distribution in each of the six layers of the ITSUpgrade simulated within the current layout. A sample of 120 pions has been generated.

The hit distribution of the current layout simulated with the new code in the transverse plane X-Y is shown in figure 4.3.

The description of the detector has been conceived to comply with any detector segmentations and sensor thicknesses. The basic idea consists in considering each silicon cylinder as divided into a virtual grid of pixels, as explained in the previous subsection concerning the geometry of the detector. If a MC particle looses energy inside the silicon volume, the virtual cells laying on top of it are considered fired. Such fired cells are called *Digits*. The detector response is assumed to be the one of an ideal digital detector

and the number of electron-hole pairs is obtained as N_{pairs}=ΔE_{loss}/(3.6 eV). No diffusion or border effects are taken into account to form the signal and no low charge threshold is applied. An advantage of such an approach is that the cell segmentation is strictly related to the desired resolution. If the cell has a size $d_{r\varphi}$, d_z perpendicularly and parallel to the beam axis respectively, the expected resolutions will be given by $d_{r\varphi}/\sqrt{12}$, $d_z/\sqrt{12}$, as can be seen in Figure 4.4: the residuals between the cluster coordinate in the global coordinates and the track reference are compatible with the resolutions as in table 4.1. This proves that the resolution is easily handled by the user by means of the cell segmentation.

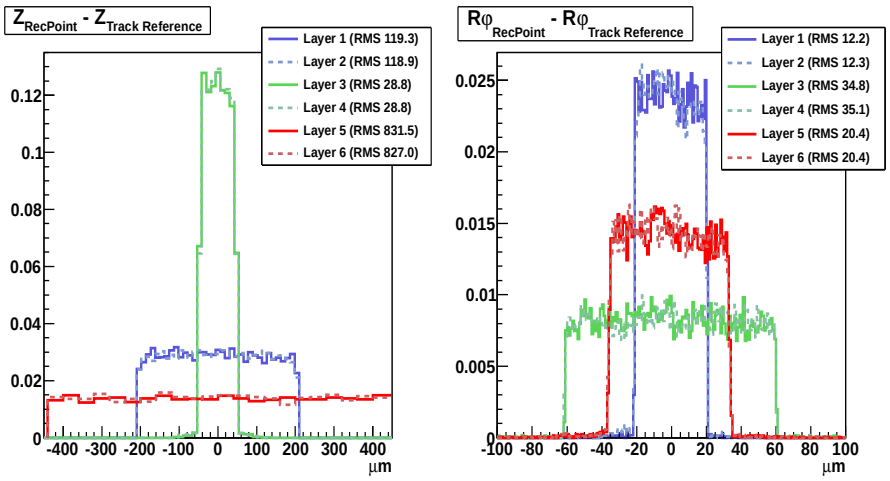

Figure 4.4: Residuals between the reconstructed clusters and the Track Reference position in central Pb–Pb MC events. The $r\phi$ residuals are shown on the left, whereas the z residuals are shown on the right. All the histograms are normalized to the number of entries and the RMS values are also given for each layer. The standard ITS layout as shown in table 4.1 was used.

The simulated digit contains also the information (label index) on the MC particles which has produced it.

4.4.3 Cluster Finder

In a high multiplicity scenario more particles can cross the same or adjacent cells. The cluster finder consists in grouping adjacent digits in one single cluster. The clusters are then built out of digits which have in common one side or one corner. The cluster charge is the sum of the charged of each digit in the cluster cell[1].

The different cluster shapes are shown in the left panel of Figure 4.5. The right panel of 4.5 shows their frequency distributions obtained from 5 central Pb–Pb collisions (at $\sqrt{s_{NN}} = 5.5$ TeV, using the Hijing [65] generator). Most of the clusters are formed by one fired pixel only[2]. The first

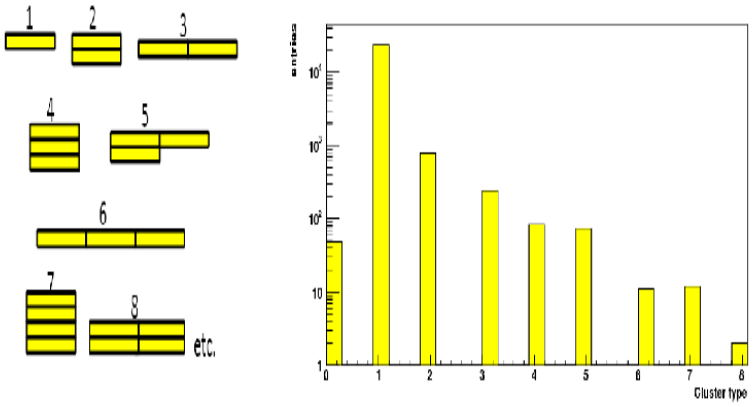

Figure 4.5: Left: Sketch of the cluster type shapes. Right: Cluster type distribution in the first silicon layer (150 μm thick) in simulated central Pb–Pb collisions. The bin 0 is filled if the cluster shape is different from the standard ones (e.g., for a cluster made of two pixels sharing just a corner).

[1] No low threshold on the cluster charge is applied so all the clusters are stored and can be used. The threshold will be applied in the tracking phase.

[2] The MC labels of the digits are propagated to the cluster as well. By means of these identification numbers a cross check with the Track References as stored during the transport process can be done.

validation of the description of the detector response consists in comparing the cluster charge distribution with a Landau function. Figure 4.6 shows that such distribution is compatible with the energy loss distribution of minimum ionizing particles (mip) which pass through 150 μm of silicon [66]. It has been verified that, when changing the silicon thicknesses between 50-300 μm, the mean values change accordingly to the expected values. Another important check is related to the cluster positioning in the space. It can be easily done by estimating the residuals between the cluster coordinates in the global coordinates and the track reference. Figure 4.4 shows that the RMS of the residuals are compatible with the input resolutions (see 4.1).

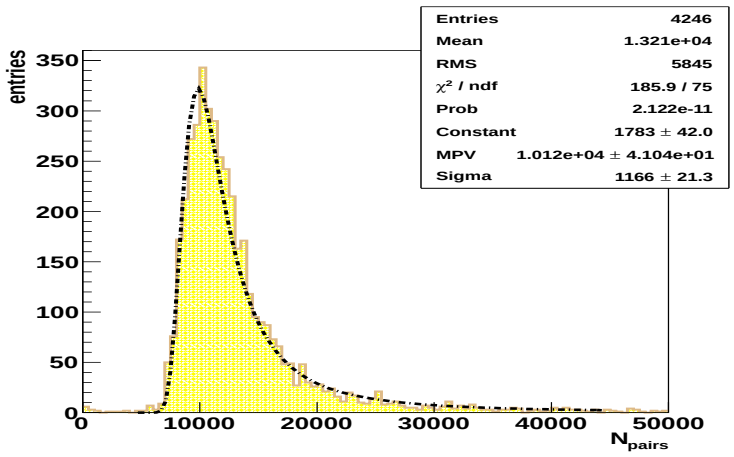

Figure 4.6: Charge distribution in unity of the number of electron-hole pairs (given from $\Delta E_{loss}/3.6\ eV$) for a sample of pions at 1 GeV/c passing through the first silicon layer (150 μm thick). A fit with a Landau function is superimposed.

4.4.4 Global, Local and Tracking reference system

A class has been developed, which manages the features of the layout, as the segmentation, the radii of the layers, the thickness and so on, and save

all the geometric information into a configuration file. This is read in each step of the simulation, from the creation of the digits to the clusterization and also during the tracking procedure, to reach the information about the layout. This class also manages the transformations between the different reference systems for the coordinates of the hits in each step of the reconstruction of the track, from the clusters in the ITS, to the tracking reconstruction. There are basically three reference systems involved: (fig.4.7). The definition of the 'Global' ALICE coordinate system, is already given in chapter 2, in the following the 'local' and 'tracking' reference systems are defined:

- Local: the local coordinate system is defined as a right handed-Cartesian coordinate system with the origin at the center of each sub-detector's 'sensitive surface' (ITS module) and the z axis coinciding with that of the global ALICE coordinate system; the x axis is coincident to

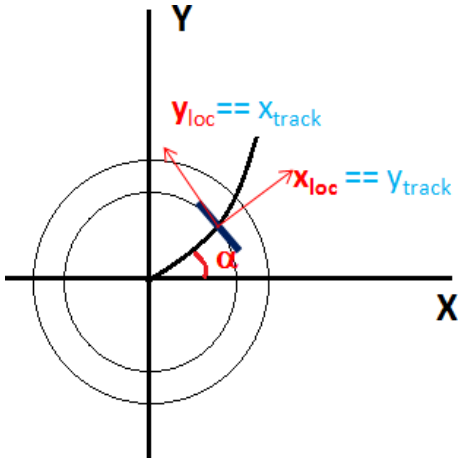

Figure 4.7: Different reference systems view in the transverse plane: the global reference system is in black, the local reference system in red and the tracking reference system in cyan

the ($r\phi$) coordinate and the y coordinate is perpendicular to the ITS module.

- Tracking: in this reference system the origin is at the center of each module and the z axis coincides with that of the global reference system. The x and y axis are swapped each other with respect the local reference system: the x axis is perpendicular to the module and the y axis is the radial coordinate ($r\phi$) of the hit. The "tracking" system is convenient for the tracking and it is the same for all other barrel detectors that contribute to the combined reconstruction.

4.4.5 Stand-alone Tracking Algorithm

Each charged particle going through the detectors leaves a number of discrete signals that measure the position of the points where it has passed. The Tracking Algorithm assigns these space points to tracks and reconstructs their kinematics.

The algorithm is derived from the stand-alone tracker developed for the current ITS [41] and it has been tuned and adapted to take into account the differences of the ITS Upgrade with respect the present detector: the variable number of layers and the simplified geometry, but also the different structure of the cluster containers and the object describing the tracks. Hereafter the two main phases of the tracking procedure are briefly summarized, but for a detailed description of the tracking algorithm we refer to [41].

The tracking scheme consists of two main phases: the 'track finding' and the 'track fitting'.

- Track Finding:

  The track finding method is based on the Kalman filter algorithm widely used in high-energy physics experiments. The clusters are sorted in containers for each layer and cluster charge selection is applied to reject background clusters. The low threshold is set at the value of $7e^{-}/\mu m$ times the thickness of the sensitive region (see for instance the figure 4.6), and thus it depends on the thickness of each layer. The algorithm begins by choosing a cluster in the starting layer and attaching a cluster in the next layer, layer by layer. The 'path' goes from the inner layer to the outer one or viceversa, depending on a choice set in the configuration file ('inward' or 'forward' finding). An inward finding is preferred in a high multiplicity environment, because of the lower occupancy of the outer layer with respect to the inner one. More in details: the algorithm starts from a cluster in the outermost (inward finding) or in the first (outward finding) layer, and searches the compatible cluster in the next layer inside a window in (λ, ϕ) where λ and ϕ are respectively the polar and azimuthal angle in the global reference system. The track seeding is performed using all the pairs of clusters in the first two starting layers and the position of the vertex (see chapter 2) and the calculation of the curvature of the track is done using this three points. This procedure is then applied for all the

layers, using the last three found points for the estimation of the track curvature. The function builds a 'candidate' track, which can be defined as a group of reconstructed points found on all the layers within the same (θ, ϕ) window (fig. 4.8). This also means that a 'candidate' track can have more than one cluster associated in each layer due to the fact that more than one point can enter the search window on the same layer. This redundancy is eliminated by the fitting procedure described below.

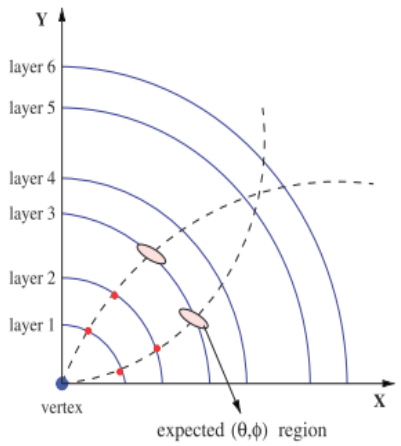

Figure 4.8: Track Finding: the Search Cluster method assign all the cluster within the (ϕ, λ) window, to a 'candidate' track.

- Track Fitting:

  After the selection of 'candidate' tracks is done, a procedure based on the Kalman Filter fits all the combinations of the different cluster of the same layer and selects and store the track with the lowest χ^2. The algorithm starts with a loop over all the possible combinations among the clusters associated to the 'candidate' track, so it defines a

general track among all the combinations of cluster in each layer. In this loop, for each track, two clusters in two different layers are picked; the curvature of the track is calculated using the vertex and these two clusters. The initial values of the track parameters and its covariance matrix are calculated using the positions of the two clusters at layers 1 and 2 and the primary vertex. Then the track is propagated in the magnetic field along the radial direction (500 μm step), modifying continuously the parameters and the covariance matrix of the track. Moreover in the particle's passage though the layers, a correction is done for the layer material, and the track parameters and its covariance matrix are updated. At the end of these processes, a track list of all the candidate tracks is obtained. The algorithm goes ahead selecting the track with the lowestt χ^2, given by the sum of all the differences between the fitted track points and the cluster positions (fig. 4.9).

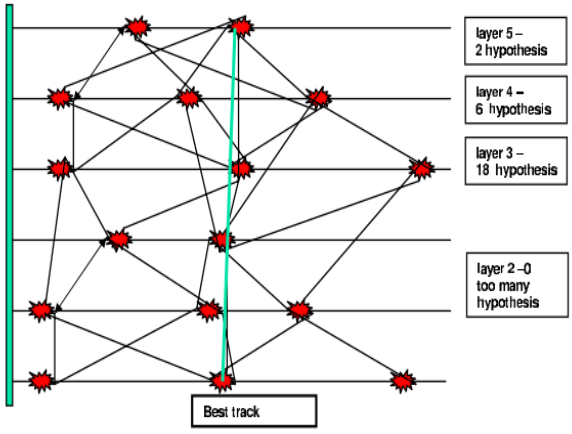

Figure 4.9: Track Fitting: the best track among all the group of clusters associated to a 'candidate' track, is selected according to the χ^2

The labels of the clusters associated to the chosen track are 'cooked': a reconstructed track can be made of clusters produced by more than one particle; each particle has an associated label, so the more frequent label is then assigned to the track. If a track has been built with at least a cluster produced by a different particle, the track is marked as 'fake'. When the 'best' track is chosen, the reconstructed points associated to it are removed from the cluster container and will not be reused in the next iteration of the cluster searching to build other 'candidate' tracks. The fitted tracks are then stored in a 'track object' (AliESDtrack) already implemented in the AliRoot Framework.

4.5 Tracking Performance: impact parameter resolution, transverse momentum resolution

The algorithm has been validated both for pp and Pb–Pb events. The validation has been done taking as a factor of merit the resolution of impact parameter in $r\phi$ and z plane, and the transverse momentum resolution.

The figure 4.10 shows the official performance plot of the ITS stand-alone in a sample of pp collision at 7 TeV and the superimposed performance of the ITSUpgrade tool on a MC sample of generated tracks. The selection of the tracks is done both for the official ITS stand-alone tracker and for the ITS Upgrade stand-alone tracker requiring at least one cluster in each layer and selecting the tracks with $\chi^2 < 3$. It can be note a perfect agreement between the resolution for the three particles species. This means that also

the tracking algorithm is validated.

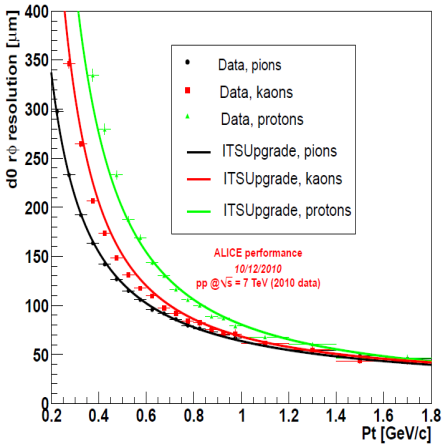

Figure 4.10: Impact parameter resolution in the transverse plane as the function of p_T in pp collisions at $\sqrt{s}$ =7 TeV with the ITS stand-alone compared to the predictions of the MC ITS Upgrade simulation obtained with the current ITS setting.

A good agreement is also found for the z component of the impact parameter and the p_T resolution, as shown in figure 4.11 where the resolution of the z impact parameter for the official ITS stand-alone and the ITS Upgrade stand-alone tracker are shown. In figure 4.12 the transverse momentum resolution is shown. For these figures the comparison is done using a sample of pp MC events, with the reference ITS results taken from [41].

In Pb–Pb events the reconstruction of the tracks is more challenging compared to pp event, owing to the higher particle density. To further verify the good behavior of the tool, a MC Pb–Pb sample has been simulated, within the HIJING generator, that yields a charged particle multiplicity in central collisions similar to the one measured at the LHC. In Figure 4.13 the p_T spectrum measured with the ITSUpgrade tool sets as the current ITS is

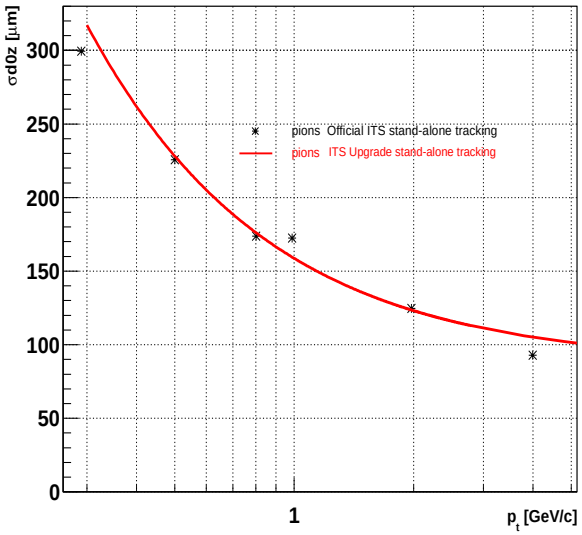

Figure 4.11: Impact parameter resolution in the z-coordinate as the function of p_T in pp collisions at $\sqrt{s}$ =7 TeV with the ITS stand-alone compared to the predictions of the MC ITS Upgrade simulation obtained with the current ITS settings.

shown. The black points represents the p_T spectrum of the MC generated particle, the blue points are the reconstructed tracks, to which correspond the ideal p_T of the MC truth that is assigned, and the red points correspond to the reconstructed tracks with the reconstructed p_T. Within the p_T resolution one expects a slight deviation from the blue and black curves. The green points, finally, describe the behavior of the 'good' tracks, that are the tracks with all the cluster belonging to the same MC particle (no fakes clusters associated to the track). Therefore a good performance of the tracking is obtained also in the Pb–Pb environment.

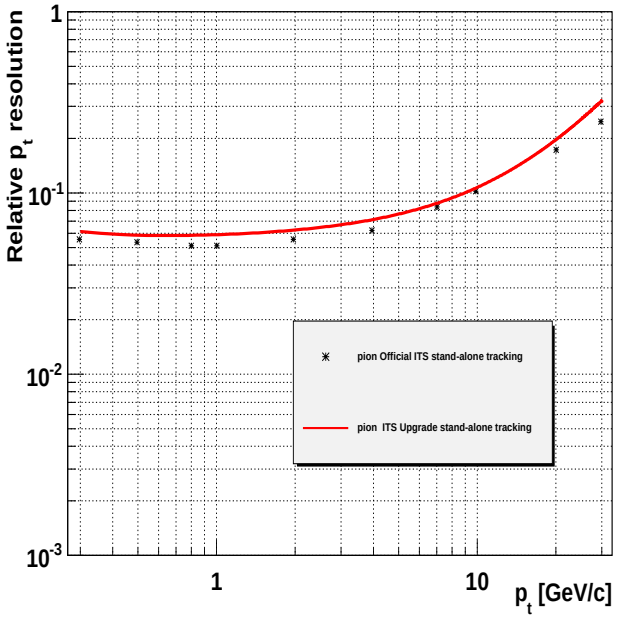

Figure 4.12: Comparison of the p_T resolution for the standard ITS stand-alone tracking and for the ITS stand-alone Upgrade tool, set as the present ITS layout.

4.6 Fast Tool simulation

A complementary semi-analytical MC approach (the Fast-Estimation-Tool FET) based on a tool developed by the STAR collaboration [78] has been developed. It allows to build a simple detector model and a tracking method (a detailed description of this tool can be found in [79]). This tool helps in the design of the detector, to optimize quickly the best position of the different layers, the intrinsic resolution of each sensor and the thickness that provide the best spatial and momentum resolution. In order to have the first layer L0 at a smaller radius than presently, the beam pipe radius has been simulated reducing its radius to 2.0 cm with a thickness of 0.5 mm.

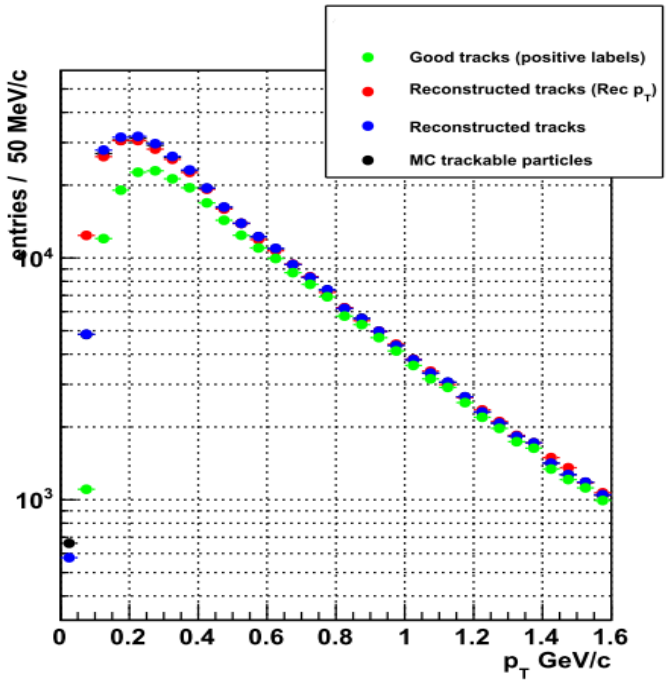

Figure 4.13: Comparison of the reconstructed p_T spectrum, for the ITS stand-alone Upgrade tool, set as the present ITS layout. p_T MC generated spectrum (black), reconstructed tracks with the ideal MC p_T (blue), reconstructed tracks with the reconstructed p_T (red), good tracks (green).

4.6.1 Impact of the first L0 layer on the impact parameter resolution.

An improvement of the impact parameter can be achieved by reducing the layer distance to the vertex, that lets to improve the cluster resolution reducing the measurement error, and a reduction of the material budget that permits to decrease the effect of the multiple scattering. For these study the configuration of the present ITS with the addition of a new layer (L0) has been investigated. As it is already discussed in the previous chapters, the properties of the first two layer are fundamental to the reconstruction of primary and secondary vertex. It has been studied that in particular these

performance depends from the layout of the first layer, the closer one to the beam line.

By positioning the new layer at a radius of 2.2 cm, an improvement of the pointing resolution in $r\phi$ and z of 35% and 22% respectively (at p_T=1 GeV/c) can be expected, as can be noted from figure 4.14.

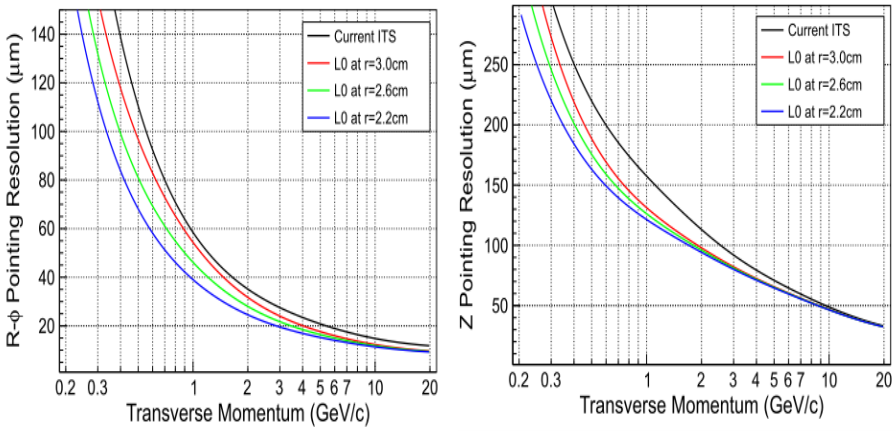

Figure 4.14: $r\phi$ (left) and z (right) pointing resolutions of charged pions at the primary vertex versus transverse momentum p_T for different radii of the layer L0.

In Fig. 4.15 the pointing resolution as a function of the transverse momentum is shown in the case of layer L0 placed at 2.2 cm and three values of its relative radiation length X/X_0 (i.e. the material budget), assuming the spatial resolution of the current pixel detector. The results for the current ITS without L0 is also reported for comparison.

Assuming the layer L0 situated at a radius or 2.2 cm, a decrease of the material budget from X/X$_0$=1.14 % to X/X$_0$=0.3 % would lead to an improvement of the pointing resolution in $r\phi$ and z by a total of 48 % and 22 % respectively, at p_T = 1 GeV/c: see Fig.4.15. The impact on the pointing

resolution in z direction is, although visible at very small p_T, marginal at p_T>1 GeV/c.

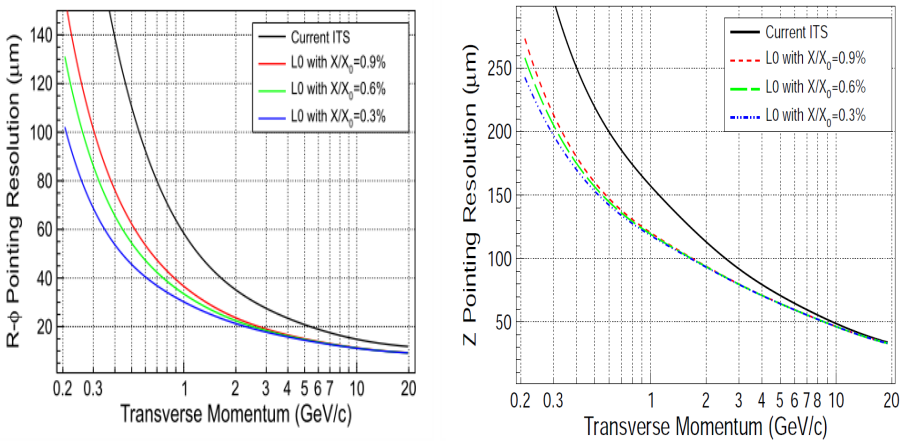

Figure 4.15: $r\phi$ (left) and z (right) pointing resolution of charged pions at the primary vertex versus transverse momentum p_T for different material budget of the layer L0.

As shown in Fig. 4.16, an improved cluster resolution of layer L0 equal to 4 μm (with r=2.2 cm and X/X_0=0.3 %) leads to a total improvement of the pointing resolution in $r\phi$ by about 60 % at p_T=1 GeV/c. The improvement of 78 % in the z pointing resolution can be attribuited to the major improvement of the cluster resolution in z from previously σ_z = 130 μm to σ_z = 12 μm. A change from 12 to 4 μm is, although visible at high momentum, almost negligible at p_T=1 GeV/c.

It can be concluded that the features of the first layer is important to the determination of the impact parameter resolution and the transverse momentum resolution.

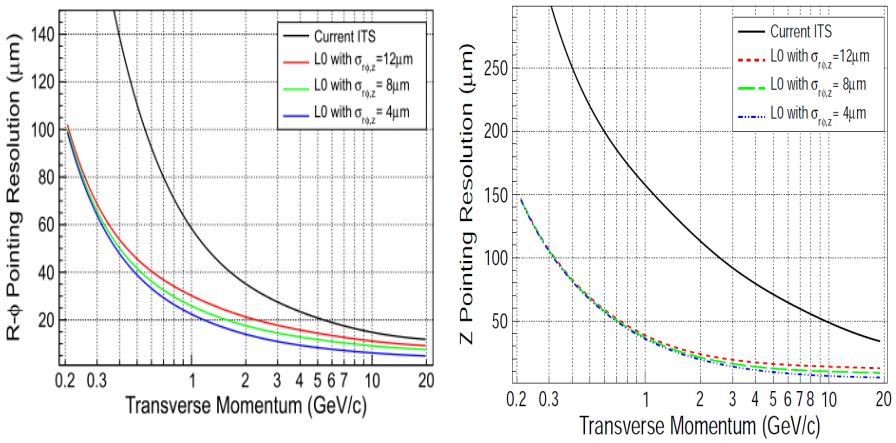

Figure 4.16: $r\phi$ (left) and z (right) pointing resolution of charged pions at the primary vertex versus transverse momentum p_T for different values of the intrinsic spatial resolution of the layer L0.

4.7 7-layers Upgrade Scenario

Two different layouts of the ITS Upgrade will be studied in term of their performance, in particular on the impact parameter resolution, transverse momentum resolution and tracking efficiency.

The transverse momentum resolution is estimated by considering the residual distribution between the p_T of simulated tracks and the reconstructed p_T. An improvement in the transverse momentum resolution of the ITS stand-alone tracking would allow a better reconstruction of the invariant mass distribution, which is affected by the momentum resolution of the decays tracks.

In this paragraph we discuss two different layouts both with 7 layers:

1. 'AllNew': in this scenario the replacement of the entire ITS with seven

Table 4.2: "SPDNew"

Layer / Type	r [cm]	$\pm z$ [cm]	Resolution $r\phi \times z$ $[\mu\text{m}^2]$	Material budget X/X_0 [%]
Beam pipe	2.0	-	-	0.22
1 / new pixel	2.2	10.5	4×4	0.30
2 / new pixel	4.7	13.5	4×4	0.30
3 / new pixel	9.0	18.5	4×4	0.30
4 / drift	15.0	22.2	35×25	1.13
5 / drift	23.9	29.7	35×25	1.26
6 / strip	38.0	43.1	20×830	0.83
7 / strip	43.0	48.9	20×830	0.83

layers of silicon pixel-like detectors with less material budget then the actual and a finer pixel segmentation is considered to improve the spatial and momentum resolution. The first layer is closer to the beam pipe (which would require a new beam pipe with a smaller radius)

2. 'SPDNew': in this scenario only the current two SPD layers are replaced by three new layers of pixel detector, with the first layer closer to the beam pipe. The SDD and SSD layers are unchanged.

The specifications of the layouts described above are summarized in tables in 4.2 and 4.3 respectively.

The resolution chosen for each sensor of the three 'new' layers of 'SPDNew' and all the layers of 'AllNew' is 4 μm both in $r\varphi$ and in z, the first layer is at 2.2 cm, and the material budget in terms of radiation length is 0.3%.

Table 4.3: Characteristics of the Upgrade Scenario 2 - "AllNew"

Layer / Type	r [cm]	$\pm z$ [cm]	Nominal resolution $r\phi \times z$ $[\mu\text{m}^2]$	Material budget X/X_0 [%]
Beam pipe	2.0	-	-	0.22
1 / new pixel	2.2	10.5	4×4	0.30
2 / new pixel	2.8	11.2	4×4	0.30
3 / new pixel	3.6	12.3	4×4	0.30
4 / new pixel	20.0	30.7	4×4	0.30
5 / new pixel	22.0	33.0	4×4	0.30
6 / new pixel	41.0	54.5	4×4	0.30
7 / new pixel	43.0	56.8	4×4	0.30

MC samples of twenty pions have been generated, each with different values of transverse momentum, from 0.3 GeV/c to 30 GeV/c. We compare the performance of these new layout 1) and 2), with that of the current ITS.

Figure 4.17 shows the impact parameter resolution in the transverse ($r\varphi$) plane in the 'AllNew' layout (in red), which is superimposed to the green curve of the 'SPDNew'. A comparison is done with the current ITS layout (black curve).

In figure 4.18 the impact parameter resolutions in the z plane, of the 'AllNew' (red), again superimposed to the 'SPDNew' (green) layout are compared with the current layout (black). The impact parameter resolution achieved with the two layouts is the same: this is due to the fact that the first two layers mainly contribute to this resolution. The improvement in the transverse plane correspond to a factor 2 at 1 GeV/c; the improvement

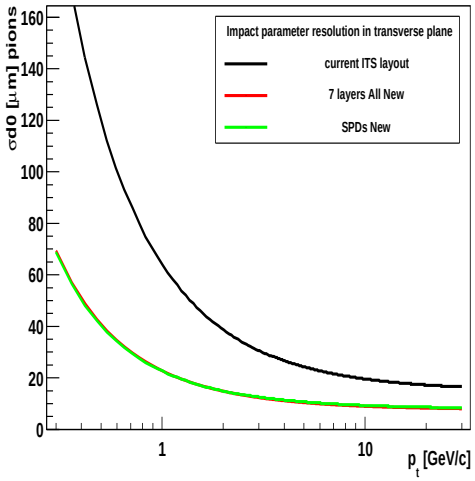

Figure 4.17: Impact parameter resolution in transverse plane. (pions)

is even better in z (at 1 GeV/c 40 μm versus the currents 160 μm), because the increase of the intrinsic resolution in z is considerable (from 120 μm in the current ITS to 4 μm).

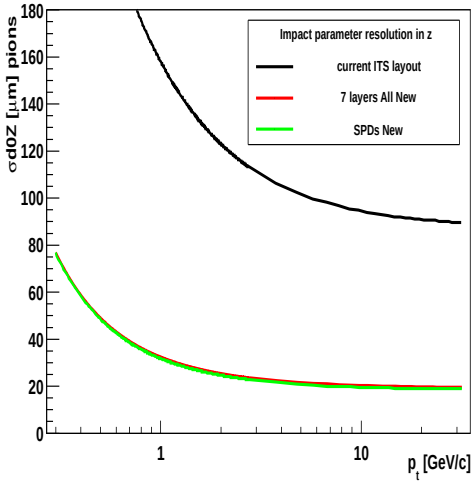

Figure 4.18: Impact parameter resolution versus p_T in z. (pions)

In figure 4.19 the transverse momentum resolution for the 'AllNew'(red) and 'SPDNew' (green) configuration is compared with the current layout

(black). Here a better improvement of the 'AllNew' configuration, with respect of the 'SPDNew' one, is observed. This is because also the configuration of the external layers are fundamental for the measurement of the momentum.

Finally, it is important to stress that the configuration will be also evaluated with respect to the production cost. Obviously the 'SPDNew' is the cheapest option, but at the same time the improvement in the p_T resolution is less effective than the 'AllNew', which is more expensive. Conversely, the 'SPDNew' is not convenient because, holding the SDD, it would be not able to satisfy the request of high read-out up to 500 kHz, due to the limitation by the electron drift time.

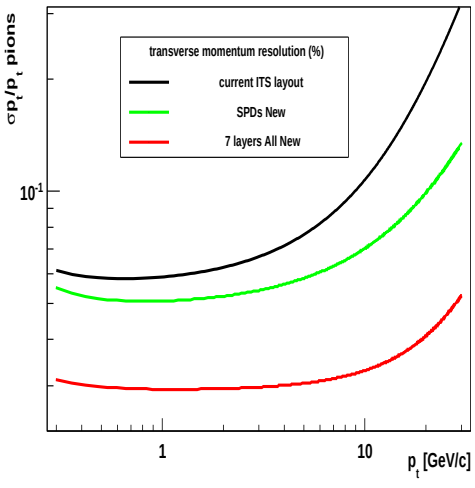

Figure 4.19: Transverse momentum resolution versus p_T (pions).

4.7.1 Tracking efficiency

The 'tracking efficiency' is defined as the

number of reconstructed track / number of trackable particles

A 'trackable particle' is defined as the particle generated with at least three track references in three different layers of the ITS (see fig. 4.20). The reconstructed tracks are selected by requiring at least three associated clusters and without any fake associated cluster from other tracks.

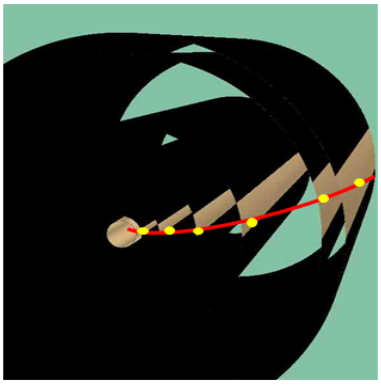

Figure 4.20: Passage of the particle through the ITS layers. Each yellow point represents a hit on each layer (Track References).

A good initial seeding is fundamental to an effective reconstruction of the track, so it becomes important to group the inner or outermost layers (for a forward or inward tracking, respectively) to obtain a high tracking efficiency in the ITS stand-alone tracking mode. Thus, besides the 'AllNew' and the 'SPDNew', a third layout is considered with 8 layers: it corresponds to the "AllNew" with the addition of a layer very close to the seventh layer (last layer at radius = 43.4 cm, seventh layers at r_7= 43.0 cm). This last layout provides a more effective track seeding in the track finding method

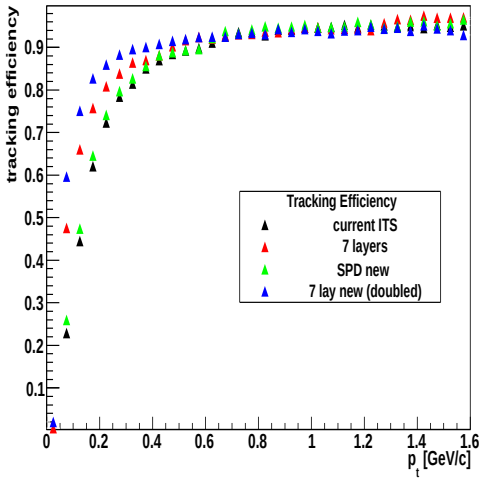

Figure 4.21: Tracking Efficiency for different layout in comparison with the current ITS layout. The main differences are at low pt, and the configuration with a double layer (7 layers All New doubled) has the best tracking efficiency since 0.2 GeV/c

(inward) within the two external layers closer each others.

In figure 4.21 the tracking efficiency versus p_T in the three different layouts is shown. It can be seen that the '7lay new doubled' configuration leads to a better tracking efficiency down to p_T>0.2.

The 'AllNew' provide a better tracking efficiency at low p_T compared to the 'SPDNew': a good spatial resolution also in the outer layers is relevant not only to improve the p_T resolution, but also for the tracking efficiency in the ITS stand-alone mode. This means that the outermost layers properties are fundamental if we want provide a optimal reconstruction performance, independent from the TPC.

Chapter 5

Performance Study on the benchmark channel Λ_c

The physics motivations for the measurement of charm baryon production has been discussed in the Chapter 3. In this Chapter the present performance of the Λ_c analysis with ALICE is presented. It has been discussed how an upgrade of the ITS would improve the spatial and momentum resolution, thus leading to a better performance in secondary vertex reconstruction. The method used to simulate the performance of the ITS Upgrade is described in this chapter, and the results obtained with the upgraded detector are presented for the channel $\Lambda_c \to pK\pi$.

5.1 Analysis of Λ_c with the current ITS

Presently, the Λ_c signal was observed by ALICE in the $pK^-\pi^+$ decay channel: in figure 5.1, the invariant mass distribution of Λ_c candidates with $p_{\mathrm{t}} > 3$ GeV/c is shown. It is obtained from a data sample of 1.9×10^8

proton–proton events, collected with the ALICE minimum bias trigger, at $\sqrt{s} = 7$ TeV. With the present ITS, the signal is observed only at transverse momenta above 3 GeV/c and the statistical significance is relatively low (about 5 σ), as compared to the D meson signals [48].

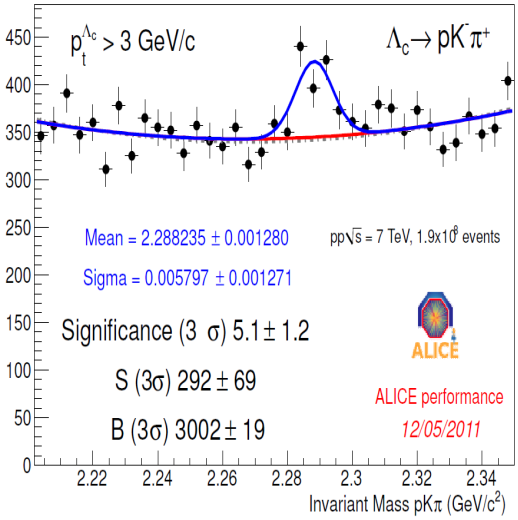

Figure 5.1: $pK\pi$ invariant mass in pp collisions at $\sqrt{s}$=7 TeV measured by ALICE for $p_T > 3$ GeV.

In Pb–Pb collisions the Λ_c measurement seems to be beyond the present ITS setup capabilities. As can be argued from figure 2.13, which shows the impact parameter resolution as a function of p_T in pp and Pb–Pb collisions, the d_0 resolution reaches a values of 65 μm at 1 GeV/c, and is much higher at lower p_T, (up to 300 μm at p_T=300 MeV/c). The cτ of Λ_c is about 60 μm, that is very slow with respect the other open charm mesons: 123 μm for D^0 and 300 μm for D^+, and this make very challenging the Λ_c analysis, that requires a resolution better than a factor of 2 at least, with respect the one obtained with the current ITS.

5.1.1 Analysis Strategy

The 'golden' hadronic decay channel $pK^-\pi^+$ is studied by analyzing the invariant mass of fully-reconstructed three-prong decays, selected by applying topological cuts and particle identification criteria, namely the proton and kaon identification using the TPC and TOF information. Detected particles are combined into candidate topologies that correspond to the studied channel. The invariant mass of each candidate is calculated using the following formula, expressed in natural units:

$$M^2 = (\sum E_i)^2 - ||\sum \vec{p_i}||^2$$

where E_i is the energy of the particle and $\vec{p_i}$ is its momentum. To extimate E_i, a hypothesis on the particle specie of each decay track has to be done, the PID plays its role in this context. The distribution of the invariant mass M^2 is built: the typical distribution presents a peak at the correct value of the particle mass, and a continuous spectrum that is due to the *background*, constituted of the random combinations of other tracks.

Decay hadrons are identified by combining tracks with appropriate charge sign, and applying topological cuts to separate the signal from the combinatorial background.

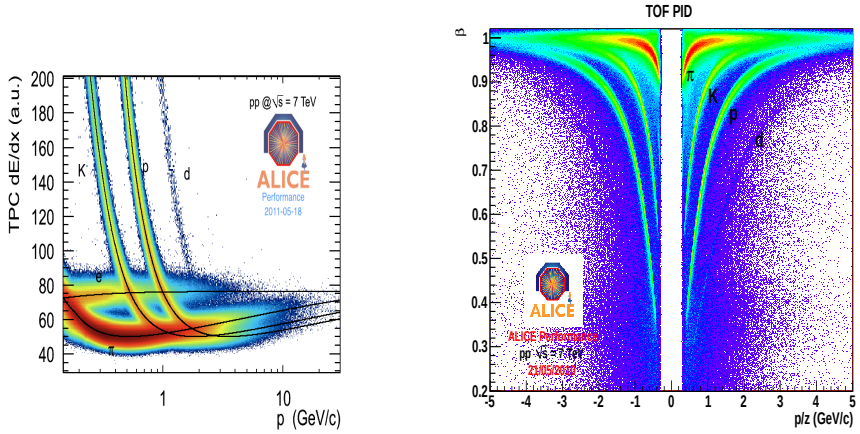

Figure 5.2: Left panel: Specific ionization energy loss $\mathrm{d}E/\mathrm{d}x$ of various particle species in the Time Projection Chamber, as a function of momentum, for 7 TeV pp collisions. The lines are a parametrization of the Bethe-Bloch formula. Right panel: velocity measured by TOF for various particle species as function of signed momentum, for 7 TeV pp collisions.

Particle Identification: PID strategy

The daughters are identified combining the PID information provided by ITS, TPC and TOF. Hadron identification over a very broad momentum range, from 0.1 to 3 GeV/c, is one of the key features of ALICE. The TPC identifies particles with intermediate momenta using the information on the specific energy deposit, $\mathrm{d}E/\mathrm{d}x$, in its volume, as shown in the left panel of figure 5.2 [91]. The ITS covers the low momentum region, going down to 0.1 GeV/c, while TOF is able to distinguish protons up to 3 GeV/c (right panel in fig. 5.2). The three detectors cover the p_T range relevant for the identification of tracks coming from charmed hadron decays, and allow a background reduction by a factor 2-3 in the low momentum region. A different identification strategy for each species has been tuned: the particle is labeled if its curve fall within "N sigma" from the corresponding theoretical

Bethe Bloch curve, using the following criteria:

- *kaon*: 3 sigmas TPC, 3 sigma TOF and 2 sigma ITS
- *proton*: 3 sigmas TPC, 3 sigma TOF and 2 sigma ITS, discard if compatible with pion.
- *pion*: 3 sigma TPC, discard if compatible with proton.
- if there is an ambiguity between TPC and TOF, the decision rely on TOF.

Cuts tuning to reject background

The reconstruction procedure consists of an event-by-event analysis. In each event, only candidates which have passed the cut selections are kept, in order to suppress the combinatorial background. Formation of the triplets belonging to single event is performed in two steps: (i) combination of opposite sign pairs and (ii) creation of triplets from an opposite sign pair and another charged track. In step (i), the loop over the particles starts with the negative tracks (K^-) which are then paired with all the other positive tracks (pion or protons). Here the description of track selections is presented. In the following section, the detailed description of the value chosen for each cut for the ITS Upgrade, is given.

Single Track Selections:

The first step of the selection is applied at the level of single reconstructed tracks before combining them into pairs. At this stage, the selection is based

on transverse momentum p_T.Therefore, assuming that particle identities are known, a cut is made to accept only tracks that satisfy the following conditions:

$p_T^K > p_T^{cut,K}$; $p_T^\pi > p_T^{cut,\pi}$; $p_T^p > p_T^{cut,p}$;

Two Track Selections:

The tracks that have passed the previous selections are combined into pairs with opposite charge signs (K,π or K,p). Common vertex for every pair is then found.

The distance of closest approach between the two tracks (DCA) is then calculated, and a cut is applied to it. For tracks coming from a common secondary vertex this parameter should have relatively small value, while for random background combinations of tracks it could be much bigger. Therefore the following selection criterion can be applied to accept candidate pairs:

$dca(12) < dca(12)^{cut}$

The distance between the two-track vertex and the primary vertex is then calculated: this has to be smaller for background pairs than for signal ones. Thus, the following selection criterion could be introduced to separate "good" candidates:

$dist_{12} > dist_{12}^{cut}$;

However, the considered distance is a first approximation of the dis-

tance between primary vertex and Λ_c decay vertex, that will be measured with more precision when the triplet is formed.

Three Track Selections:

For each selected track pair a third track is added to form a triplet. The added third track together with the opposite sign track of the initial pair must also satisfy the cuts on the pairs described above. Then the three-track vertex is reconstructed and a dispersion parameter is calculated:

$$\sigma^2 = \sum_{k=1}^{2}[(x_k - x_0)^2 + (y_k - y_0)^2 + (z_k - z_0)^2]$$

where (x_0; y_0; z_0) are the coordinates of the found vertex and (x_k; y_k; z_k) are the coordinates of the point that belongs to the track k and which is closest to the vertex.

Then a selection on the $\cos(\theta_{point})$ is applied, where θ_{point} is the pointing angle, i.e. the angle between the direction of the reconstructed Λ_c momentum and the line connecting the primary and secondary vertices. If the found vertex really corresponds to a Λ_c decay vertex, then $\theta_{point} \sim 0$ and $\cos(\theta_{point}) \sim 1$, therefore the selection criterion is:

$$\cos(\theta_{point}) > \cos(\theta_{point})^{cut};$$

The last applied selection criterion is the distance between the primary and secondary vertices. Signal triplets that come from the displaced decay vertex of Λ_C should have on average larger distance from the primary vertex with respect to background triplets. Thus the following selection criterion is

applied:

decayLenght $>$ decayLenght^{cut}

The aim of the cut tuning procedure is to find optimum cut values that maximize the statistical significance defined as:

$$Significance = \frac{S}{\sqrt{S+B}}$$

where S is the number of signal triplets and B is the number of background combinations, in a given mass range (e.g. 3 σ around the mass quark).

5.1.2 Simulation method

In order to quantify the improvement of an upgrade of the ITS, a fast simulation scheme is employed. It is based on existing Monte Carlo productions including the detailed geometry and response of the current ALICE detector setup. The impact of the new ITS is obtained by 'smearing' the parameters of the reconstructed tracks, according to the 'upgraded' spatial and momentum resolutions as obtained by the Monte Carlo tool (see chapter 4). Tracks are parametrized as helices in the Kalman filter description. They are fully described by a 5 parameters track-state vector, which in the local coordinate system is defined as: $x^T = (y, z, \tan\lambda, \sin\phi, 1/p_T)$, where p_T is the transverse momentum and $1/p_T$ is proportional to the curvature of the track projection on the transverse plane, λ is the angle between the track and the transverse plane, and ϕ is the angle between the track projection in the transverse plane and the x axis. If $\sigma^{current}_{d_{0,r\phi}}$, $\sigma^{current}_{d_{0,z}}(p_T)$ and $\sigma^{current}_{1/p_T}(p_T)$ are the resolution obtained with the current layout, and $\sigma^{upgrade}_{d_{0,r\phi}}$, $\sigma^{upgrade}_{d_{0,z}}$

and $\sigma^{upgrade}_{1/p_T}$ that of the upgrade one, the improvement is applied as follow:

$$\begin{pmatrix} y' \\ z' \\ \sin\phi' \\ \tan\lambda' \\ 1/p'_T \end{pmatrix} = \begin{pmatrix} y_{MC} + \sigma^{upgrade}_{d_{0,r\phi}}(p_T)/\sigma^{current}_{d_{0,r\phi}}(p_T) \cdot (y - y_{MC}) \\ z_{MC} + \sigma^{upgrade}_{d_{0,z}}(p_T)/\sigma^{current}_{d_{0,z}}(p_T) \cdot (z - z_{MC}) \\ \sin\phi \\ \tan\lambda \\ (1/p_T)_{MC} + \sigma^{upgrade}_{1/p_T}(p_T)/\sigma^{current}_{1/p_T}(p_T) \cdot ((1/p_T) - (1/p_T)_{MC}) \end{pmatrix}$$

Thus, this is a simple scaling of the residuals of the impact parameters in $r\phi$ and z, as well as of the transverse momentum, with respect to their

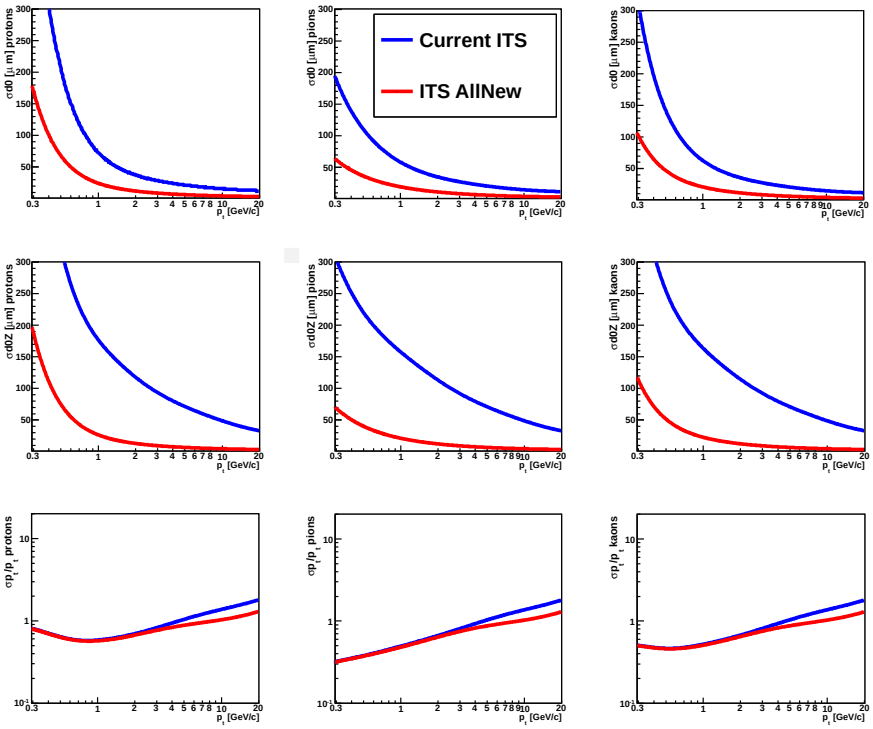

Figure 5.3: Track impact parameter resolution in $r\phi$ and z, and transverse momentum resolution (current in blue and upgrade in red), for protons, pions and kaons.

true values (MC), known from the generated particle kinematics. The scaling factors are the ratios of the upgrade/current resolutions on these variables. The track polar angle θ and the ϕ are assumed to remain unchanged being determined mostly by the TPC. After the scaling is done, the analysis is re-run with the improved parameters. This approach is called *Hybrid*, because it applies the detector performance of the upgraded ITS to full simulations of the current ITS. In this way the correlation between the different parameters stay unchanged.

A drawback of this approach is that it does not allow to study the effect of a complete new detector, 100% efficient and without dead zone. The impact of this extension on the physics performance is not assessed here, but it will be addressed in the near future with dedicated simulation studies.

Figure 5.3 shows the corresponding impact parameter and transverse momentum resolutions as a function of transverse momentum for the upgraded ITS compared to those of the current ITS, for pions, protons and kaons. The scaling factors of the *Hybrid* approach are the ratios of these two resolutions, for each p_T value.

5.2 Performance studies for $\Lambda_c \to pK\pi$

The simulation study reported in this section uses the *Hybrid* approach and the “AllNew" configuration of the ITS.

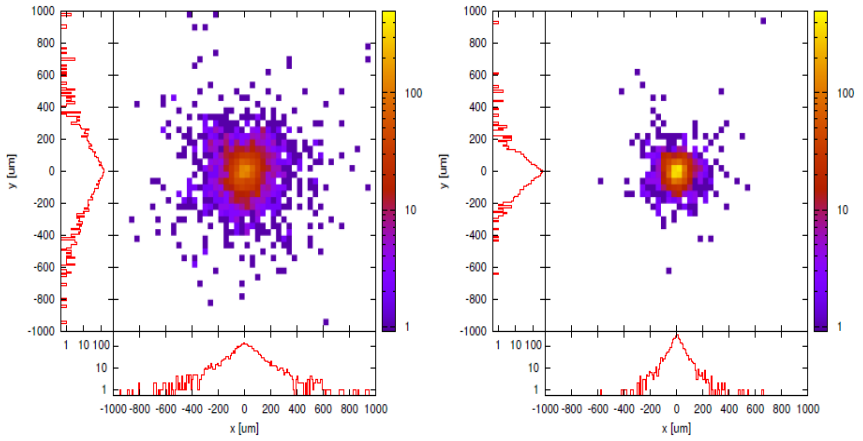

Figure 5.4: Distribution of the residuals between the reconstructed and generated position of decay vertices for $\Lambda_c \to pK^-\pi^+$ in the plane transverse to the beam line, for the present (left) and upgrade (right) ITS scenarios.

The improved vertex resolution obtained with the ITS Upgrade allows a much cleaner separation of decay point from the interaction point with respect to the current ITS. In figure 5.4 the $\Lambda_c \to pK^-\pi^+$ distribution of the residuals between the reconstructed and generated position of secondary vertices in the transverse plane, obtained with the Hybrid method, is shown: the left panel shows the distribution for the current layout and the right panel that for the upgrade scenario.

To optimize the discrimination of the Λ_c signal against the background, which is made mostly of primary particles, a study of the cuts on kinematical and topological variables has been carried out also with the new layout. The analysis cuts optimized to extract the signal in pp collision data at $\sqrt{s} = 7$ TeV were used as a starting point. However, these are not fully adequate for taking advantage of the ITS upgrade potential, because the increased impact parameter resolution provided by the new detector allows

a better discrimination of the signal against the background, hence looser cuts allow to still reject effectively the background but minimize the loss of the signal.

5.2.1 Cuts Optimization

The optimization of the cuts with the ITS Upgrade layout has been performed by studying the distribution of the kinematical variables listed in section 5.1.1. A comparison has been done between the amounts of rejected signal and background with the current analysis cuts and with the new ones: the new cuts represent a compromise between the maximization of the significance and the minimization of the signal loss.

The most relevant changes in the cuts concern the following variables:

- the cut on the p_T of the decay tracks is very powerful: the p_T distribution for each species for the signal differs from that of background candidates, as it can be noted in fig. 5.5. For $p_T^{\Lambda_c} > 4$ GeV/c, the cuts has been tuned to be $p_T^{kaon} > 1.2$ GeV/c, $p_T^{pion} > 1.2$ GeV/c, $p_T^{proton} > 0.4$GeV/c.

- the impact parameter (d_0) of a daughter tracks: this is the distance of closest approach of the track to the primary vertex. The distribution of this variable has a similar shape for signal and background, but it is wider for the background. The cuts $|d_0| < 0.4$ cm has been chosen without significant loss of signal for each species (see fig. 5.6). In the

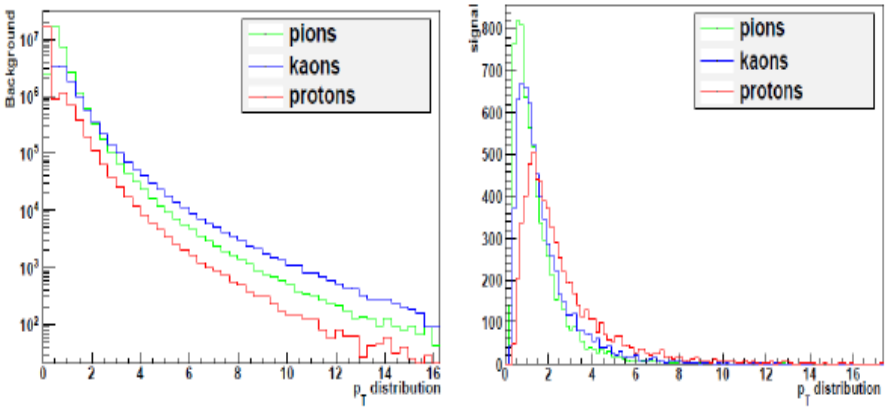

Figure 5.5: Transverse momentum distributions for pions, kaons and protons, for background and signal within the upgrade layout.

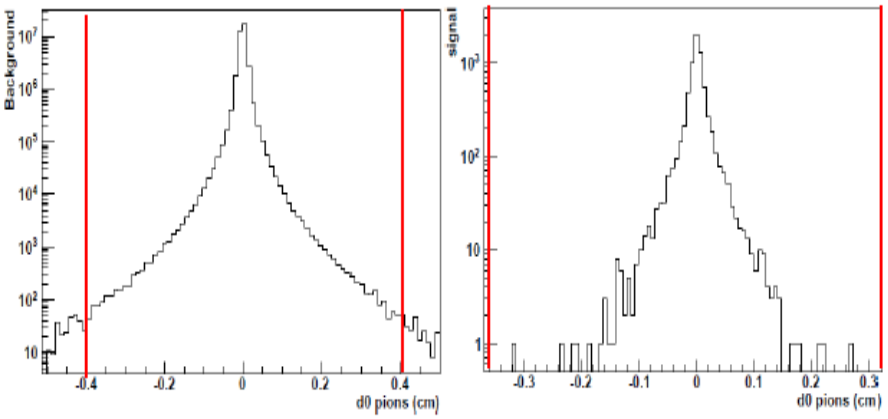

Figure 5.6: Impact parameter distributions of pions, for background and signal within the upgrade layout.

current analysis with the present detector this cut is not used. It's worth to remark that in the current analysis the topological cuts are not selective enough, because, as in the case of the impact parameter distribution, the background and signal distributions are quite similar: thus this type of cut would not be so efficient.

- the cosine of the pointing angle: this variable has a decreasing dis-

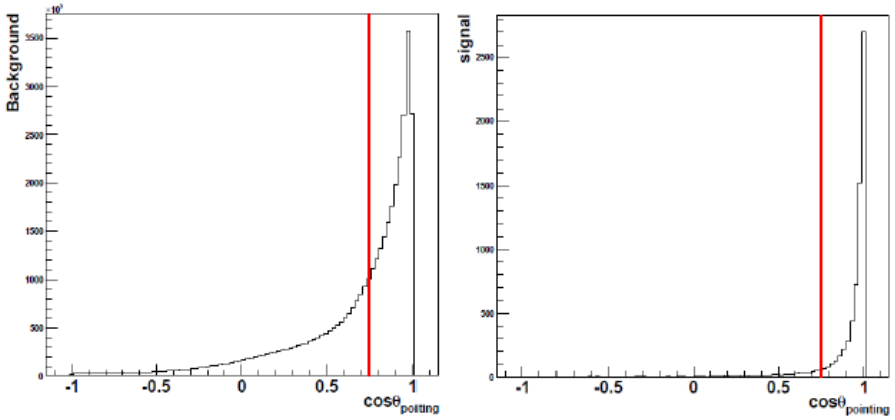

Figure 5.7: Cosin of the pointing angle $\cos\theta_{pointing}$ for background and signal within the upgrade layout.

tribution and for the background it is wider that for the signal: the chosen cut is $\cos\theta_p > 0.75$, which allows to reduce significantly the background and removes very small amount of signal, thus improving the significance, as can be noted in fig. 5.7. In the current analysis with the present detector this cut is $\cos\theta_p > 0$ for $p_T > 4$ GeV/c, the distribution of the signal obtained with the current ITS being broader than in the Upgrade case.

- the decay length (L): the current analysis uses $L > 70$ μm, a further background rejection with the upgraded ITS is achievable by imposing $L > 80$ μm, losing very small amount of signal, again with an improvement in the significance.

- sigma vertex: it is very sensitive to the improved resolution. The current analysis applies a cut to this variable at 600 μm, with the ITS Upgrade the cut is moved to 400 μm (see fig. 5.8), this is feasible

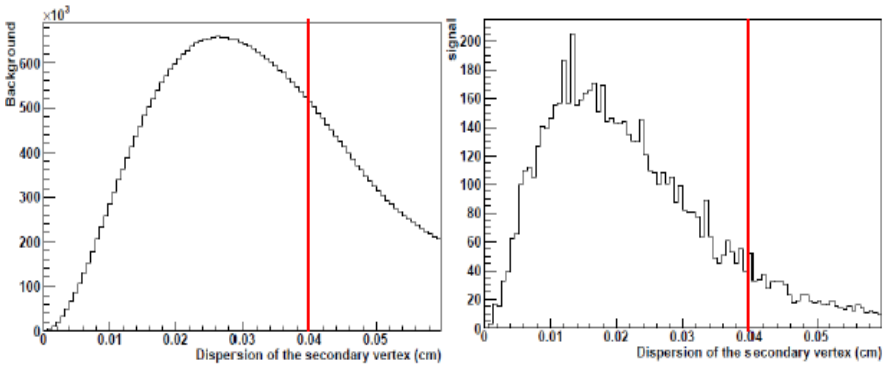

Figure 5.8: Dispersion of the tracks around the secondary vertex for background and signal within the upgrade layout.

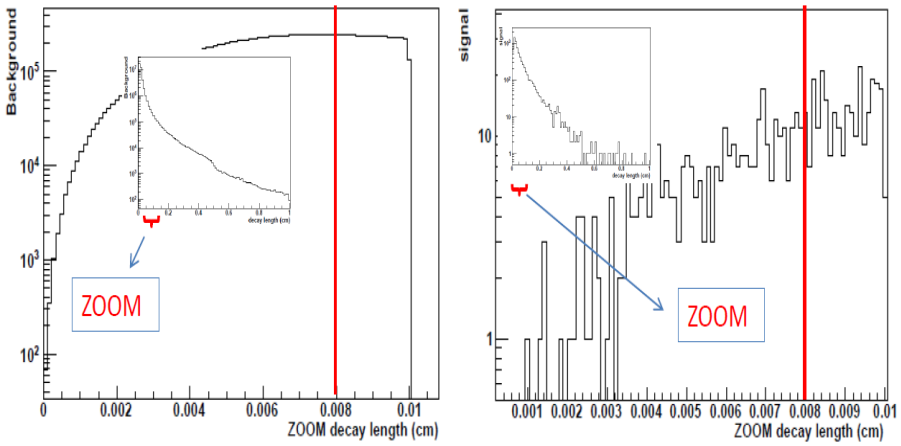

Figure 5.9: Decay length for background and signal within the upgrade layout. In each panel a zoom of the 'cut zone' is shown, and in the little panels the complete distribution of the decay lenght is also shown.

because the signal distribution is narrower with the Upgrade scenario, hence the discrimination of the background is better.

5.2.2 Results

In the right panel of figure 5.10, the invariant mass distribution obtained for the ITS upgrade case is shown, for the same event statistics of

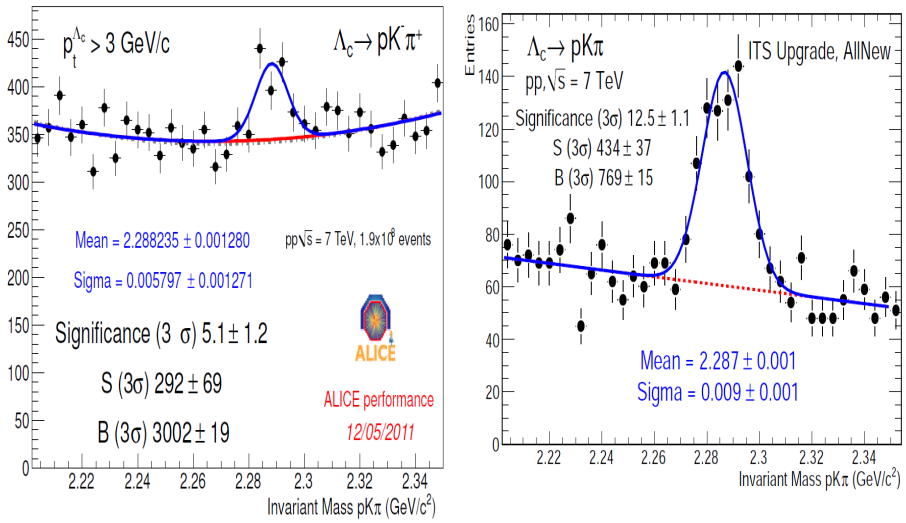

Figure 5.10: Left: $pK\pi$ invariant mass in pp collisions at $\sqrt{s}$=7 TeV measured by ALICE for $p_T > 3$ GeV. Right: Hybrid simulation with the ITS upgrade configuration. The sample statistics in the simulation is the same as in the data, while the selection cuts were optimized specifically for the upgrade scenario.

the current data analysis, which is shown in the left panel of the same figure. The 'upgraded' performance is obtained on a sample of pp events produced with the PYTHIA generator [92, 93] (with the Perugia-0 tune [94]) by rescaling the signal and background yields, in order to match the features observed in data, as explained in the following. For the background, the scaling factor is simply the ratio of the sample sizes for the data and the simulation $N_{\rm data}/N_{\rm MC}$ $(1.9 \times 10^8/1.3 \times 10^8)$. For the signal, in addition to this factor, a 10% correction was included in order to equalize the total $c\bar{c}$ cross section yielded by PYTHIA Perugia-0 to the one measured in ALICE, $\sigma_{\rm pp}^{c\bar{c}} = 7.73 \pm 0.54(stat.)^{+0.74}_{-1.38}(syst.) \pm 0.44(lumi.)^{+1.90}_{-0.87}(extr.)$ mb [95]. For the ITS upgrade scenario, a significance of about 12 is obtained for Λ_c baryons with $p_{\rm t} > 3$ GeV/c, to be compared to the current value on data of about 5. The increase of the signal statistics is of about 50% (looser cuts are used for

the upgrade case) and the increase of the signal-to-background ratio is more than a factor of 5.

Concerning Pb–Pb collisions, the Λ_c signal is currently not observed with the 2010 data sample, because of the very large combinatorial background. The feasibility for an analysis with the ITS upgrade scenario has been studied considering minimum-bias Pb–Pb (0–100% centrality). The *Hybrid* technique was applied to existing Pb–Pb Monte Carlo samples. The combinatorial background was evaluated from a sample produced with the HIJING generator, and it was rescaled so that the background level for the current ITS case in the simulation matches the level observed in the Pb–Pb data, when analyzed with the same selection cuts. The Λ_c signal was evaluated from a sample of HIJING events in which charm particles were added using PYTHIA and forced to decay into selected channels (with the $pK^-\pi^+$ final state in case of Λ_c). The signal was rescaled so that the generated yield matches the expectations for minimum-bias Pb–Pb collisions at top LHC energy $\sqrt{s_{\rm NN}} = 5.5$ TeV.

The Left panel of figure 5.12 shows the resulting invariant mass distribution, for candidates with $p_{\rm t} > 4$ GeV/c, in a sample of 10^8 Pb–Pb minimum-bias collisions (0–100% centrality class). The $\Lambda_c \to pK^-\pi^+$ signal is visible with a significance of about 10, within the "AllNew" layout.

5.3 Performance with further improved detector

Another ITS layout has been investigated to test the improvement of a thinner innermost layer. In this configuration the first layer has a material budget of $X/X_0 = 0.1\%$ and a radius equal to 2.2 cm. It differs from the "AllNew" layout only in the material budget of the first layer: from 0.3% to 0.1%. The feasibility of this small material budget is currently under study. In figure 5.11 the comparison between the impact parameter and the transverse momentum resolutions of the two layouts is shown: the blue curve represents the standard "AllNew" and the red one represents the "AllNew0.1%" layout.

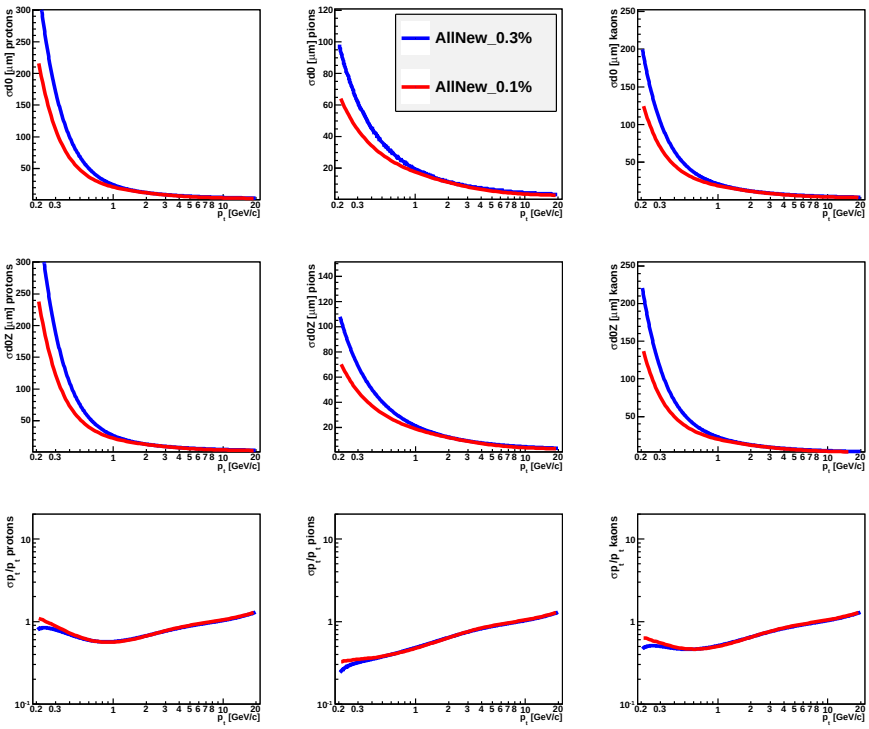

Figure 5.11: Track impact parameter resolution in $r\phi$ and z, and transverse momentum resolution ("AllNew" in blue and "AllNew0.1%" in red), for protons, pions and kaons.

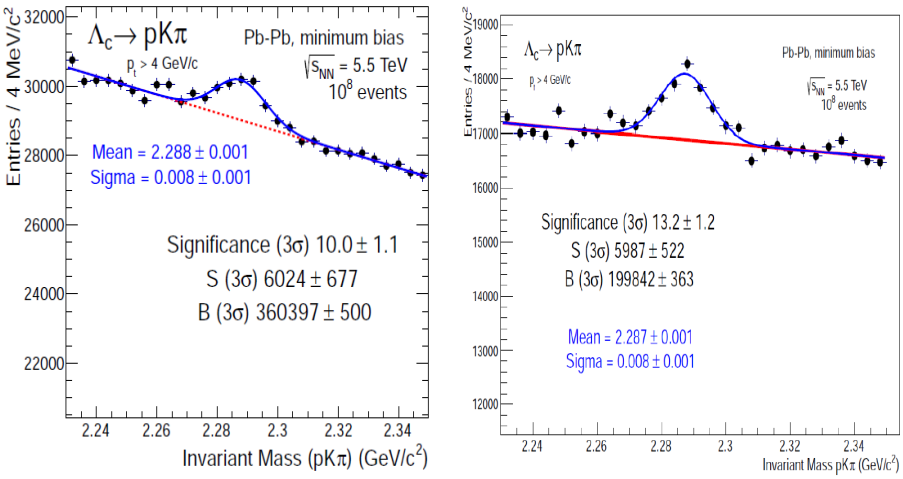

Figure 5.12: Left: $\Lambda_c \to pK^-\pi^+$: invariant mass distribution for $p_{\rm t} > 4$ GeV/c with ITS upgrade "AllNew" (X/X_0 =0.3%) in Pb–Pb minimum-bias collisions (0–100%) at $\sqrt{s_{\rm NN}} = 5.5$ TeV. Right: the same, obtained with ITS upgrade "AllNew" with the material budget of the first layer equal to (X/X0=0.1%)

The analyzes carried out with the method described above, provide a significance of 13, 30% better than the 'AllNew' layout obtained with X/X_0 = 0.3%, assuming the same number of events. Invariant mass distribution is shown in the right panel of 5.12.

5.4 Reconstruction efficiency

Also the efficiency of Λ_c reconstruction is enhanced with respect the current layout, as shown in figure 5.13. The efficiency is defined as the ratio between the number of reconstructed Λ_c, and the number of generated Λ_c in the detector acceptance, with the three daughters within the acceptance. The acceptance has been assumed to be $|\eta| < 0.9$. The figure shows the efficiency obtained with the current ITS (blue) and with the ITS Upgrade (0.3% 'All New' layout) with and without the cut selection (in green and

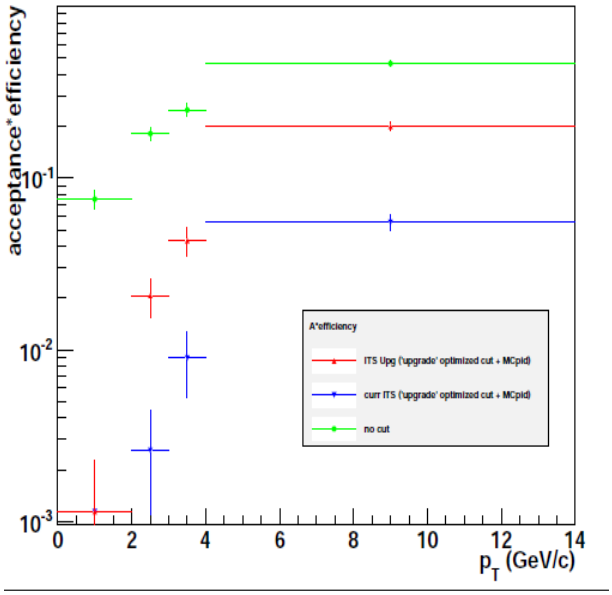

Figure 5.13: Reconstruction efficiency for Λ_c detectable, within the acceptance, for current ITS and upgraded one.

red, respectively).

5.5 Conclusion

In summary, this study shows that with the upgraded ITS the Λ_c signal significance improves (on the same statistical sample) by more than a factor of 2 for pp collisions and the signal becomes accessible in Pb–Pb collisions, where it is currently not observed in data. These results should be considered as a lower limit of the attainable performance, since a dramatic improvement can be expected from the implementation of a dedicated trigger based on topological selections.

Conclusions

The subject of this thesis is the study of a possible upgrade of the Inner Tracking System (ITS) of the ALICE experiment. In order to explain the motivations for the upgrade, the analysis performed by ALICE has been presented, with a review of the status of the current ITS and its tracking performance in terms of spatial and momentum resolution and tracking efficiency. Despite its excellent capabilities to study high energy nuclear collisions, there are several frontiers for which the current experimental setup is not yet fully optimized. The design goal of the new detector focuses on the improvement of the impact parameter resolution, of the transverse momentum resolution and of the efficiency of the stand-alone tracking algorithm. The simulation studies have demonstrated that the improved spatial resolution would be obtained with a first layer closer to the beam line, with thinner silicon sensors (low material budget), and a higher granularity, resulting in an improved intrinsic resolution of each sensor. Such modifications would also result in an enhanced transverse momentum resolution, which would also benefit from the addition of other layers. This last modification is also of great importance for the improvement of the tracking efficiency. In or-

der to study in detail these features, a simulation tool has been developed, completely integrated in the existing simulation and analysis framework (AliRoot). The new detector has been simulated in details, from the geometry to the detector response and the tracking algorithm. The aim was to provide a flexible tool, allowing one to easily switch among different layouts, in order to optimize the design of the new detector and to study physics performance on benchmark channels. When the features of the new layout will be chosen, the tool will be finalized, and eventually will replace the current ITS in the AliRoot framework. The tool has been validated by checking its ability to reproduce the current ITS performance using the current ITS design, with both pp and Pb–Pb Monte Carlo samples. After validation, the tool was used to check the tracking performance obtained with new layouts under test. In particular, two layouts were considered, both composed of seven layers: the "AllNew" is composed by all new pixel-like detectors, with the first layer at a distance of 2.2 cm from the beam line; in the "SPDNew" layout the current two SPD layers are replaced by three new layers of pixel detector, with the first layer closer to the beam pipe. The impact parameter resolution obtained with both the new layouts is improved with respect to the present by a factor two in the transverse plane and by a factor five in the z coordinate. The transverse momentum resolution is different for the two scenarios: the "AllNew" exhibits a resolution that is a factor two better than the current one, while the improvement obtained by the "SPDNew" is about 10% for p_T=1 GeV/c. The tracking efficiency has also been investigated for

the two layouts: an improvement at low p_T is obtained with both of them, but it is better for the "AllNew" configuration. Finally, an additional layout has been explored: to improve the efficiency, a good initial seeding is fundamental for the tracking algorithm. To this aim a new layer has been added, at large radius, closer to the last layer (r_{layer7}=43 cm, r_{layer8}=43.4 cm). This "$7AllNew_{doubled}$" layout leads to a better tracking efficiency down to p_T>0.2 GeV/c.

The good momentum resolution and tracking efficiency would permit a trigger selection of event topologies with displaced vertices, resulting in a much better statistical significance for heavy flavour analysis. The Upgrade would also permit a reconstruction of charm and beauty with the ITS and TRD+TOF, without the TPC, allowing to perform a very fast readout, with the capability to sustain a Pb–Pb interaction rate up to 50 kHz.

To investigate the upgraded performance on physical channel, a study for heavy flavor detection has been carried out by considering the analysis of the $\Lambda_c \to pK\pi$ with the "AllNew" scenario. The study of open charm baryon channels such as the Λ_c is expected to play a crucial role in understanding the characteristics of QGP. With the current setup, the Λ_c signal is seen only in pp, with a poor significance, equal to five. The limit to the current performance is set by the poor spatial resolution at low p_T. The study of this baryon in the upgrade scenario is then of particular interest. To study the performance of an upgraded detector on this particle, a fast simulation tool has been used, based on existing Monte Carlo productions, including

detailed geometry and response of current ALICE detector. The effects of the new ITS has been introduced by improving the reconstructed track parameters according to the p_T and particle species dependent scaling laws obtained in the previously described performance simulations. A detailed study on the cut optimization to separate the signal from the combinatorial background has been carried out. The significance obtained in pp is larger by a factor 2 with respect to the current analysis on a date sample of about 10^9 minimum bias pp collisions. In Pb–Pb collisions, the Λ_c is not visible with the current layout. With the "AllNew" configuration, in a sample of 10^8 minimum bias event (equivalent to one month of minimum bias Pb–Pb data taking) the invariant mass distribution shows a significance of 10. A more ambitious layout, with the challenging material budget of 0.1% in the first layer, has been also explored: the resulting significance is 13. The outcome of such studies proves the huge effect on the ALICE performance in the heavy flavour sector, which would be provided by an upgraded ITS detector.

Bibliography

[1] Edward V. Shuryak. Quantum Chromodynamics and the Theory of Superdense Matter. Phys. Rept., 61:71-158, 1980. doi:10.1016/0370-1573(80) 90105-2

[2] Karsch (for the RBC-Bielefield Collaboration), Transition temperature in QCD with physical light and strange quark masses, Journal of Physics G: Nucl. and Part. Phys. 34 No 8 (2007) S627-S630

[3] A. Chodes et al., Phys. Rev. D9 (1974) 3471.

[4] Karsch (for the RBC-Bielefield Collaboration), Transition temperature. Presentation at Quark Matter 2006 Shanghai 14-20 Nov 2006

[5] J. D. Bjorken, *Highly relativistic nucleus-nucleus collisions: The central rapidity region.* Physical Review D 27 (1983) 140-151

[6] J. Schukraft, *Little bang at big accelerators: Heavy ion physics from AGS to LHC.* Nucl. Phys. B 75 (1999) 46-53

[7] L. Maiani, *Towards a new state of matter* arXiv:hep-ph/0602113v1 13 Feb 2006

[8] M. Gyulassy and L. McLerran, *New forms of QCD matter discovered at RHIC.* Nucl. Phys. A 750 (2005) 30-63

[9] *The Large Hadron Collider Accelerator Project.* CERN/AC/93-03 (LHC) 1993

[10] *LHC design report.* http://ab-div.web.cern.ch/ab-div/Publications/LHC-DesignReport.html

[11] R. Baier, Y.L. Dokshitzer, A.H. Mueller, S. Peigne and D. Schiff, Nucl. Phys. B 483 (1997) 291, arXiv:hep-ph/9607355.

[12] R. Baier, Y.L. Dokshitzer, A.H. Mueller, S. Peigne and D. Schiff, Nucl. Phys. B 484 (1997) 265, arXiv:hep-ph/9608322.

[13] S. Wicks, W. Horowitz, M. Djordjevic and M. Gyulassy, Heavy quark jet quenching with collisional plus radiative energy loss and path length uctuations, Nucl.Phys. A783, 493 (2007), arXiv:nucl-th/0701063, doi:10.1016/j.nuclphysa.2006. 11.102.

[14] W. Horowitz and M. Gyulassy, Heavy quark jet tomography of Pb + Pb at LHC: AdS/CFT drag or pQCD energy loss?, Phys.Lett. B666, 320 (2008), arXiv:0706. 2336, doi:10.1016/j.physletb.2008.04.065.

[15] H. van Hees and R. Rapp, Phys. Rev. C 71, 034907 (2005).

[16] W. Broniowski and W. Florkowski, hep-ph/0202059

[17] F. Becattini et al., Phys. Rev. C 69, 024905 (2004)

[18] E.L. Bratkovskaya, Signal of the QGP phase transition - a view from microscopic transport models, arXiv:0710.5756.v1 [nucl.th]

[19] N. Armesto, A. Dainese, C. Salgado and U. Wiedemann, Testing the color charge and mass dependence of parton energy loss with heavy-to-light ratios at BNL RHIC and CERN LHC, Phys. Rev. D 71, 054027 (2005), doi:10.1103/PhysRevD.71.054027.

[20] C. Gupt, R.K. Shivpuri, N.S. Verma and A.P. Sharma, Nuovo Cim. A75 (1983) 408; T. Ochiai, Prog. Theor. Phys. 75 (1986) 1184; T.S. Biro, P. Levai and J.Zimanyi, Phys. Lett. B347 (1995) 6; T.S. Biro, P. Levai and J. Zimanyi, J. Phys. G 28 (2002) 1561.

[21] S.A. Voloshin, Nucl. Phys. A. 715 (2003) 379c; D. Molnar and S.A. Voloshin, Phys. Rev. Lett. 91 (2003) 092301; R.J. Fries, B. Muller, C. Nonaka and S.A.u Bass, Phys. Rev. Lett. 90 (2003) 202303; V. Greco, C.M. Ko and P. Levai, Phys. Rev. Lett. 90 (2003) 202302; Z.W. Lin and C.M. Ko, Phys. Rev. Lett. 89 (2002) 202302; Z.W. Lin and D. Molnar, Phys. Rev. C68 (2003) 044901.

[22] B. M Ìller, nucl-th/0404015.

[23] F. Becattini, Production of Multiply Heavy Flavored Baryons from Quark Gluon Plasma in Relativistic Heavy Ion Collisions, Phys. Rev. Lett. 95, 022301 (2005), doi:10.1103/PhysRevLett.95.022301.

[24] S. A. Voloshin, A. M. Poskanzer, and R. Snellings, in Relativistic Heavy Ion Physics, Landolt-Bornstein Vol. 1 (Springer-Verlag, Berlin, 2010), pp. 5-54.

[25] Denes Molnar. Charm elliptic flow from quark coalescence dynamics. J. Phys., G31:S421âS428, 2005. arXiv:nucl-th/0410041, doi:10.1088/0954-3899/31/4/052. 32

[26] K. Aamodt et al.[ALICE Collaboration], J. Instrum 3, S08002 (2008).

[27] ALICE collaboration. ALICE Time Projection Chamber: Technical Design Report. Technical Design Report ALICE. CERN, Geneva, 2000. http://cdsweb.cern.ch/record/451098.

[28] ALICE Collaboration. ALICE Time-Of-Flight system (TOF): Technical Design Report. Technical Design Report ALICE. CERN, Geneva, 2000. http://cdsweb.cern.ch/record/430132

[29] W.T.Scott, Rev.Mod.Phys. 35, 231, (1963)

[30] G.E.Bruno D.Elia et al. Sensor thickness dependence of the ALICE Silicon Pixel Detector performance ALICE-INT-2005-011

[31] G.E.Bruno D.Elia et al. Comparison of SPD beam test data with the simulation models in ALICE-INT-2005-022

[32] G.E.Bruno et al. Tuning of the SPD simulation model in AliRoot ALICE-INT-2008-003

[33] G. Aglieri Rinella et al., The pixel trigger system for the ALICE experiment PoS (RD09) 005 (2009)

[34] R. Turrisi et al., ALICE Pixel Detector operations and performace PoS (VERTEX 2010) 007 (2010)

[35] M.Sitta and P.Christakoglou, Operations and performance of the Silicon Drift and Silicon Strip Detectors of the ALICE experiment, PoS (Vertex 2010) 009 (2010)

[36] G. Contin, The ALICE Silicon Strip Detector performance during the first LHC data taking PoS (RD09) 005 (2011)

[37] AliRoot: ALICE Off-line framework for simulation, reconstruction and analysis, http://aliceinfo.cern.ch/Offline.

[38] C. Bombonati et al., Alignment of the ALICE Inner Tracking System with cosmic-ray tracks, ALICE-INT-2009-035 (2009) A. Dainese et al., Validation of the survey measurement for the alignment of the Silicon Strip Detector using cosmic-ray tracks, ALICE-INT-2009-045 (2009)

[39] Blobel, V. (2006). A new fast track-fit algorithm based on broken lines. Nucl. Instrum. Meth., A566:1417.

[40] B. Batyunya, Yu. Belikov, K. Safarik, ALICE Internal Note, ALICE-INT-97-24 (1997)

[41] E. Crescio et al. Performance of the ITS stand-alone tracker in pp collisions, ALICE-INT-2009-046. 2009

[42] Physics Publications of the ALICE Collaboration in Refereed Journals, http://aliceinfo.cern.ch/ArtSubmission/publications.

[43] STAR Collaboration, Experimental and theoretical challenges in the search for the quarkâgluon plasma: The STAR Collaborationâs critical assessment of the evidence from RHIC collisions, Nuclear Physics A 757 (2005) 102-183

[44] ALICE Collaboration, Charged-Particle Multiplicity Density at Midrapidity in Central Pb–Pb Collisions at $\sqrt{s_{NN}} = 2.76$ TeV, Phys. Rev. Lett. 105, 252301 (2010), doi:10.1103/PhysRevLett.105.252301.

[45] A.Toia Bulk properties of Pb–Pb collisions at $\sqrt{s_{NN}} = 2.76$ TeV measured by ALICE, J. Phys. G: Nucl. Part. Phys. 38 (2011) 124007 (8pp) doi:10.1088/0954-3899/38/12/124007

[46] Adler SS et al (PHENIX) 2005 Phys. Rev. C 71 034908

[47] Phys.Lett.B 696 (4): 328-337, 2011 doi:10.1016/j.physletb.2010.12.053

[48] A. Dainese et al. (ALICE collaboration), Heavy-flavour production in Pb–Pb collisions at the LHC, measured with the ALICE detector, 1106.4042, arXiv nucl-ex/1106.4042, 2011, arXiv:1106.4042.

[49] Adams J et al (STAR Collaboration and STAR-RICH Collaboration) 2006 arXiv:nucl-ex/0601042

[50] Lamont M A C (STAR Collaboration) 2007 Eur. Phys. J. C 49 35

[51] M. Cacciari, M. Greco and P. Nason, The pt spectrum in heavy flavor hadroproduction, JHEP 9805, 007 (1998), arXiv:hep-ph/9803400.

[52] M. Krzewicki et al. (ALICE Collaboration), Elliptic and triangular flow of identified particles at ALICE, 1107.0080, arXiv nucl-ex/1107.0080, 2011., arXiv:1107.0080.

[53] Shen C, Heinz U W, Huovinen P and Song H 2011 arXiv:1105.3226 [nucl-th]

[54] Aamodt K et al (ALICE Collaboration) 2010 Phys. Rev. Lett. 105 252302

[55] Teaney D, Lauret J and Shuryak E V 2001 arXiv:nucl-th/0110037

[56] B. Abelev et al. (STAR Collaboration), Mass, quark-number, and $\sqrt{s_{NN}}$ dependence of the second and fourth flow harmonics in ultra-relativistic nucleus-nucleus collisions, Phys.Rev. C75, 054906 (2007), arXiv:nucl-ex/0701010, doi:10.1103/PhysRevC.75.054906.

[57] V. Greco, C. Ko and R. Rapp, Quark coalescence for charmed mesons in ultrarelativistic heavy-ion collisions, Physics Letters B 595, 202 (2004), doi:10. 1016/j.physletb.2004.06.064.

[58] Krzewicki M 2011 J. Phys. G: Nucl. Part. Phys. 38 124047

[59] Florin Dobrin A 2011 J. Phys. G: Nucl. Part. Phys. 38 124170

[60] L. Rossi, P. Fischer, T. Rohe and N. Wermes, Pixel Detectors: from Fundamentals to Applications (Springer, Berlin, Germany, 2006).

[61] M. Stanitzki, Advanced monolithic active pixel sensors for tracking, vertexing and calorimetry with full CMOS capability, Nucl. Instr. and Meth. A (2010), doi:10.1016/j.nima.2010.11.166.

[62] O. S. Brning et al., LHC Design Report (CERN, Geneva, 2004).

[63] Brun R. et al. P 1985 GEANT3 User Guide CERN Data Handling Division DD/EE/84-1 http://www.info.cern.ch/asdoc/geantold/GEANTMAIN.html

[64] G.R.Lynch and O.I.Dahl, Nucl.Instr.and Meth. B58, 6, (1991)

[65] Li S-Y and Wang X-N 2002 Phys. Lett. B 527 85

[66] K.Nakamura et al. Review of PArticle Physics, Journal of Physics G 37 (2010)

[67] 3-D Chips: IBM Moves Moore's Law Into The Third Dimension ScienceDaily (Apr. 12, 2007)

[68] R.Yarema 3D Circuit Integration For VErtex and Other Detectors Vertex 2007 N.Y.

[69] Nuclear and Particle Puysics Volume 33 July 2006

[70] A.Dainese "Tesi dottorato: Charm production and in-medium QCD energy loss in nucleus-nucleus collisions with ALICE. A performance study." Universita' degli studi di Padova

[71] V.Koch Introduction to Chiral Symmetry Nucl-th 9512029 (1995)

[72] ALICE: Physics Performance Report, Volume I J. Phys. G: Nucl. Part. Phys. 30 (2004) 1517-1763

[73] ALICE: Physics Performance Report, Volume II J. Phys. Nucl. Part. Phys. 32 (2006) 1295-2040

[74] ALICE: Technical Design Report of the Inner Tracking System(ITS) CERN /LHCC 99-12 ALICE TDR 4 18 June 1999

[75] ALICE Collaboration, First proton-proton collisions at the LHC as observed with the ALICE detector: measurement of the charged-particle pseudorapidity density at v s=900 GeV, Eur.Phys.J.C, 65 (2010), 111-125

[76] M. Djordjevic, M. Gyulassy, Phys.Lett. B560 (2003) 37-43

[77] Martinez 200855,PhysRevC.74.024902

[78] STAR Collaboration, The STAR Heavy Flavor Tracker, Conceptual Design Report, submitted to DOE at CD1 review, 2009.

[79] http://alice.web.cern.ch/Alice/ppr/ITSupgrade/ITSUpgrade-CDR.php

[80] J. Gasser and H. Leutwyler, Phys. Rep. 87 (1982) 77.

[81] J.F. Donoghue, Annu Rev. Nucl. Part. Sci. 39 (1989) 1.

[82] K.J. Eskola et al., Nucl. Phys., B570 (2000) 379.

[83] The **C**ompact **M**uon **S**olenoid, homepage: http://cms.cern.ch/

[84] **A T**oroidal **L**HC **A**pparatus, homepage: http://atlas.ch/

[85] The **L**arge **H**adron **C**ollider **b**eauty experiment, homepage: http://lhcb.web.cern.ch/lh

[86] **A L**arge **I**on **C**ollider **E**xperiment, homepage: http://aliceinfo.cern.ch/

[87] D. Contarato, M.Battaglia Monolithic Pixel Sensors ILC Vertex 2007

[88] G. Batignani et al. Recent development in 130 nm CMOS monolithic active pixel detectors Nuclear Physics B (Proc. Suppl.) 172 (2007) 20-24

[89] For a review see L. McLerran *The Color Glass Condensate and Small x Physics: 4 Lectures.* arXiv:hep-ph/0104285v2 27 Apr 2001

[90] K. Aamodt et al. [ALICE Coll.], Phys. Lett. B696 (2011) 30-39. [arXiv:1012.1004 [nucl-ex]].

[91] ALICE Collaboration, K. Aamodt et al., arXiv:1105.0380v1 [hep-ex]

[92] T. Sjöstrand, Comput. Phys. Commun., 82, 74 (1994)

[93] T. Sjöstrand, S. Mrenna and P. Skands. JHEP 05, 026, (2006)

[94] P.Z. Skands, arXiv:0905.3418 (2009)

[95] A.Dainese, on behalf of the ALICE Collaboration, Heavy-flavour production in Pb-Pb collisions at the LHC, measured with the ALICE

detector, talk at the XXII International Conference on Ultrarelativistic Nucleus Nucleus Collisions (Quark Matter 2011)